The Dissertation Committee for Seyyed Hossein Mousavi
certifies that this is the approved version of the following dissertation:

Optical Properties And Collective Modes Of Plasmonic Meta-Surfaces

Committee:

Gennady Shvets, Supervisor

Roger Bengtson

Alex Demkov

Manfred Fink

Hao Ling

Optical Properties And Collective Modes Of Plasmonic Meta-Surfaces

by

Seyyed Hossein Mousavi, M.Sc., B.S.

DISSERTATION
Presented to the Faculty of the Graduate School of
The University of Texas at Austin
in Partial Fulfillment
of the Requirements
for the Degree of

DOCTOR OF PHILOSOPHY

THE UNIVERSITY OF TEXAS AT AUSTIN
December 2012

Dedicated to my parents and my wife, Neda.

Acknowledgments

This thesis represents the work of many scientists. Most importantly, I must thank my adviser Professor Gennady Shvets for all his guidance, encouragement and support which made this work possible. I also wish to thank Dr. Alexander Khanikaev who provided me with hands on training and with whom I collaborated closely in my daily research. I thank fellow group members Drs. Burton Neuner III, Yoav Avitzour, Chihhui Wu, and Chris Fietz for their helps, as well as their substantial contribution to our collaborative research efforts. I must also thank the members of my dissertation committee for their feedback and valuable suggestions. Supercomputing resources were provided by the Texas Advanced Computing Center.

Optical Properties And Collective Modes Of Plasmonic Meta-Surfaces

Publication No. __________________

Seyyed Hossein Mousavi, Ph.D.
The University of Texas at Austin, 2012

Supervisor: Gennady Shvets

Plasmonics is an important branch of optics and photonics, focusing on the electromagnetic response of metals or other materials with free carriers. This field has recently experienced a significant expansion due to its importance for applications. Plasmonics has shown great promises in green energies, biosensing, nanolasers, and imaging. The main advantage of plasmonics stems from the existence of unique excitations, referred to as plasmons, representing collective response of the free carriers to the electromagnetic field. While plasmons, both in the bulk and on the surface of the metals, have been known for decades, the recent advances in nano fabrication and material sciences at nano scale have enabled versatile engineering of these modes.

Focus of my dissertation is surface plasmons whose properties can be tailored by judiciously nano-patterning metal films and surfaces. Such patterned structures, referred to as metasurfaces, are the main tool to control and boost the light-matter interaction. Appropriately designed metasurfaces provide many-fold electromagnetic energy enhancement on the surface which can be used to amplify numerous surface effects such as SEIRA and nonlinear optical phenomena, facilitate spectroscopy, and enhance absorption of light.

In this thesis, I report approaches to shape and engineer the confinement, mode profile, and lifetime of the surface modes. I also investigate how the dielectric environment affects the properties of the modes. The effect of the geometry and topology of the nano patterns on the optical response of metasurfaces is also studied. Finally I study how manipulating symmetries of metasurfaces can be used to tailor polarization state of light and lifetime of the modes using an ultrathin metasurface, instead of bulky traditional optical elements.

The work summarized in this thesis has brought marked advances in understanding the physics behind the collective surface waves in nano-structured metasurfaces. It paves new avenues for engineering structures with desirable properties. The immediate application of my findings is the compactification of optical elements, and envisioning next-generation plasmonic-based on-chip devices.

Table of Contents

Chapter 1. Introduction To Plasmonics **1**

Chapter 2. Highly Confined Hybrid Spoof Surface Plasmons in Ultra-thin Metal/Dielectric Heterostructures **20**

List of Figures

Chapter 1

Introduction To Plasmonics

In this chapter I will give a brief review of what plasmonics is and how it is related to optics. The idea of metals being only reflectors/mirrors in optics or conducting elements in electronics is stale. Recently there has been immense interest in exploiting other unique properties of metallic structures such as their unusual ability to confine light below the diffraction limit of light. From the electromagnetic point of view, metals are plasmas that are comprised of free conduction electrons and fixed ions. The recent research is focused on exploiting the collective oscillations of the free electrons of this plasma, and consequently the topic has become known as *plasmonics* and the collective resonant oscillations are referred to as *plasmons*.

1.1 Plasmons

The collective resonant oscillations in a plasma is called a *plasmon*. The mechanism behind this resonance stems from the restoring (capacitive) force between the separated layer of free electrons and the fixed ions that are left behind (see Fig. 1.1). Let ions have an infinite mass and electrons have a mass m and a number density n. The resonance angular frequency ω_p is given by [59]

$$\omega_p^2 = \frac{ne^2}{m\epsilon_0}, \tag{1.1}$$

where e is electron's charge and ϵ_0 is the permittivity of vacuum. For metals such as silver, the plasma frequency is in ultraviolet (UV) [59].

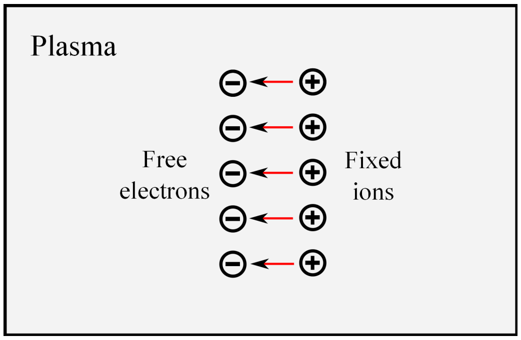

Figure 1.1: Schematics showing the collective oscillations of free electrons in metal (plasma) provided by the restoring electric field (arrows).

Plasmons play a large role in the optical properties of metals. Due to this resonance, the permittivity of a metal is frequency dependent and is given by $\epsilon(\omega) = 1 - \frac{\omega_p^2}{\omega(\omega+i\gamma)}$ where the relaxation frequency γ originates from the scattering of free electrons from any scattering source such as phonons [59]. Electromagnetic radiation incident upon a metal, or a plasma in general, will be reflected or (partially) transmitted depending on the radiation frequency ω. If the incident frequency is below the plasma frequency, the permittivity possesses a negative sign and becomes a reflective mirror. Only above its plasma frequency metal becomes opaque. However, due to the scattering mechanisms in metal, it dissipates the electromagnetic energy and the transmitted power is negligible.

1.2 Localized Plasmons

Being known for centuries, the color of colloids of small metallic particles is an interesting optical effect. The color exhibited by such particles is due to a plasmonic resonance. When light is incident on such a particle, the electric field of the light exerts a force on the free electrons in the metal. The redistribution of charges (see Fig. 1.2) acts to provide a restoring force on the displaced electrons and, just as in the case of the bulk plasmon discussed above, there is an associated resonant frequency. For a small spherical particle of radius $a \ll \lambda$, this phenomenon can be explained in terms of electrostatics, neglecting any phase shift across the particle. Using electrostatic analysis, one can derive a simple analytical formula for the electric dipole moment, $\mathbf{p}$, of the particle

$$\mathbf{p} = 4\pi a^3 \, \frac{\epsilon_m - \epsilon_d}{\epsilon_m + 2\epsilon_d} \, \mathbf{E}, \tag{1.2}$$

where ϵ_m and ϵ_d are the permittivities of the metallic particle and the surrounding medium, respectively. The localized plasmon corresponds to the divergence of the electric dipole moment $\mathbf{p}$. A resonance occurs at $\epsilon_m = -2\epsilon_d$ as can be seen from Eq. (1.2). Note that the resonance spectral position is independent of the size of the particle as long as the particle's radius is much smaller compared to the wavelength. The color of different metallic materials (embedded in vacuum) originates from this resonance and is dictated by the frequency at which $\epsilon(\omega) = -2$. For gold this occurs in the green part of the spectrum, at 520 nm, whilst for silver it occurs in the deep violet (420 nm).

Note that this is a localized plasmon confined in a very small volume, beating the traditional diffraction limit of light [52]. An electrodynamic correction to Eq. (1.2) is needed since it does not include the radiative losses of a dipole at a finite frequency [38], however, it does not modify the resonance condition discussed above significantly. Also due to the symmetry of the spherical particle, this particle supports three degenerate dipole resonances, each corresponding to a dipole aligned along one of the principal axes.

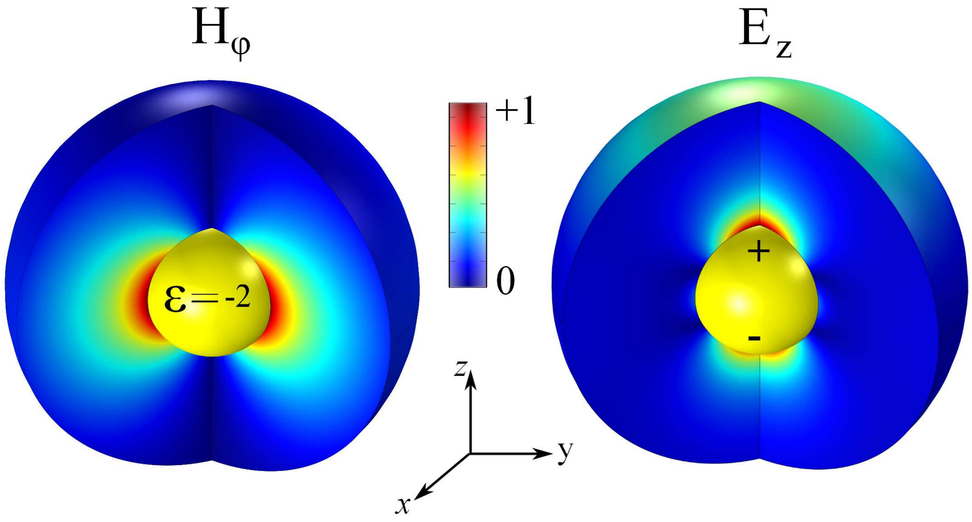

Figure 1.2: Electric (right) and magnetic (left) fields of the localized plasmon mode of a small spherical plasmonic particle.

For ellipsoidal particles with principal axes a, b, and c, an analogous expression to Eq. (1.2) can be found in the quasistatic approximation via introducing geometrical depolarization factors L_i along these axes, [19] leading to

$$\mathbf{p} = \frac{4}{3}\pi abc\,\frac{\epsilon_m - \epsilon_d}{\epsilon_m + L_i(\epsilon_d - \epsilon_m)}\,\mathbf{E},\quad \sum_i L_i = 1. \tag{1.3}$$

For spherical particles, L_1=L_2=L_3=1/3. For spheroidal particles (L_1=L_2), the plasmon resonance thus splits into a strongly redshifted long-axis mode (polarization parallel to the long axis) and a slightly blueshifted short axis mode (polarization perpendicular to the long axis) [19].

1.3 Surface Plasmons Polaritons

The interface of a metal and a dielectric may support a plasmon mode, referred to as a surface plasmon-polariton (SPP), shown in Fig. 1.3. In contrast to the localized modes associated with particles, the SPP modes associated with a planar interface are propagating, typically over a few tens of micrometers. Due to their propagating nature, it is instructive to look at the dispersion relation (the relationship between frequency and wavevector k_{SPP}) of the mode [92]:

$$k_{\mathrm{SPP}} = \frac{2\pi}{\lambda_{\mathrm{SPP}}} = \frac{\omega}{c}\sqrt{\frac{\epsilon_m \epsilon_d}{\epsilon_m + \epsilon_d}}, \tag{1.4}$$

where λ_{SPP} is the wavelength of the SPP mode and ϵ_d and ϵ_m are the permittivities of the dielectric and metallic layers. First of all, while in the case of localized plasmons, the resonance condition was satisfied at only one frequency, SPPs exist over a wide frequency range. Secondly, in order to have a waveguiding mode confined to the surface, the square root term in Eq. (1.4)

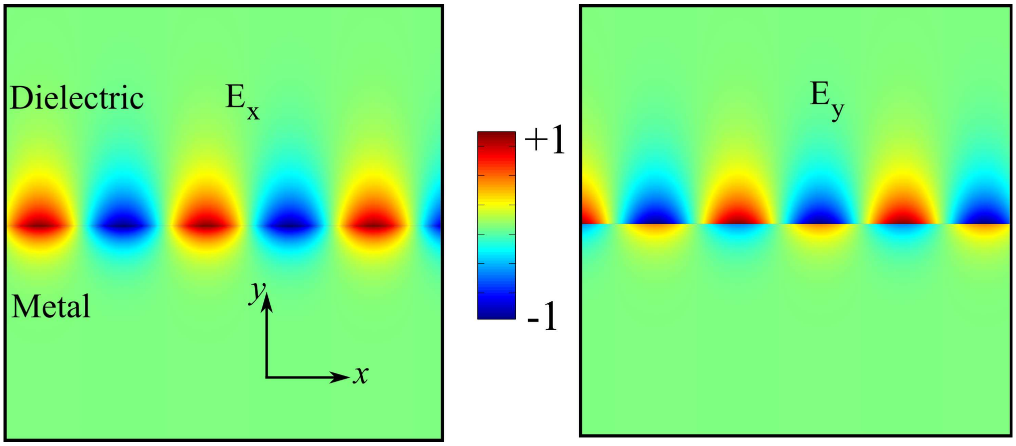

Figure 1.3: Collective oscillations of free electrons running along the x direction in the interface between metal with permittivity ϵ=-2 and vacuum. The left (right) panel shows the x (y) component of the electric field by color.

should be larger than $\sqrt{\epsilon_d}$ which implies that the permittivity of metal should be negative and also $\epsilon_m < -\epsilon_d$. However since the index of the mode is larger than that of the dielectric, coupling to this mode requires special techniques such as prism or grating couplers.

Next I consider a plasmonic film of finite thickness. Each side of the plasmonic film supports a SPP mode. If the cladding on either sides of the film are of the same dielectric material, the modes hybridize and form new coupled SPP modes: (i) even mode with a lower eigen-frequency (than the original mode's) and (ii) odd mode with a higher eigen-frequency [72]. The thinner the film is, to a greater degree the modes hybridize and the larger the frequency shift is. Figure 1.4 shows the electric field of both the odd and even modes which shows the symmetries of the modes. However, even after the hybridization between the modes of the two interfaces, the new eigenmodes still will be guiding, i.e., their dispersion curve lies under the light line ($k_{\parallel} > \omega/c$). Due to the phase mismatch between these modes and the incident light, it is impossible to excite these SPP modes using conventional means. In the next section, I will see how patterning the surface will abate this problem.

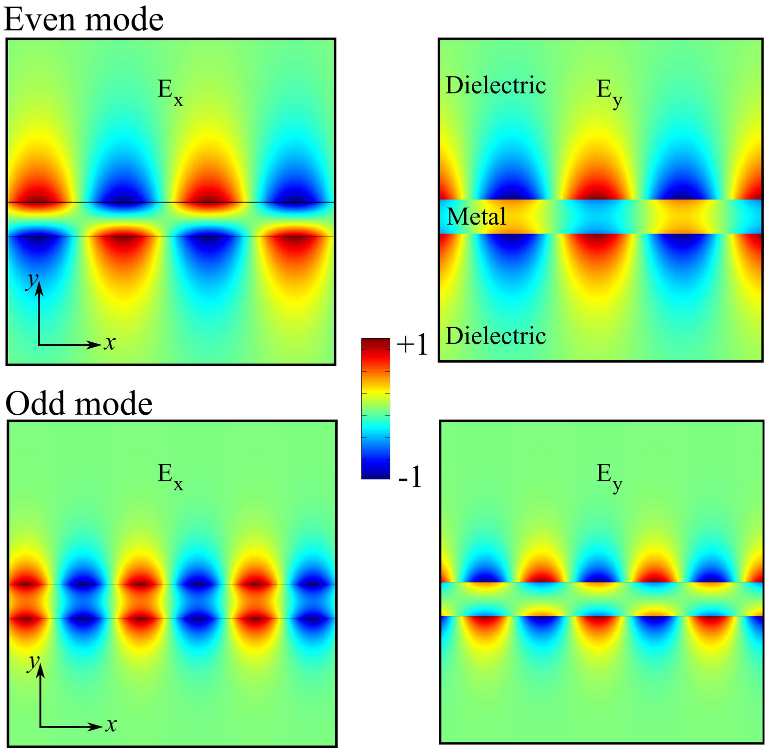

Figure 1.4: Guiding modes (SPPs) on each interface of a plasmonic film hybridize and form two new eigenmodes: An even mode (top panel) and an odd mode (bottom panel). Permittivity of the plasmonic layer is assumed to be -2.

1.4 Periodic Structuring of Surfaces: Meta-Surfaces

As was mentioned in the previous section, there is a significant phase (momentum) mismatch between incident light and SPP modes. One way to alleviate the problem is by structuring the surface to match the momentum $p = \hbar k$ of the diffracted light to that of the SPP modes (see Fig. 1.5). The in-plane wavenumber k^n of the n-th diffracted wave scattered from a one-dimensional grating is $k_{inc} + n\ (2\pi/P)$, where k_{inc} is the in-plane wavenumber of the incident wave, P is the periodicity of the grating, and n is an integer that indexes the order of the diffraction. For example, n=0 represents the secular reflection from the grating. By appropriately choosing the periodicity P, the momentum of the diffracted waves can be matched to that of the surface modes. Structuring the surface not only provides momentum matching but also results in the ability to engineer the dispersion of the modes.

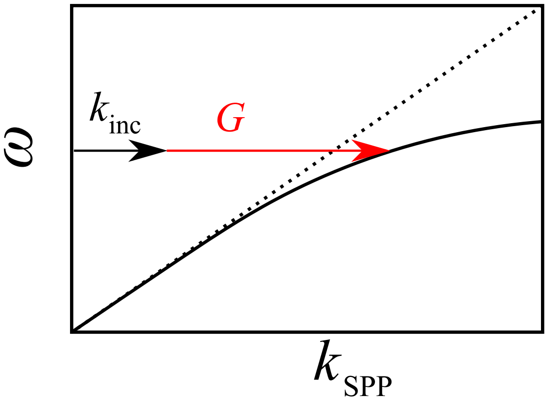

Figure 1.5: Dispersion of surface plasmon $\omega(k_{SPP})$. k_{inc} is the in-plane component of the incident wave vector and G corresponds to the wavenumber needed to couple to the SPP mode under the light line shown by the dotted curve.

1.4.1 Extraordinary Optical Transmission (EOT)

Ordinarily, a metal film perforated by a periodic array of sub-wavelength holes would demonstrate low transmission of light. Remarkably, in 1998

Ebbessen et al. [27] reported that under appropriate conditions such structures can transmit a significant amount of light – a phenomenon that has become known as the extraordinary optical transmission (EOT). The role of surface plasmons in this enhanced transmission is now well established, [14] and the importance of the surface modulation is clear – holes are not essential, appropriate surface corrugations may also enhance the transmittance [20].

The concept of EOT generated considerable interest because it predicted that a periodic array of sub-wavelength holes can transmit orders of magnitude more light than each individual hole could. According to Bethe's prediction [18], a circular hole milled in an ultrathin free-standing metallic sheet would transmit (normalized to the transmission through the same area without any structure)

$$T_B = \frac{64}{27\pi^2}(kr)^4, \tag{1.5}$$

where $k = 2\pi/\lambda$ is the wavevector of the incoming light and r is the hole radius. This expression predicts that transmission of light $T_B \propto (kr)^4 \propto (r/\lambda)^4$ drops rapidly as the the radius r decreases. The finite thickness h of the metallic sheet will attenuate the transmission even further for small holes by adding an exponential decay for $\lambda > 4r$ [95]. This decay comes from the fact that the hole is a circular waveguide whose cutoff is determined by the condition $\lambda = 4r$. Plasmonic response of the walls modifies this condition and effectively enlarges the hole by twice the skin depth [46].

Martin-Moreno et al. [74] explained the EOT phenomenon as follows.

A plasmonic sheet of thickness h supports a SPP mode on each side. However an incoming light directly cannot excite these modes because the momentum of the incoming wave and that of the SPPs do not match. A periodic array of sub-wavelength-sized holes drilled on the metallic sheet provides the momentum required for the excitation of the SPP modes. Finally, the coupling between the excited SPP modes on either side of the sheet results in EOT. Thus, the spectral position where EOT occurs can be determined, to the first approximation, by the dispersion of the SPPs of a smooth metallic interface assuming that the presence of the holes only provides the right momentum but does not change the spectral position of the modes. Assuming that the momentum is provided by the diffracted wave of the order (i,j), the EOT spectral position for a normally incident incoming light is given by:

$$\lambda^0_{\mathrm{EOT}}(i,j) = \frac{P}{\sqrt{\frac{4}{3}(i^2+ij+j^2)}}\sqrt{\frac{\epsilon_m\epsilon_d}{\epsilon_m+\epsilon_d}}. \tag{1.6}$$

In Eq. (1.6), another approximation is that the coupling between the two SPPs on both sides of the film was assumed to result in an insignificant shift of the SPP modes of each side. In reality, the presence of the holes shifts the spectral position of the modes of the smooth film and the actual spectral position of EOT happens just below the wavelength $\lambda^0_{\mathrm{EOT}}(i,j)$ given by Eq. (1.6).

1.4.2 Wood's Anomaly

In 1902, R.W. Wood discovered [112] that on many diffraction gratings, narrow spectral regions showed sharp change of energy diffracted. Rayleigh [93] explained these “anomalies” under the name “passing-off orders”. The physical explanation is the following. Consider a reflection grating which produces a range of diffracted light (see Fig. 1.6). In some order, at some critical wavelength, the diffracted light lies in the plane of the grating. It is not possible for light beyond this point to be diffracted off the grating. The power which would be sent into the forbidden region is redistributed back into the allowed orders (“passed off”). The power appears as an addition, to the spectrum response, with a sharp cut on at the critical wavelength and a steep decline to the red. The additional power is an enhancement of efficiency of the grating, as if the light from two orders has been combined, which it has. As can be imagined from the physical explanation, which involves light passing near the plane of the grating, the additional efficiency is highly polarization-dependent – a Wood’s anomaly is almost entirely polarized perpendicular to the grating rulings (the s-plane).

For incident light with an in-plane wavenumber k_x along the x-axis and k_y along the y-axis, the diffracted order (m,n) has a propagating constant $k_z^{(m,n)}$ along the normal to the surface given by:

$$k_z^{(m,n)} = \sqrt{\epsilon_d k_0^2 - \{k_x + \frac{m\pi}{P_x}\}^2 - \{k_y + \frac{n\pi}{P_y}\}^2}, \tag{1.7}$$

where $k_0 = \omega/c$ is the wavenumber in vacuum and ϵ_d is the permittivity of the medium in which the grating is placed. P_x and P_y are the periodicities along the x and y directions, respectively. Also note that m and n range from $-\infty$ to ∞. The observed diffracted orders away from the grating are the ones

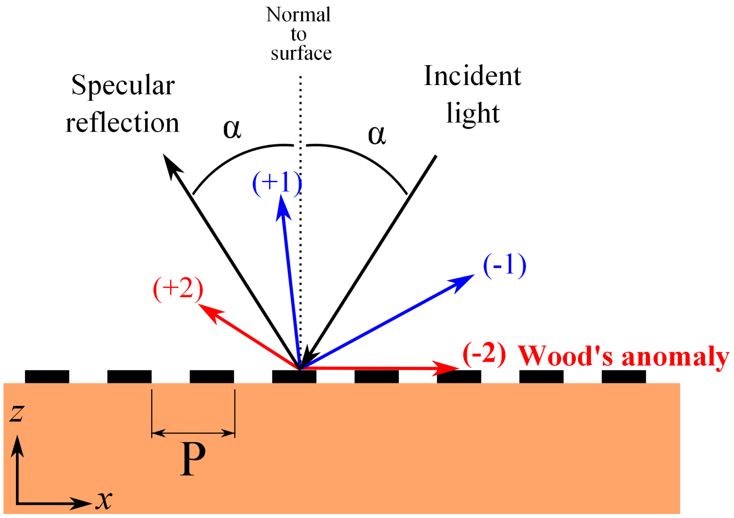

Figure 1.6: A diffraction grating scattering the incident light and producing diffraction orders including the specular reflection (0-th order), ±1-st orders, etc. Here, the diffraction order -2 is about to experience a Wood's anomaly. At a slightly lower wavelength, the power that used to be carried by this order will be redistributed to the other propagating orders.

with a real k_z. The diffraction orders with an imaginary k_z are *evanescent* orders – orders that do not carry power but store energy in the near field of nanostructures (in this case, a diffraction grating).

A Wood's anomaly occurs at the wavelength when a diffraction channel is closing $k_z^{(m,n)} = 0$ where a transition from a propagating order with a real k_z to an evanescent one with an imaginary k_z happens. According to the above equation, for an incidence along the x-direction with an angle α relative to the normal (see Fig. 1.6), this condition is satisfied at a particular wavelength which depends on the incident angle α:

$$\epsilon_d k_0^2 - \{k_0 \sin(\alpha) + \frac{m\pi}{P_x}\}^2 - \{\frac{n\pi}{P_y}\}^2 = 0. \tag{1.8}$$

As an example, Wood's anomalies of the diffraction orders ($\pm m$,0) happens at

$$k_0^{(\pm m,0)} = \frac{m\pi}{P_x} \frac{1}{\sqrt{\epsilon_d} \mp \sin(\alpha)}, \tag{1.9}$$

and that of the diffraction orders (0,$\pm n$) happens at

$$k_0^{(0,\pm n)} = \frac{n\pi}{P_y} \frac{1}{\sqrt{\epsilon_d - \sin^2(\alpha)}}, \tag{1.10}$$

The spectral position of the lowest orders Wood's anomalies for a square lattice is plotted in Fig. 1.7 as a function of the in-plane wavenumber along the x direction (k_y=0).

It is worthwhile noting that Wood's anomaly is not a mode. However, because collective modes usually happen in the immediate vicinity of the Wood's anomalies, sometimes it could mistakenly be considered as a mode [38].

1.5 Mimicking Surface Plasmon Polaritons In Structured Metallic Surfaces

Materials even with quite different dielectric functions from the plasma form can also support electromagnetic surface modes. However, a perfect electric conductor (PEC) is an exception. Pendry et al. in 2004 [87] showed that even such a material can be induced to support surface modes by drilling an array of holes in the surface as long as the holes were sub-wavelength sized. Electromagnetic fields, in this case, penetrate/decay into the holes perforated in PEC and emulate the confinement of the SPPs inside the metals. Even a one-dimensional array of holes perforated in PEC may support a surface

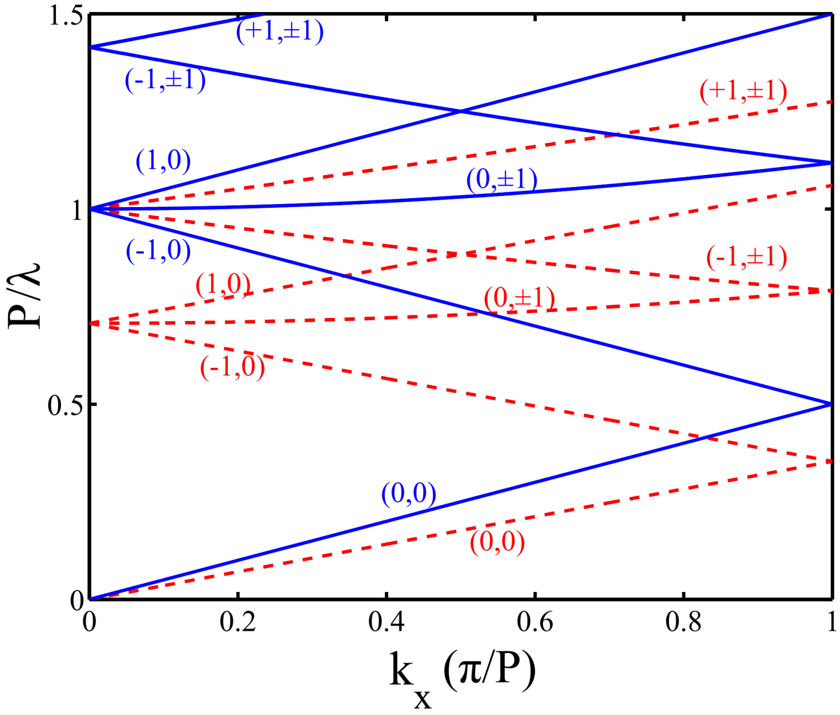

Figure 1.7: Spectral position of the Wood's anomalies for a two-dimensional diffraction grating as a functional of the incident wavenumber along the x-direction. Here I have assumed an asymmetric superstrate (ϵ_{sup}=1, blue curves) and substrate (ϵ_{sub}=2, red curves), and equal periods along the x and y directions P_x=P_y=P.

mode. However, in this case, the holes should be blocked, i.e., they should not be through-holes (see Fig. 1.8). The reason is that a groove, unlike a 2-D hole, supports a mode without a cutoff. In order to emulate the decay of the electromagnetic field into the metallic layer to obtain a real surface mode, grooves should be blocked.

The unique property of "spoof" surface plasmons is the ability to control their eigenfrequency and refractive index using variable size and shape of the

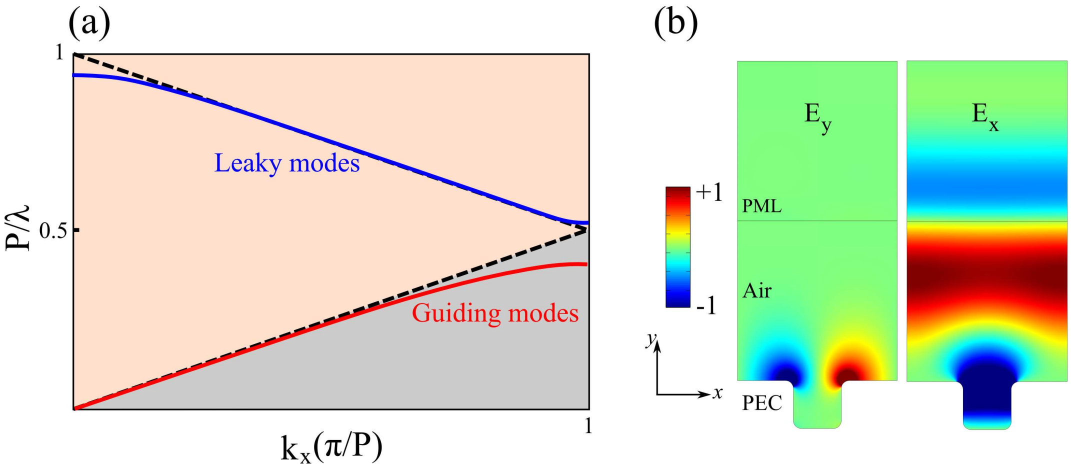

Figure 1.8: An unpenetrable perfect electric conductor (PEC) can be induced to support surface modes by drilling an array of holes. (a) Blue and red curves represent the dispersion relation of the leaky ($k_x < \omega/c$, beige region) and guiding ($k_x > \omega/c$, gray region) "spoof" surface plasmon, respectively. The dashed lines show the light lines, folded at the Brillouin zone's edge. (b) The non-vanishing components of the electric field of a leaky spoof surface plasmon are shown at the Γ point (k_x=0). Here, the width of the groove w and the depth of the groove are chosen to be $0.3P$. For leaky modes, perfectly matched layers (PMLs) are used to truncate the computational region in the y direction.

metal holes. The theory of spoof surface plasmons will be presented in Chapter 2 and its appendix.

1.6 Babinet Principle And Structures Complementary To Holey Meta-Surfaces

Let S be a diffracting meta-surface, and $\tilde{S}$ its complement, i.e., the surface that is transparent where S is opaque, and opaque where S is transparent. If the surfaces are infinitely thin without any ohmic losses and are surrounded by a symmetric (substrate=superstrate) dielectric environment, the transmission through S for one polarization equals the reflection through $\tilde{S}$ for a 90° rotated polarization. The sum of the radiation patterns caused by S and $\tilde{S}$ must be the same as the radiation pattern of the undisturbed beam. In places where the undisturbed beam would not have reached, this means that the radiation patterns caused by S and $\tilde{S}$ must be opposite in phase, but equal in amplitude.

According to Babinet principle, a periodic assembly of meta-molecules also supports both collective waveguiding modes and collective leaky modes. The only difference is that, at resonance, instead of having a peak of transmission, a peak in reflection would be observed in the far field. The simplest example of such a complementary metasurface is comprised of a two-dimensional periodic array of dipole antennas – antennas with a long dimension of approximately half the wavelength of light. This structure has been shown to support spoof SPPs with a dispersion controllable by the dimensions of the antennas, as well as the plasmonic response of the metallic antennas [38]. The mechanism behind this resonance roots in the long-range transverse interactions between dipoles giving rise to the phenomenon of Wood's anomalies [38] and spoof plasmons.

1.7 Organization Of Thesis

In Chapter 2, I propose an approach to improve the confinement of spoof surface plasmons while retaining their important advantage: the ability to control their eigen-frequency and refractive index using variable size and

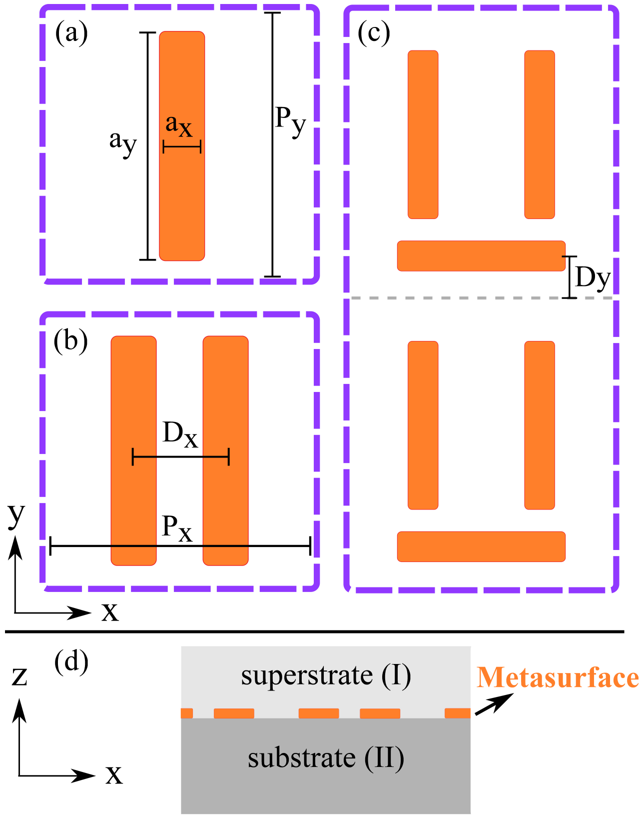

Figure 1.9: (Color online.) Schematic unit cell of the three structures considered in chapter 3: (a) single-antenna, (b) double-antenna, and (c) dolmen metasurfaces. In (c), two unit cells (separated by a dashed line) are shown. (d) shows the side view of the metasurfaces cladded by the superstrate and the substrate.

shape of the metal holes. This is achieved by combining metal structuring with the traditional method of electromagnetic field confinement, waveguiding. Also I give a detailed derivation of a semi-analytical technique based on mode matching. I used this method to study both the eigenmodes and their lifetimes and also the optical response of the structure in the driven simulations.

In Chapter 3, I study the effects of the optical contrast between the superstrate and substrate of a metasurface on the long-range dipole-dipole interactions between the unit cells comprising the surface. Three topologically different structures are considered (shown in Fig. 1.9). I show that in all the cases, Wood's anomalies, signifying the collective effects, are suppressed. However in the structures that exhibit a Fano resonance, the resonance is not suppressed but only experiences a spectral shift. Again I give a detailed derivation of another semi-analytical technique based on surface-current expansion that is suitable for antenna geometry.

In Chapter 4, I study the effect of the geometry and topology of the unit cells on their collective interactions by considering a meta-surface composed of a double-antenna unit cell. I find that in this structure, the effective dipole-dipole interaction is significantly modified and the transverse long-range interaction is suppressed, giving rise to the disappearance of Wood's anomalies. First-principle calculations done in COMSOL also show that such suppression of long-range interaction results in an anomalous spatial dispersion of the electric-dipolar mode, making it insensitive to the angle of incidence. In contrast, the quadrupolar mode of the antenna pair experiences strong spatial dispersion. These results show that collective effects in plasmonic metamaterials are very sensitive to the design and topology of meta-molecules. My findings, as I show in this chapter, envision the possibility of suppressing the spatial dispersion effects to weaken the dependence of the metamaterials' response on the incidence angle.

In Chapter 5, I study the possibility to convert polarization of light with ultrathin metasurfaces instead of bulky wave plates. By manipulating the symmetries of the structure, I design a multi-resonant metasurface. The interplay between the resonances enables the control over the phase of the scattered wave. By judiciously designing the metasurface, an analog of electromagnetically induced transparency (EIT) is obtained. In conventional (non-EIT) metasurfaces, resonant modes' excitation results in strong reflection of light accompanied by a significant reduction in transmission. In Fano-resonant metasurfaces with EIT, one can overcome this limitation and boost the transmission. One of the benefits of the proposed approach to polarization conversion is the spectral selectivity stemming from the fact that, in contrast to other metasurface designs [86, 118], the EIT peak, where polarization conversion takes place, is surrounded by low transmission region. Thus, the structure naturally cuts off those spectral regions where polarization conversion does not take place or is not very efficient.

In Chapter 6, I conclude the thesis by summarizing the findings of my studies of the optical properties of plasmonic meta-surfaces in infrared spectral range and the collective surface waves they support.

Chapter 2

Highly Confined Hybrid Spoof Surface Plasmons in Ultra-thin Metal/Dielectric Heterostructures

2.1 Introduction

The surface plasmon (SP) is one of the linchpins of the field of sub-diffraction optics [15]: by penetrating below the metal surface [92], electromagnetic waves can be localized beyond diffraction limit. This opens a wide range of applications in spectroscopy, photonic circuits, solar cells, and other technologically important areas [10, 23, 65]. For longer wavelengths, metals begin resembling perfect electric conductors (PECs), wave penetration into the metal becomes negligible, and other approaches to light localization and concentration must be found. It has been recently discovered [16, 38, 39, 80, 87] that SPs can be mimicked by perforating the metal surface with an array of sub-wavelength holes. Dispersion and confinement of the resulting “spoof” surface plasmons (SSPs) are defined (and can be tuned) by the holes’ size and geometry. Thus, the SSP-based approach to light confinement is crucial for bringing the advantages of plasmonics into the longer-wavelength spectral range, which is especially important for various infrared applications, including surface-enhanced infrared absorption (SEIRA) spectroscopy [62, 84], on-chip light sources [50], and infrared detectors [24, 97].

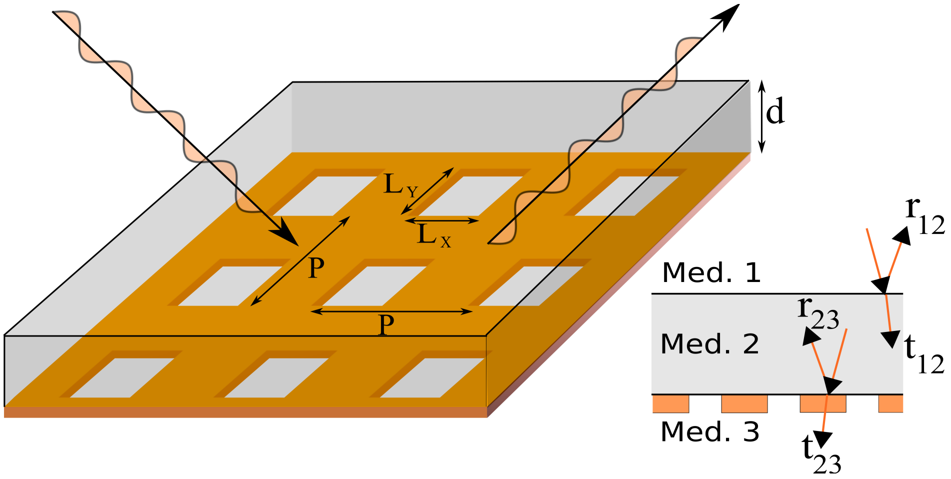

Figure 2.1: (color online). (Left) Schematic of the heterostructure supporting hybrid SSPs. (Right) Side view and definitions of the reflection/transmission coefficients used in the text.

A major drawback of SSPs supported by metal films with simple perforation geometries (e.g., circular or rectangular holes) is that they are very weakly confined for most frequencies and, therefore, are not suitable for the above applications. More sophisticated geometries that have been shown [70, 80] to improve confinement in the microwave spectral range are not practical for optical applications. In this chapter, we resolve the problem of poor confinement of conventional SSPs while retaining their important advantage: the ability to control SSP's frequency and refractive index using variable size and shape of the metal holes. This is achieved by combining metal structuring with the traditional method of electromagnetic field confinement, waveguiding. We theoretically predict and experimentally confirm that a new class of SSPs exists in the ultrathin heterostructure comprised of a slab of high-index dielectric material and a perforated metal film (Fig. 2.1). The resulting SSPs owe their unusual electromagnetic properties to their hybrid nature: the conventional SSP modes inherent to any periodic metal structure are hybridized with conventional modes of dielectric films: guided waves (GW) and leaky Fabry-Perót (FP) modes. The hybrid SSPs represent an important improvement on both conventional guided modes and SSPs: they are better confined than either one of the two (Fig. 2.3), while their spectral properties and lifetimes are controllable by the size and shape of the metallic perforations. As a specific example and possible application of the proposed concept, we demonstrate that hybrid SSPs can turn low-absorbing semiconductor (specifically, SiC) films into near-perfect absorbers of infrared radiation. The choice of SiC owes to the strong dependence of its dielectric permittivity $\epsilon_{\mathrm{SiC}}(\omega)\equiv n^2(\omega)$ on frequency $\omega\equiv 2\pi c/\lambda$: ϵ_{SiC} changes by a factor 2 as λ changes by 8% [82].

In this work, theoretical calculations and numerical modeling were performed by the author and Dr. Alexander B. Khanikaev and nanoscale sample fabrication and FTIR spectroscopy were performed by Burton Neuner III, and sample growth was performed by University Claude Bernard Lyon I collaborator Gabriel Ferro.

2.2 Theoretical description

It is instructive to start the theoretical description of hybrid SSPs by considering the eigenmodes (both leaky and fully-confined) of the *unperforated* heterostructure. Mathematically, this is done by recalling the standard Airy

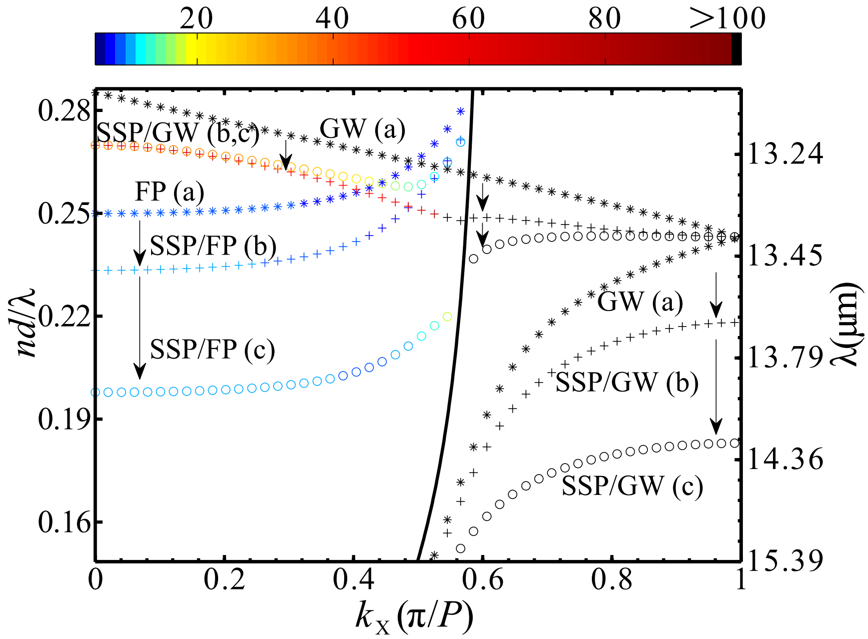

Figure 2.2: (color online). Family of dispersion curves of the p-polarized eigenmodes of the heterostructure shown in Fig. 2.1 for different hole sizes: stars (a) - unperforated metal; pluses (b) L_X=L_Y=1.2 μm; circles (c) L_X=L_Y=1.8 μm. P=3.84 μmand d=570 nm. Color: the quality factor of the modes. Solid curve is the air light line.

expression [21] for the reflectivity coefficient of the heterostructure r_{slab}:

$$r_{\text{slab}} = r_{12} + t_{12}t_{21}\ exp(2i\delta)\ r_{23}\ Z, \quad \delta = k_z d, \tag{2.1}$$

where the reflection (transmission) coefficients $r_{ij} \equiv |r_{ij}|e^{i\phi_{ij}}$ (t_{ij}) at the i-th/j-th medium interface are illustrated by Fig. 2.1, $Z \equiv 1/(1-r_{21}r_{23}e^{2i\delta})$ accounts for multiple reflections, and k_z is the propagation wave number normal to the interface. All eigenmodes of the unperforated heterostructure (including leaky and fully-guided modes) correspond to the poles of r_{slab}. These poles are given by Z^{-1}=0, giving rise to the following condition that must be satisfied by any eigenmode:

$$\phi_{21} + \phi_{23} + 2\,Re\{k_z\}d = 2\pi l, \tag{2.2}$$

where l is an integer number. Note that $\phi_{23}=\pi$ in the case of unperforated PEC film, and the phase ϕ_{21} of the Fresnel's reflection coefficient satisfies $\phi_{21}=0$ above the light line, but can depart from zero below the light line. The frequencies of the two eigenmodes found for real wavenumbers $\mathbf{k}_{||}$ along the interface correspond to: (i) the leaky FP mode above the light line, and (ii) the confined GW mode below the light line. For a specific case of a SiC film with thickness $d = 570$ nm, the dispersion relations $\omega(\mathbf{k}_{||}) \equiv \omega_r(\mathbf{k}_{||}) + i\omega_i(\mathbf{k}_{||})$ for these modes are plotted in Fig. 2.2. Because the FP mode is leaky, it has a low quality factor $Q = \omega_r/\omega_i$. However, coupling to the GW mode requires a high-index prism or a diffraction grating, and its Q is limited only by the material losses. As shown below, when the metal film is patterned, both FP and GW modes can hybridize with SSPs giving rise to highly confined modes whose spectral properties can be tuned by the size and shape of the perforations, and whose confinement drastically exceeds that of either the SSPs or the modes of the unperforated structure.

Next, we consider a periodically perforated metal film as shown in Fig. 2.1. SSPs are introduced by generalizing Eq. (2.1) to include the effects of diffraction. Specifically, using the standard scattering matrix formulation, the reflection coefficient, which connects different diffractive orders, is expressed in the matrix form:

$$\hat{r}_{\text{slab}} = \hat{r}_{12} + \hat{t}_{21}\; exp(i\hat{\delta})\; \hat{r}_{23}\; \hat{Z}\; exp(i\hat{\delta})\; \hat{t}_{12}, \tag{2.3}$$

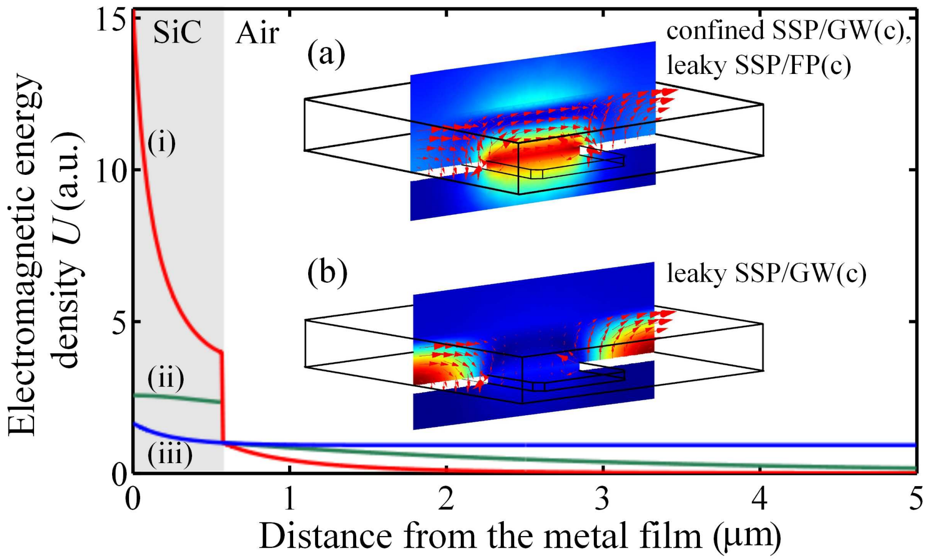

Figure 2.3: (color online). Transverse distribution of electromagnetic energy density averaged over the unit cell for the case of (i) SSP/GW of perforated heterostructure, (ii) GW of unperforated heterostructure, and (iii) SSP of uncoated perforated PEC. Parameters are the same as in Fig. 2.2. Insets show the fields corresponding to the excitation of hybrid SSPs given in Fig. 2.2.

where $\hat{Z}$ is the multi-pass matrix given by $\hat{Z} = (\hat{I} - exp(i\hat{\delta})\ \hat{r}_{21} exp(i\hat{\delta})\ \hat{r}_{23})^{-1}$. Complex eigenfrequencies of the hybrid SSPs correspond to the roots of the equation $Det\,[\hat{r}^{-1}_{\text{slab}}(\omega, \mathbf{k})]{=}0$.

2.2.1 Generalized Airy Expressions Taking Diffraction Into Account

In this subsection, we give the full derivation of Eq. (2.3). An easy way to find the reflection and transmission coefficients (S-matrices, in general) of a slab with a finite thickness is to use the S-matrices of each interface of the slab. These expressions are known as Airy expressions [21]. However the standard

Airy expression does not take the diffraction into account. Here we generalize the standard Airy expressions to take all the diffraction and waveguiding effects into consideration:

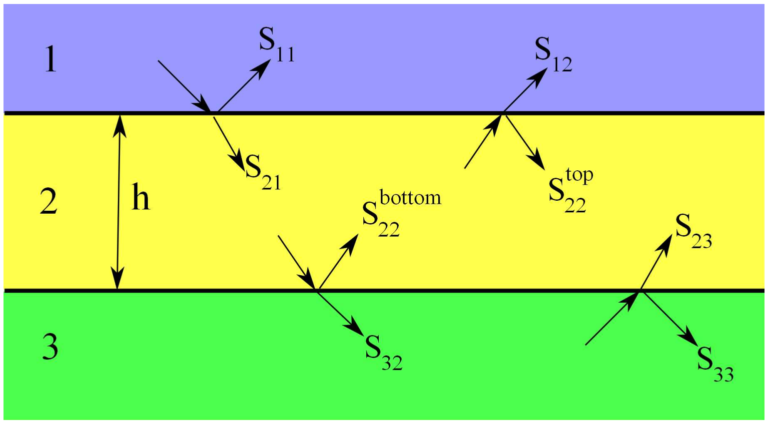

Figure 2.4: Schematics showing a slab (medium '2') of thickness h sandwiched between the semi-infinite media '1' and '3'. All the possible reflection and transmission pathways and the corresponding coefficients are shown on each interface.

$$
\begin{aligned}
\hat{S}_{11}^{\text{slab}} &= \hat{S}_{11} + \hat{S}_{12}\,\hat{\Phi}\,\hat{S}_{22}^{\text{bottom}}\,\hat{\Phi}\;\hat{S}_{21} + \hat{S}_{12}\,\hat{\Phi}\,\hat{S}_{22}^{\text{bottom}}\,\hat{\Phi}\,(\hat{S}_{22}^{\text{top}}\,\hat{\Phi}\,\hat{S}_{22}^{\text{bottom}}\,\hat{\Phi})\,\hat{S}_{21} \\
&\quad + \hat{S}_{12}\,\hat{\Phi}\,\hat{S}_{22}^{\text{bottom}}\,\hat{\Phi}\,(\hat{S}_{22}^{\text{top}}\,\hat{\Phi}\,\hat{S}_{22}^{\text{bottom}}\,\hat{\Phi})(\hat{S}_{22}^{\text{top}}\,\hat{\Phi}\,\hat{S}_{22}^{\text{bottom}}\,\hat{\Phi})\,\hat{S}_{21} + \ldots, \\
\hat{S}_{31}^{\text{slab}} &= \hat{S}_{32}\,\hat{\Phi}\;\hat{S}_{21} + \hat{S}_{32}\,\hat{\Phi}\,(\hat{S}_{22}^{\text{top}}\,\hat{\Phi}\,\hat{S}_{22}^{\text{bottom}}\,\hat{\Phi})\,\hat{S}_{21} \\
&\quad + \hat{S}_{32}\,\hat{\Phi}\,(\hat{S}_{22}^{\text{top}}\,\hat{\Phi}\,\hat{S}_{22}^{\text{bottom}}\,\hat{\Phi})(\hat{S}_{22}^{\text{top}}\,\hat{\Phi}\,\hat{S}_{22}^{\text{bottom}}\,\hat{\Phi})\,\hat{S}_{21} + \ldots, \\
\hat{S}_{33}^{\text{slab}} &= \hat{S}_{33} + \hat{S}_{32}\,\hat{\Phi}\,\hat{S}_{22}^{\text{bottom}}\,\hat{\Phi}\;\hat{S}_{23} + \hat{S}_{32}\,\hat{\Phi}\,\hat{S}_{22}^{\text{bottom}}\,\hat{\Phi}\,(\hat{S}_{22}^{\text{bottom}}\,\hat{\Phi}\,\hat{S}_{22}^{\text{top}}\,\hat{\Phi})\,\hat{S}_{23} \\
&\quad + \hat{S}_{32}\,\hat{\Phi}\,\hat{S}_{22}^{\text{bottom}}\,\hat{\Phi}\,(\hat{S}_{22}^{\text{bottom}}\,\hat{\Phi}\,\hat{S}_{22}^{\text{top}}\,\hat{\Phi})(\hat{S}_{22}^{\text{bottom}}\,\hat{\Phi}\,\hat{S}_{22}^{\text{top}}\,\hat{\Phi})\,\hat{S}_{23} + \ldots, \\
\hat{S}_{13}^{\text{slab}} &= \hat{S}_{12}\,\hat{\Phi}\;\hat{S}_{23} + \hat{S}_{12}\,\hat{\Phi}\,(\hat{S}_{22}^{\text{bottom}}\,\hat{\Phi}\,\hat{S}_{22}^{\text{top}}\,\hat{\Phi})\,\hat{S}_{23} \\
&\quad + \hat{S}_{12}\,\hat{\Phi}\,(\hat{S}_{22}^{\text{bottom}}\,\hat{\Phi}\,\hat{S}_{22}^{\text{top}}\,\hat{\Phi})(\hat{S}_{22}^{\text{bottom}}\,\hat{\Phi}\,\hat{S}_{22}^{\text{top}}\,\hat{\Phi})\,\hat{S}_{23} + \ldots, \qquad (2.4)
\end{aligned}
$$

Each of these infinite sums represents a geometric series which are converging and can be written in the following closed forms.

$$
\begin{aligned}
\hat{S}_{11}^{\text{slab}} &= \hat{S}_{11} + \hat{S}_{12}\,\hat{\Phi}\,\hat{S}_{22}^{\text{bottom}}\,\hat{\Phi}\,\hat{Z}^{\text{top}}\,\hat{S}_{21}, \\
\hat{S}_{31}^{\text{slab}} &= \hat{S}_{32}\,\hat{\Phi}\,\hat{Z}^{\text{top}}\,\hat{S}_{21}, \\
\hat{S}_{33}^{\text{slab}} &= \hat{S}_{33} + \hat{S}_{32}\,\hat{\Phi}\,\hat{S}_{22}^{\text{bottom}}\,\hat{\Phi}\,\hat{Z}^{\text{top}}\,\hat{S}_{23}, \\
\hat{S}_{13}^{\text{slab}} &= \hat{S}_{12}\,\hat{\Phi}\,\hat{Z}^{\text{bottom}}\,\hat{S}_{23}, \qquad (2.5)
\end{aligned}
$$

where

$$
\begin{aligned}
\hat{Z}^{\text{bottom}} &= \hat{I} + (\hat{S}_{22}^{\text{bottom}}\,\hat{\Phi}\,\hat{S}_{22}^{\text{top}}\,\hat{\Phi}) + (\hat{S}_{22}^{\text{bottom}}\,\hat{\Phi}\,\hat{S}_{22}^{\text{top}}\,\hat{\Phi})^2 + \ldots \\
&= \{\hat{I} - \hat{S}_{22}^{\text{bottom}}\,\hat{\Phi}\,\hat{S}_{22}^{\text{top}}\,\hat{\Phi}\}^{-1}, \\
\hat{Z}^{\text{top}} &= \hat{I} + (\hat{S}_{22}^{\text{top}}\,\hat{\Phi}\,\hat{S}_{22}^{\text{bottom}}\,\hat{\Phi}) + (\hat{S}_{22}^{\text{top}}\,\hat{\Phi}\,\hat{S}_{22}^{\text{bottom}}\,\hat{\Phi})^2 + \ldots \\
&= \{\hat{I} - \hat{S}_{22}^{\text{top}}\,\hat{\Phi}\,\hat{S}_{22}^{\text{bottom}}\,\hat{\Phi}\}^{-1}, \qquad (2.6)
\end{aligned}
$$

account for the multiple reflections inside the slab and $\hat{\Phi} = diag\{e^{i\mathbf{k}_z h}\}$ is the phase matrix, where $\mathbf{k}_z$ is the z component of the wave-vector of all the diffraction orders in the second medium where all the multiple reflections occur. In the above expressions, $\hat{I}$ is the unity matrix with the appropriate dimensions.

In the absence of diffraction and perforations, these expressions reduce to the scalar version of the Airy expressions:

$$\begin{aligned}
S_{11}^{\text{slab}} &= S_{11} + \frac{1}{D} S_{12}\,\Phi^2\,S_{22}^{\text{bottom}}\,S_{21}, \\
S_{31}^{\text{slab}} &= \frac{1}{D} S_{32}\,\Phi\,S_{21}, \\
S_{33}^{\text{slab}} &= S_{33} + \frac{1}{D} S_{32}\,\Phi^2\,S_{22}^{\text{top}}\,S_{23}, \\
S_{13}^{\text{slab}} &= \frac{1}{D} S_{12}\,\Phi\;S_{23},
\end{aligned} \tag{2.7}$$

where $D = 1 - S_{22}^{\text{bottom}} S_{22}^{\text{top}} \Phi^2$, and $\Phi = diag\{e^{ik_z h}\}$.

Also note that the scattering matrices ($\hat{S}$ matrices) relate the amplitude of incoming waves to those of the outgoing waves. Due to the diffraction effects, however, here each element of the $\hat{S}$ matrix (e.g., $\hat{S}_{11}$) is a matrix by itself relating the incoming waves in all diffracted orders to the scattered diffracted waves. For example, $(S_{11})_{ij}$ relates the amplitude of the i-th order incoming wave to that of the j-th order reflected wave.

To make a further connection of hybrid SSPs to the modes of unperforated heterostructure, we introduce two effective (tilded) complex quantities for a perforated film: $\tilde{r}_{23}\tilde{Z} \equiv (\hat{r}_{23}\hat{Z})_{00}$ and $\tilde{Z} \equiv 1/(1 - r_{21}\tilde{r}_{23}e^{2i\delta})$. By comparing Eq. (2.1) to Eq. (2.3) and by using the above definitions, we find that

$$\tilde{r}_{23} \equiv |\tilde{r}_{23}| e^{i\tilde{\phi}_{23}} = \frac{\sum}{1 + r_{21}\, e^{2i\delta}\, \sum}, \tag{2.8}$$

where $\sum \equiv \sum_{\mathbf{G}} (\hat{r}_{23})_{0\mathbf{G}}\ (\hat{Z})_{\mathbf{G}0}$ involves summation over all the reciprocal lattice vectors $\mathbf{G}$. These definitions enable us to use the scalar Eqs. (2.1, 2.2) by replacing transmission and reflection coefficients and the corresponding phases with their effective counterparts. For example, the modified resonant phase-matching condition is obtained by replacing $\phi_{23}{=}\pi$ in Eq. (2.2) with $\tilde{\phi}_{23}$, which can considerably deviate from π. As will be shown below, the size and shape of the hole can strongly influence $\tilde{\phi}_{23}$, thereby shifting the absorption peak from the Fabry-Perót resonance $d{=}\lambda_{\mathrm{FP}}/4n(\lambda_{\mathrm{FP}})$.

We calculated the scattering matrices ($\hat{r}_{23}$ and $\hat{t}_{23}$) using the semi-analytic modal matching technique (see Appendix to this chapter), and analytically continued it into the complex ω-plane. The resulting dispersion curves for hybrid SSPs both above (leaky SSPs) and below (confined SSPs) the light line are plotted in Fig. 2.2, where j=(a,b,c) labels the hole size (see caption), and the color indicates the quality factor Q of the modes.

First we focus on dispersion curves below the light line: the guided mode of the unperforated structure GW(a), and the two hybrid SSPs (SSP/GW(b) and SSP/GW(c)) whose dispersion curves are controlled by the holes' size. As the hole size increases, the dispersion curves depart from the light line, thereby indicating high spatial confinement. Flattening of the dispersion curves for larger hole sizes also indicates an increasing density of states which can be utilized for plasmon-enhanced infrared emission [50]. Strong concentration of the magnetic field of the hybrid SSP/GW mode inside the hole (Fig. 2.3 inset (a)) explains the high sensitivity of this mode to the size and shape of the hole. Figure 2.3 illustrates that the confinement of the SSP/GWs exceeds that of both classes of waves (GWs and pure SSPs without the dielectric film) from which these hybrid SSPs originate. The figure shows energy profiles of three modes at the particular subwavelength frequency, corresponding to a SSP/GW(c) mode at $k_X = \pi/P$ (i), a GW mode of the unperforated structure (ii), and a pure SSP of a thick perforated metal film surrounded by air (iii). Clearly, the hybrid SSPs have the highest confinement and the highest concentration of energy inside the dielectric film: 15% (70%) of the SSP/GW (GW) mode resides outside of the dielectric slab.

Hybridization between FP modes and SSPs produce leaky hybrid SSPs above the light line as shown in Fig. 2.2 by the progression from FP to SSP/FP modes. These hybrid *leaky* SSPs have a similar three-dimensional magnetic field profile to that of the *guided* SSP/GW modes as shown in the inset (a) to Fig. 2.3. Because fields are concentrated inside the perforation, spectral properties and the lifetime of the SSP/FP modes are strongly affected by the holes' size $L_{X,Y}$. Their transverse confinement also significantly exceeds that of FP modes as indicated by Q-factor shown by color in Fig. 2.2. The SSP/FP mode lifetime Q/ω and field confinment both increase with $L_{X,Y}$. The corresponding energy density profiles are similar to those plotted for the confined modes in Fig. 2.3. Note that, in addition to the SSP/FP modes, there is another leaky hybrid SSP labeled SSP/GW(j) above the light line whose field distribution (shown in Fig. 2.3 inset (b)) is centered outside of the hole. Therefore, the spectral position of the leaky SSP/GW modes is not strongly affected by the holes' dimensions. Because SSP/FP and SSP/GW modes are leaky above the light line, they can be experimentally observed using conventional infrared spectroscopy as presented below.

2.3 Experimental results

A SiC film of thickness d=570 nm was hetero-epitaxially grown on a Si(100) substrate wafer, and an air-bridged membrane with area (500 μm)^2 was produced after KOH back-etching of the Si substrate. SiC permittivity with parameters extracted from a fit to experimental reflectivity data is given by the analytical function:

$$\epsilon_{\text{SiC}}(\omega) = \epsilon_\infty \frac{\omega^2 - \omega_{LO}^2 + i\Gamma\omega}{\omega^2 - \omega_{TO}^2 + i\Gamma\omega} + \frac{i\sigma}{\omega}, \tag{2.9}$$

where $\epsilon_\infty = 6.5$, ω_{LO}=972 cm^{-1}, ω_{TO}=796 cm^{-1}, Γ=5 cm^{-1}, and σ=500 cm^{-1}. Figure 2.5 shows the real and imaginary part of the refractive index $n_{\text{SiC}} = \sqrt{\epsilon_{\text{SiC}}}$. Due to the low doping level of SiC, a low-loss response of SiC is obtained which is indicated by the small fraction of the imaginary part to the real part of the refractive index as can be seen from Fig. 2.5. The aim of this study was to show how excitation of highly confined spoof plasmons can enhance this low absorption.

Next, a 100 nm Au film was thermally deposited on the newly exposed

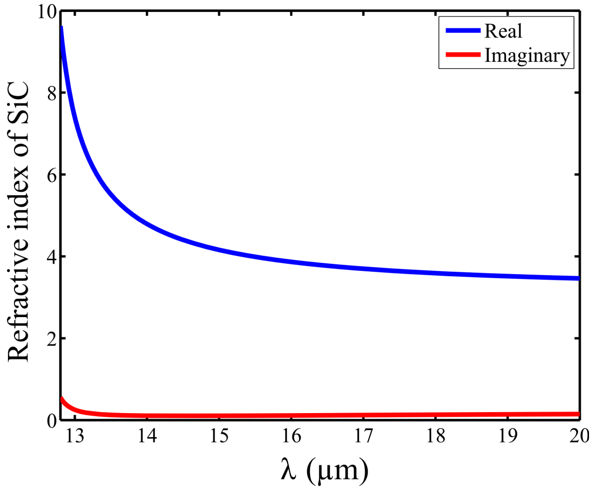

Figure 2.5: (color online). Real and imaginary parts of the refractive index of doped SiC $n_{SiC} = \sqrt{\epsilon_{SiC}}$ where ϵ_{SiC} is given in Eq. (2.9) with the following parameters: $\epsilon_\infty = 6.5$, ω_{LO}=972 cm^{-1}, ω_{TO}=796 cm^{-1}, Γ=5 cm^{-1}, and σ=500 cm^{-1}.

side of the SiC. Metal perforations were produced using a focused ion beam over a (100 μm)^2 area. Optical characterization (reflection, transmission) was performed using a Thermo Scientific Continuum microscope coupled to a Nicolet 6700 FTIR Spectrometer. In all measurements, transmission was less than 10%. Therefore, we will focus on reflectivity $R(\lambda)$ and absorptivity $A(\lambda)$ spectra for the rest of this chapter. First, $R(\lambda)$ prior to perforating the metal film was measured which is shown by dot-dashed lines in Fig. 2.6. The broad reflection dip at λ_{FP}=13.3 μm corresponds to coupling to FP mode.

Next, $R(\lambda)$ and $A(\lambda) = 1 - R(\lambda) - T(\lambda)$ for the perforated metal structures were measured and plotted alongside the results of the finite-elements COMSOL simulations in Fig. 2.6. Two hole sizes were used as perforations:

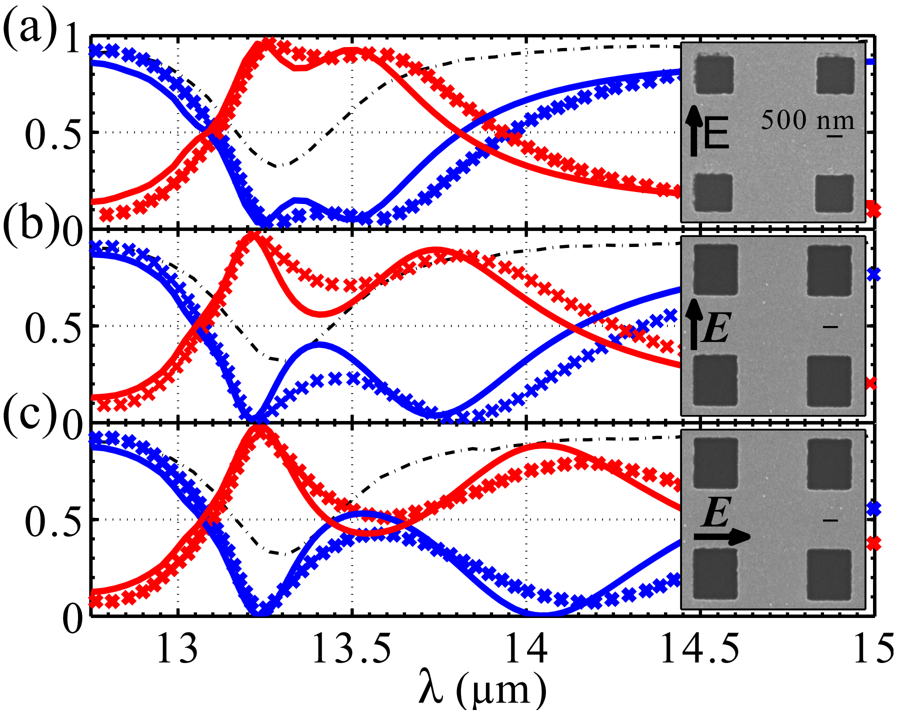

Figure 2.6: (color online). Reflection (blue) and absorption (red) curves obtained from experimental measurements (crosses) and finite-element simulations (lines) for different hole dimensions $L_X \times L_Y$ and incident light polarizations. (a) L_X=L_Y=1.2 μm, polarization-independent; (b) L_X=1.45 μm, L_Y=1.75 μm, y-polarized; (c) L_X=1.45 μm, L_Y=1.75 μm, x-polarized. Black dash-dotted curves: reflection from unperforated Au film/SiC structure. Courtesy of Dr. Burton Neuner III.

small square holes (Fig. 2.6(a)) and larger rectangular holes (Fig. 2.6(b,c)). As predicted by the theory of hybrid SSPs, reflectivity curves reveal two reflection minima, which also correspond to absorption maxima. Thus, the metal perforation causes $R(\lambda)$ to drop to zero and absorption $A(\lambda)$ to reach nearly unity. The physical reason for this enhanced absorptivity is resonant coupling to leaky SSP/FP (long-wavelength peak) and SSP/GW (short-wavelength peak) modes.

Experimental results confirm that the spectral position of the SSP/GW dip (λ=13.25 μm) is almost independent of the size/shape of the holes, while that of SSP/FP dip is very sensitive to hole size and, for rectangular holes, is polarization-sensitive. The SSP/FP absorption peak (e.g., at λ=14.20 μm for light polarized along the short dimension of the large rectangular hole) is especially remarkable because it occurs far from the FP resonance in the spectral region where SiC is not very absorptive: n=4.6+0.04i. Without perforation, the round-trip absorptivity of the d=λ/25 SiC film is only $8\pi\,\mathrm{Im}(n)\,d/\lambda$=4%. This absorption enhancement is caused by the excitation of the high-Q SSP/FP mode which strongly traps and enhances the electromagnetic field inside the weakly-absorbing film, turning it into a "perfect" absorber.

2.4 More Complex Geometries

Another degree of freedom to confine electromagnetic energy is to use more sophisticated hole shapes that exhibit site (or shape) resonances [70, 80]. For example, a strong confinment even in a thinner heterostructures can be accomplished by employing relatively simple (and feasible for fabrication) U-shaped holes [96] shown in Fig. 2.7(a). For instance, in the case of the SSP/FP resonance, use of U-shaped holes causes even more dramatic red-shifting which facilitates trapping of electromagnetic fields by a subwavelength thick heterostructure. A family of reflectivity spectra shown in Fig. 2.7(b) correspond to U-shapes with increasing metal "tongue" length t (see inset to Fig. 2.7(a)).

The figure indicates that, counter-intuitively, the spectral position of the reflection dip red-shifts even as the remaining hole area decreases with increasing t. This effect is due to the LC-like resonances of the U-shape occurring for electric field polarized parallel to the tongue [96]. This resonance manifests itself in the increased effective reflection phase $\tilde{\phi}_{23}$. $\tilde{\phi}_{23}$ obtained for both rectangular and U-shaped holes at the respective reflectivity dips is shown by crosses and circles in Fig. 2.7(a) as a function of L_X and t, respectively. The U-shape's parameter t has a more pronounced effect on $\tilde{\phi}_{23}$ (and, by extension, on the spectral position of the reflection dip) than the overall size L_X of the rectangular hole. In the latter case, the reflection phase $\tilde{\phi}_{23}$ saturates around the value of 1.25π, while in the case of the U-shaped holes, $\tilde{\phi}_{23}$ approaches $3\pi/2$, with high value of $d\tilde{\phi}_{23}/dt$ indicating strong sensitivity to the geometry of the U-shape.

2.5 Conclusion

In conclusion, we have predicted and experimentally demonstrated that a heterostructure comprised of a periodically perforated metal film coated with high-index dielectric layer supports strongly confined hybrid spoof surface plasmons. This extraordinary confinement is achieved through hybridization between two weakly confined sets of modes: SSPs supported by the perforated metal film and guided modes supported by the dielectric layer. Hybrid SSPs retain tunability due to strong sensitivity to the holes' size and shape. As an experimental proof of principle, we have demonstrated that hybrid SSPs can

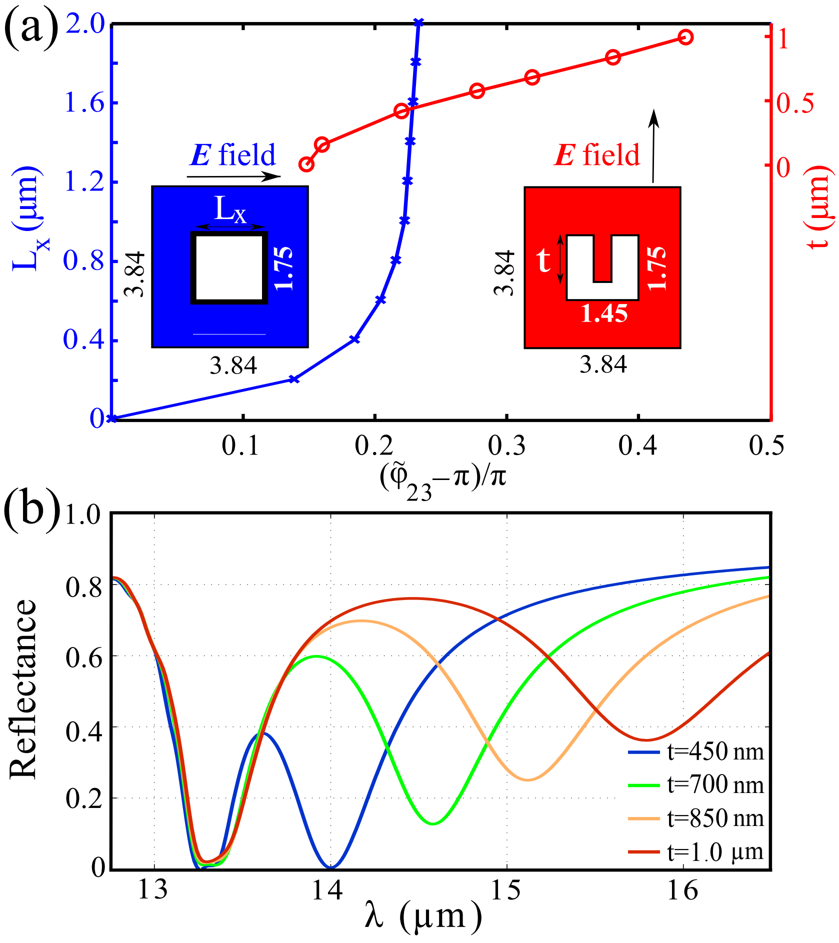

Figure 2.7: (color online). (a) Reflection phase shift $\tilde{\phi}_{23}$ at the reflectivity minima for (i) rectangular holes as the function of L_X (crosses), and (ii) U-shaped holes as the function of t (circles). (b) Family of reflection spectra (different values of t (nm)) for the U-shaped holes.

turn weakly-absorbing ultra-thin semiconductor films into spectrally-tunable "perfect" absorbers. Hybrid SSPs may find practical applications in multi-spectral infrared imaging, thermophotovoltaics, on-chip light sources, and infrared detectors.

2.6 Appendix: A Semi-Analytical Technique to Derive Reflection and Transmission From Meta-Surfaces With Semi-Infinite Periodic Holes

In this section, we will explain in detail a semi-analytical technique to find the coefficients of reflection from, and transmission through, a thick metallic layer with a two-dimensional array of rectangular holes perforated in it, (see Fig. 2.8) for all the resulting diffracted orders. Here we will assume that the superstrate is an isotropic semi-infinite dielectric medium with a dielectric permittivity of ϵ_d and the substrate is a semi-infinite perfect electric conductor perforated by a periodic arrangement of holes with a dielectric permittivity of ϵ_h.

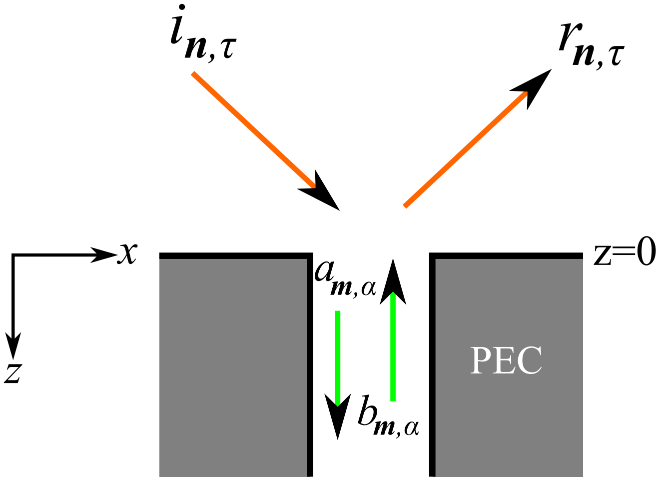

Figure 2.8: (a) Side-view schematics of the interface between a semi-infinite dielectric medium and a semi-infinite perfect electric conductor layer with periodic holes cut into it. The amplitudes of the incident and reflected waves in the dielectric medium and the transmitted wave in the holes (waveguides) are shown by $i_{\mathbf{n},\tau}$, $r_{\mathbf{n},\tau}$, and $a_{\mathbf{m},\alpha}$. For the case of incidence from the top, $b_{\mathbf{m},\alpha}$ will be assumed to be zero. The interface between the two media is at $z = 0$.

2.6.1 Modes Of An Isotropic Dielectric Medium

Using the periodicity of the structure, the tangential components of the fields are expanded in the superstrate in the plane-wave basis in terms of the amplitudes of the incident ($i_{\mathbf{n},\tau}$), reflected ($r_{\mathbf{n},\tau}$) fields:

$$\begin{aligned} \mathbf{E}_{\|}^{\mathrm{I}} &= \sum_{\mathbf{n},\tau} (i_{\mathbf{n},\tau}\, e^{ik_z^{\mathbf{n}} z} + r_{\mathbf{n},\tau}\, e^{-ik_z^{\mathbf{n}} z})\, |\mathbf{n},\tau\rangle, \\ -\hat{z}\times\mathbf{H}_{\|}^{\mathrm{I}} &= \sum_{\mathbf{n},\tau} Y_{\mathbf{n},\tau}(i_{\mathbf{n},\tau}\, e^{ik_z^{\mathbf{n}} z} - r_{\mathbf{n},\tau}\, e^{-ik_z^{\mathbf{n}} z})\, |\mathbf{n},\tau\rangle, \end{aligned} \tag{2.10}$$

where $|\mathbf{n},\tau\rangle = |n_x, n_y, \tau\rangle$ represents the in-plane (tangential) electric field of the $\mathbf{n}$-th diffracted plane wave with an in-plane wave-number $\mathbf{k}_{\|}^{\mathbf{n}} = (k_x^{\mathbf{n}}, k_y^{\mathbf{n}})$, a polarization state τ (s or p polarization) and a wave admittance $Y_{\mathbf{n},\tau}$. The wave admittance of an s-polarized plane wave is $Y_{\mathbf{n},s} = k_z^{\mathbf{n}}/k_0$ and that of a p-polarized plane wave is $Y_{\mathbf{n},p} = \epsilon_d k_0/k_z^{\mathbf{n}}$. In the above expressions, $k_x^{\mathbf{n}} = 2\pi n_x/P_x$, $k_y^{\mathbf{n}} = 2\pi n_y/P_y$, and $k_z^{\mathbf{n}} = \sqrt{\epsilon_d k_0^2 - (k_{\|}^{\mathbf{n}})^2}$ are respectively the x, y, and z components of the wavevector $\mathbf{k}^{\mathbf{n}}$. k_0 is the wavenumber of the wave in vacuum and ϵ_d is the relative permittivity of the medium in which the wave is propagating. The spatial representation of $|\mathbf{n},\tau\rangle$ is given by:

$$\big\langle \mathbf{r}_{\|} \,|\mathbf{n}, s\big\rangle = \frac{\exp{(ik_x^{\mathbf{n}}x + ik_y^{\mathbf{n}}y)}}{k_{\|}^{\mathbf{n}}\sqrt{P_xP_y}}\{k_y^{\mathbf{n}}\hat{x} - k_x^{\mathbf{n}}\hat{y}\}, \tag{2.11}$$

$$\big\langle \mathbf{r}_{\|} \,|\mathbf{n}, p\big\rangle = \frac{\exp{(ik_x^{\mathbf{n}}x + ik_y^{\mathbf{n}}y)}}{k_{\|}^{\mathbf{n}}\sqrt{P_xP_y}}\{k_x^{\mathbf{n}}\hat{x} + k_y^{\mathbf{n}}\hat{y}\}. \tag{2.12}$$

2.6.2 Modes Of A Rectangular Waveguide

The fields inside the waveguides (holes) can be expanded in the waveguide-modes basis in terms of the amplitudes of the transmitted ($a_{\mathbf{m},\alpha}$) and incident

($b_{\mathbf{m},\alpha}$) waves. For the case of incidence from the dielectric layer, we will assume $b_{\mathbf{m},\alpha} = 0$ later in the derivation. But for now, we will keep the expressions more general:

$$\begin{aligned} \mathbf{E}_{\|}^{\mathrm{II}} &= \sum_{\mathbf{m},\alpha} (a_{\mathbf{m},\alpha}\, e^{i\beta^{\mathbf{m}} z} + b_{\mathbf{m},\alpha}\, e^{-i\beta^{\mathbf{m}} z})\, |\mathbf{m},\alpha\rangle, \\ -\hat{z} \times \mathbf{H}_{\|}^{\mathrm{II}} &= \sum_{\mathbf{m},\alpha} Y_{\mathbf{m},\alpha} (a_{\mathbf{m},\alpha}\, e^{i\beta^{\mathbf{m}} z} - b_{\mathbf{m},\alpha}\, e^{-i\beta^{\mathbf{m}} z})\, |\mathbf{m},\alpha\rangle, \end{aligned} \tag{2.13}$$

where $\beta^{\mathbf{m}} = \sqrt{\epsilon_h k_0^2 - (\frac{m_x \pi}{a_x})^2 - (\frac{m_y \pi}{a_y})^2}$ is the propagation constant of the $\mathbf{m}$-th waveguide mode, independent of its polarization α=(s or p). $|\mathbf{m},\alpha\rangle = |m_x, m_y, \alpha\rangle$ represents the in-plane (tangential) electric field of the $\mathbf{m}$-th waveguide mode with a polarization state α ($s = TE$ or $p = TM$ polarization) and a wave admittance $Y_{\mathbf{m},\alpha}$. The wave admittance of an s-polarized waveguide mode is $Y_{\mathbf{m},s} = \beta^{\mathbf{m}}/k_0$ and that of a p-polarized waveguide mode is $Y_{\mathbf{m},p} = \epsilon_h k_0/\beta^{\mathbf{m}}$. In the above expressions, ϵ_h is the relative permittivity of the medium inside the holes. The spatial representation of $|\mathbf{m},\alpha\rangle$ can be found from a scalar field $A_{s/p}(x,y,z)$ [28],

$$\begin{aligned} \langle \mathbf{r}_{\|} | \mathbf{m}, s \rangle &= \{-\frac{1}{\epsilon_0 \epsilon_h} \partial_y A_s\}\hat{x} + \{\frac{1}{\epsilon_0 \epsilon_h} \partial_x A_s\}\hat{y}, \\ \langle \mathbf{r}_{\|} | \mathbf{m}, p \rangle &= \{\frac{ic}{k_0 \epsilon_h} \partial_{xz}^2 A_p\}\hat{x} + \{\frac{ic}{k_0 \epsilon_h} \partial_{yz}^2 A_p\}\hat{y}, \end{aligned} \tag{2.14}$$

where $A_s(x,y,z)$ and $A_p(x,y,z)$ are given by:

$$\begin{aligned} A_s &= \cos(g_x^{\mathbf{m}}\, x)\, \cos(g_y^{\mathbf{m}}\, y)\, e^{i\beta^{\mathbf{m}} z}, \\ A_p &= \sin(g_x^{\mathbf{m}}\, x)\, \sin(g_y^{\mathbf{m}}\, y)\, e^{i\beta^{\mathbf{m}} z}, \end{aligned} \tag{2.15}$$

where $g_x^{\mathbf{m}} = m_x\pi/a_x$ and $g_y^{\mathbf{m}} = m_y\pi/a_y$. Note that, in the case of the s (TE) polarization, ($m_x \geq 0$, $m_y \geq 0$) excluding m_x=m_y=0. In the case of p (TM) polarization, ($m_x, m_y \geq 1$). Also note that the above-mentioned form of $|\mathbf{m}, \alpha\rangle$ should be normalized to the hole area such that $\langle \mathbf{m}, \alpha | \mathbf{m}, \alpha \rangle = \int_{\text{hole}} |\left\langle \mathbf{r}_\parallel | \mathbf{m}, \alpha \right\rangle|^2 \, d^2\mathbf{r}_\parallel = 1$. The normalization factor $N_{\mathbf{m}}$ is given by:

$$N_{\mathbf{m}} = \frac{a_x a_y}{4} \{g_y^2 \, (1 + (0)^{m_x}) + g_x^2 \, (1 + (0)^{m_y})\}; \tag{2.16}$$

2.6.3 Boundary conditions

By applying the appropriate boundary conditions, one can relate the reflected and transmitted fields to the incident field. The boundary conditions of the boundary at $z = 0$ are the continuity of the electric field over the whole unit cell and that of the magnetic field over only the holes. To demonstrate the applicability of each boundary condition in its particular region of the interface, we will define a function $f(x, y)$ which is unity on the holes and zero otherwise. In this language, the boundary conditions are:

$$\begin{aligned} \mathbf{E}_\parallel^{\mathrm{I}} &= f(x,y)\mathbf{E}_\parallel^{\mathrm{II}}, \\ f(x,y)\,(\hat{z} \times \mathbf{H}_\parallel^{\mathrm{I}}) &= f(x,y)\,(\hat{z} \times \mathbf{H}_\parallel^{\mathrm{II}}), \end{aligned} \tag{2.17}$$

which ensures the vanishing electric field on the PEC part of the interface as well. Applying the above-mentioned boundary conditions gives rise to the following relations between the field amplitudes:

$$\begin{aligned} i_{\mathbf{n},\tau} + r_{\mathbf{n},\tau} &= \sum_{\mathbf{m},\alpha} \langle \mathbf{n},\tau|\mathbf{m},\alpha\rangle \, (a_{\mathbf{m},\alpha} + b_{\mathbf{m},\alpha}), \\ \sum_{\mathbf{n},\tau} \langle \mathbf{m},\alpha|\mathbf{n},\tau\rangle \, Y_{\mathbf{n},\tau} \, (i_{\mathbf{n},\tau} - r_{\mathbf{n},\tau}) &= Y_{\mathbf{m},\alpha} \, (a_{\mathbf{m},\alpha} - b_{\mathbf{m},\alpha}) \end{aligned} \tag{2.18}$$

2.6.4 S Matrices

By defining the vectors $\mathbf{i} = \{i_{\mathbf{n},\tau}\}$, $\mathbf{r} = \{r_{\mathbf{n},\tau}\}$, $\mathbf{a} = \{a_{\mathbf{m},\alpha}\}$, and $\mathbf{b} = \{b_{\mathbf{m},\alpha}\}$ and the matrices $\hat{O} = \{\langle \mathbf{n},\tau|\mathbf{m},\alpha\rangle\}$, $\hat{Y}_d = \mathrm{diag}\{Y_{\mathbf{n},\tau}\}$, and $\hat{Y}_h = \mathrm{diag}\{Y_{\mathbf{m},\alpha}\}$, the following matrix equations are derived:

$$\begin{aligned} \mathbf{i} + \mathbf{r} &= \hat{O} \, (\mathbf{a} + \mathbf{b}), \\ \hat{O}^{\dagger} \, \hat{Y}_d \, (\mathbf{i} - \mathbf{r}) &= \hat{Y}_h (\mathbf{a} - \mathbf{b}), \end{aligned} \tag{2.19}$$

It is worthwhile mentioning that $\hat{O}$ is the overlap between the waveguide modes $|\mathbf{m},\alpha\rangle$ and the diffracted waves $|\mathbf{n},\tau\rangle$ which will be calculated in the next section. Now we give the $\hat{S}$ matrices of this structure. Scattering-matrix or $\hat{S}$-matrix relates the amplitudes of the incoming waves to those of the outgoing (scattered) waves (see Fig. 2.4). For example, $\hat{S}_{11}$ relates the incident wave (only from the medium '1') to the reflected wave according to $\mathbf{r} = \hat{S}_{11}\mathbf{i}$. For this, one has to set $\mathbf{b} = 0$ and solve for $\mathbf{r}$ in terms of $\mathbf{i}$. Below I give all the four $\hat{S}$ matrices of the structure with the following definitions for the $\hat{S}$ matrices:

(1) $\mathbf{r} = \hat{S}_{11}\mathbf{i}$, (2) $\mathbf{a} = \hat{S}_{21}\mathbf{i}$, (3) $\mathbf{a} = \hat{S}_{22}\mathbf{b}$, and (4) $\mathbf{r} = \hat{S}_{12}\mathbf{b}$ (see Fig. 2.8).

$$\begin{aligned}
\hat{S}_{11} &= -(\hat{I} + \hat{M})^{-1}(\hat{I} - \hat{M}), \\
\hat{S}_{21} &= \hat{O}^{-1}(\hat{I} + \hat{S}_{11}), \\
\hat{S}_{22} &= (\hat{I} + \hat{M}')^{-1}(\hat{I} - \hat{M}'), \\
\hat{S}_{12} &= \hat{O}(\hat{I} + \hat{S}_{22}),
\end{aligned} \tag{2.20}$$

where $\hat{M} = \hat{O}\,\hat{Y}_h^{-1}\,\hat{O}^{\dagger}\,\hat{Y}_d$ and $\hat{M}' = \hat{O}^{-1}\,\hat{M}\,\hat{O}$. Note that, because of the diffraction effects, here, each element of the $\hat{S}$ matrix (e.g., $\hat{S}_{11}$) is also a matrix, relating the amplitude of the incoming waves of all diffracted orders to those of the outgoing waves of all orders.

2.6.5 Expressions For Overlap Matrices

The overlap matrix $\hat{O} = \{\langle \mathbf{n}, \tau | \mathbf{m}, \alpha \rangle\}$ is the overlap between the waveguide modes $|\mathbf{m}, \alpha\rangle$ (order $\mathbf{m}$ and polarization α, inside medium ‘2’, bottom medium in Fig. 2.8) and the diffracted waves $|\mathbf{n}, \tau\rangle$ (diffracted order $\mathbf{n}$ and polarization τ, inside medium ‘1’, top medium in Fig. 2.8). The specific form of the overlap matrix $\hat{O}$ depends on the shape of the holes. Here we will consider only the rectangular holes. For circular holes, also, the overlap matrix can be found analytically [95], however, for more complicated geometries, the overlap can only be found numerically which is beyond the scope of this dissertation. For the rectangular geometry, the overlap matrix elements $O_{\mathbf{n},\tau;\mathbf{m},\alpha}$

are given:

$$\begin{aligned} O_{\mathbf{n},\tau;\mathbf{m},\alpha} &= \langle \mathbf{n},\tau | \mathbf{m},\alpha \rangle \\ &= e_x^{\mathrm{I}}(\mathbf{n},\tau)\, e_x^{\mathrm{II}}(\mathbf{m},\alpha)\, I_{cx}(\mathbf{n},\mathbf{m})\, I_{sy}(\mathbf{n},\mathbf{m}) \\ &+ e_y^{\mathrm{I}}(\mathbf{n},\tau)\, e_y^{\mathrm{II}}(\mathbf{m},\alpha)\, I_{sx}(\mathbf{n},\mathbf{m})\, I_{cy}(\mathbf{n},\mathbf{m}). \end{aligned} \tag{2.21}$$

where

$$I_{cx}(\mathbf{n},\mathbf{m}) = -ik_x^{\mathbf{n}} \frac{1-(-1)^{m_x}\exp(-ia_x k_x^{\mathbf{n}})}{(k_x^{\mathbf{n}})^2-(g_x^{\mathbf{m}})^2} \tag{2.22}$$

$$I_{cy}(\mathbf{n},\mathbf{m}) = -ik_y^{\mathbf{n}} \frac{1-(-1)^{m_y}\exp(-ia_y k_y^{\mathbf{n}})}{(k_y^{\mathbf{n}})^2-(g_y^{\mathbf{m}})^2} \tag{2.23}$$

$$I_{sx}(\mathbf{n},\mathbf{m}) = -g_x^{\mathbf{m}} \frac{1-(-1)^{m_x}\exp(-ia_x k_x^{\mathbf{n}})}{(k_x^{\mathbf{n}})^2-(g_x^{\mathbf{m}})^2} \tag{2.24}$$

$$I_{sy}(\mathbf{n},\mathbf{m}) = -g_y^{\mathbf{m}} \frac{1-(-1)^{m_y}\exp(-ia_y k_y^{\mathbf{n}})}{(k_y^{\mathbf{n}})^2-(g_y^{\mathbf{m}})^2}. \tag{2.25}$$

and

$$\begin{aligned} &e_x^{\mathrm{I}}(\mathbf{n},s) = -\frac{k_y^{\mathbf{n}}}{\sqrt{P_x P_y k_{\parallel}^{\mathbf{n}}}}, \quad e_y^{\mathrm{I}}(\mathbf{n},s) = \frac{k_x^{\mathbf{n}}}{\sqrt{P_x P_y k_{\parallel}^{\mathbf{n}}}}, \\ &e_x^{\mathrm{I}}(\mathbf{n},p) = \frac{k_x^{\mathbf{n}}}{\sqrt{P_x P_y k_{\parallel}^{\mathbf{n}}}}, \quad e_y^{\mathrm{I}}(\mathbf{n},p) = \frac{k_y^{\mathbf{n}}}{\sqrt{P_x P_y k_{\parallel}^{\mathbf{n}}}}, \\ &e_x^{\mathrm{II}}(\mathbf{m},s) = g_y^{\mathbf{m}}, \quad e_y^{\mathrm{II}}(\mathbf{m},s) = -g_x^{\mathbf{m}}, \\ &e_x^{\mathrm{II}}(\mathbf{m},p) = g_x^{\mathbf{m}}, \quad e_y^{\mathrm{II}}(\mathbf{m},p) = g_y^{\mathbf{m}}. \end{aligned} \tag{2.26}$$

$e_{x/y}^{\mathrm{I/II}}$ and $I_{c/s,x/y}$ are introduced here for expressions conciseness. The subscripts c and s in I refer to the shape of the waveguide modes (cosine-like or sine-like).

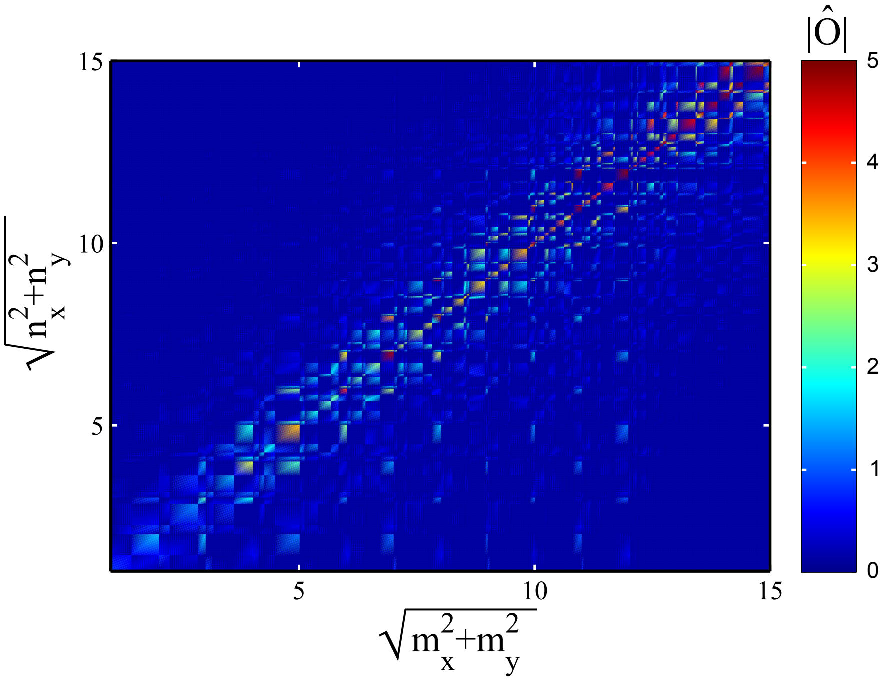

Figure 2.9: Absolute value of the overlap matrix elements showing the importance of the diagonal elements representing the phenomenon of relative convergence. Here P_x=4.22 μm, P_y=5.45 μm, a_x=2.14 μm, a_y=2.65 μm, ϵ_h=1, ϵ_d=1, and the incidence is normal to the metasurface.

2.6.6 Absolute and Relative Convergences

In order to obtain the correct value of the S-matrices, an enough number of diffraction orders and waveguide modes should be considered. Other than this “absolute” convergence, one should pay attention to “relative” convergence as well. That is, for a given number of the diffraction orders, too many waveguide modes should not be taken into account. The opposite also holds. Relative convergence is a well known phenomenon arising in the solution of truncated double-infinite sets of equations [51, 111]. In order to alleviate this problem, approximately the same number of diffraction orders and waveguide modes should be used as can be seen from Fig. 2.9 which shows that the elements that contribute the most are the ones that lay close to the diagonal ($m \approx n$) of the matrix. However, the minimal contribution of the elements far from the diagonal introduces instability and, therefore, should be avoided.

Chapter 3

Substrate Effects

3.1 Introduction

Optical nanostructures exhibiting Fano resonances have attracted a significant attention of the research community in recent years [30, 31, 35, 47, 68, 71, 76, 85, 98, 108, 114, 118]. As classical analogues of quantum Fano system [33], these systems represent elegant tabletop tools for testing fundamental principles of physics [9]. From the applications' point of view, the possibility to trap, enhance, and manipulate light in optical Fano nanostructures and metamaterials is also very promising and has already been demonstrated to be beneficial in sensing and bio-sensing [2, 64, 113, 116], photovoltaics and thermo-photovoltaics [10, 44, 94], and slow-light generation [114].

Fano resonances in optical metamaterials originate from electromagnetic interactions between their constituents. According to the type of interaction, Fano resonances can be classified into two groups: (a) coherent Fano resonances which are the result of interferences between all of the meta-atoms forming a periodic array, and (b) local Fano resonances which originate from the complex local structure of individual meta-atoms. While for the first class of these resonances, periodic arrangement of a large number of meta-molecules

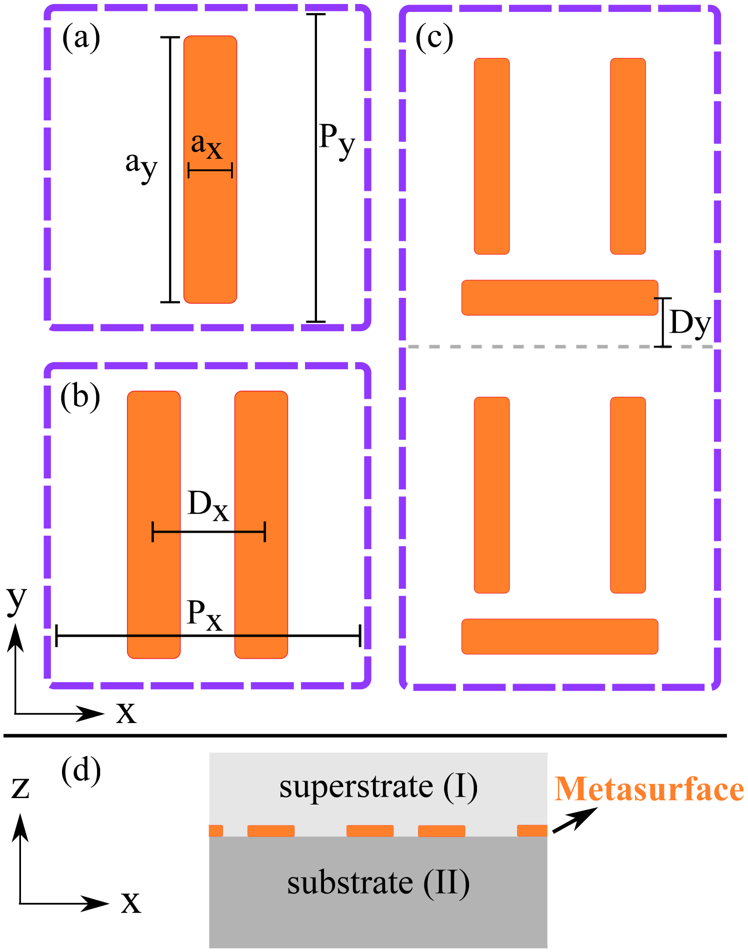

Figure 3.1: (Color online.) Schematic unit cell of the three structures considered in this chapter: (a) single-antenna, (b) double-antenna, and (c) dolmen metasurfaces. In (c), two unit cells (separated by a dashed line) are shown. (d) shows the side view of the metasurfaces cladded by the superstrate and the substrate.

is crucial, for the second class, even a single meta-molecule may exhibit a Fano resonance [71]. However, in both cases the response of the meta-surface will depend on the dielectric environment. For coherent metamaterials, it is well-known that the presence of a substrate modifies the far-field interactions[4, 36], which substantially alters the collective response. However, even in the case of local Fano resonances, the presence of a substrate can significantly modify the interaction between the meta-molecule's constituents[90]. Thus, understanding of substrate effects in both cases is critical for basic understanding of Fano resonances in experimentally relevant systems.

The geometry of the systems with Fano resonances can vary from simple designs such as metal nanoparticles [71] and perforated films [32, 43, 99] to structures with complex geometries such as oligomers and dolmens [9, 30, 31, 108].

The simplest approach to describe the Fano resonances is a mechanical toy model of coupled harmonic oscillators [68, 88, 114, 118]. In many cases, such model provides sufficient insight into the physics of the system; it allows one to fit optical spectra and associate spectral features of the system with the known properties of the mechanical Fano model. Nevertheless, such simplified representation of a complex physical system neglects various effects relevant for real structures. Among these are substrate effects, effects of periodicity resulting in a collective character of the electromagnetic response of meta-materials, geometry/proximity effects modifying the interactions between meta-molecules.

Another analytical description applicable to some relatively simple systems, such as arrays of point-like dipoles, is offered by a dipole model [11, 38, 85, 121, 122]. Indeed, a few of the above-mentioned phenomena, including collective effects and Fano resonances, can be adequately described by this model [78]. However, there are situations when the dipole model is inadequate. For instance, as soon as the scatterers or the metamolecules forming the array become comparable in size to the wavelength of light, the dipole-dipole interaction mechanism breaks down because interactions through higher multipoles come into play. Incorporating substrate effects also represents a challenge for the dipole model. To resolve these problems, the dipole model has been extended by including effects of higher multipoles [100], found with the use of numerically calculated polarizabilities of metamolecules and by applying the scattering-matrix technique [12, 16, 101]. However, after such generalizations, the dipole model can no longer be considered analytical. To fully account for all the above-mentioned effects, the approach which is being widely used is to apply a powerful yet time consuming ab-initio numerical solvers of the Maxwell equations, or various generalizations of hybrid numerical/analytical approaches [37].

However, there is another very promising semi-analytical yet rigorous approach based on the modal-matching technique (MMT). MMT has been proven to be very fruitful for describing various electromagnetic systems ranging from frequency-selective surfaces and antenna arrays in radio frequency domain [26] to perforated metallic structures [49, 55, 74, 77]. In both cases, the approach is relying on the expansion of a system-specific polarization (e.g., the total current in the antennas or the fields inside the holes) in the form of a superposition of the eigenmodes satisfying appropriate boundary conditions. It is important that, because the basis used for the expansion takes into account meta-molecules' geometry, this approach can account for the geometry-specific effects, including shape resonances and proximity effects [66, 91].

In this chapter, the semi-analytical MMT based on the current expansion [26] is applied to study Fano resonances in two-dimensional periodic arrays of metallic antennas on a substrate (Fig. 3.1). The emphasis is on arrays of complex antennas resonant in the mid-IR part of optical spectrum, which is important for bio-sensing [2, 113] and thermo-photovoltaic applications [10, 44, 94]. MMT is shown to capture the meta-molecule geometry as well as the substrate effects and is easily expandable to the cases of more complex geometries composed of several spatially extended scatterers per unit cell. We develop a minimal model of the MMT by truncating the electric-current basis of the full model and demonstrate that even the resulting analytical model is capable to quantitatively describe the optical properties of the structures. The main emphasis of the chapter is on the effect of the substrate. It is demonstrated that with the model in hand the MMT can predict the spectral positions of the resonances and describe the interference among the different scattering pathways provided by the different metamolecule's resonances.

In this work, theoretical calculations, analytical techniques, and numerical modeling were performed by the author and Dr. Alexander B. Khanikaev.

The rest of the chapter is organized as follows. In Section II a general MMT based on the Rayleigh and current expansions is derived. In Section III a minimal model is developed and applied to study a periodic single-antenna metasurface (SAM), shown in Fig. 3.1a. In Section IV we analyze periodic double-antenna meta-surfaces (DAMs) [Fig. 3.1b], which are known to exhibit a Fano resonance due to the interference of the modes corresponding to symmetric and anti-symmetric charge distributions in the antenna pairs. Finally, in Section V a dolmen structure formed by three antennas (Fig. 3.1c) and known to exhibit a plasmonic analogue of electromagnetically induced transparency (EIT) [68, 118] is studied.

3.2 Modal Matching Technique: Theoretical Formalism

In this section the electric current expansion technique is generalized to the case of infinitesimally thin metallic antennas of finite surface conductivity. Following Ref. [26], we rely on the current expansion, but require the current in the plasmonic antennas to be defined by the high-frequency conductivity of the metal and the electric field right on the antennas' surface. To make the expressions more compact and keep the formulation more general, the Dirac notation is used. Using the periodicity of the structures the tangential components of the fields are expanded in the superstrate (I) and the substrate (II) in the plane-wave basis in terms of the amplitudes of the incident ($i_{\mathbf{n},\tau}$), reflected ($r_{\mathbf{n},\tau}$), and transmitted ($t_{\mathbf{n},\tau}$) fields,

$$\begin{aligned}
\mathbf{E}_{\parallel}^{\mathrm{I}} &= \sum_{\mathbf{n},\tau} (i_{\mathbf{n},\tau} e^{ik_z^{\mathbf{n},\mathrm{I}} z} + r_{\mathbf{n},\tau} e^{-ik_z^{\mathbf{n},\mathrm{I}} z}) \, |\mathbf{n}, \tau\rangle, \\
\mathbf{E}_{\parallel}^{\mathrm{II}} &= \sum_{\mathbf{n},\tau} t_{\mathbf{n},\tau} e^{ik_z^{\mathbf{n},\mathrm{II}} z} \, |\mathbf{n}, \tau\rangle, \\
-\hat{z} \times \mathbf{H}_{\parallel}^{\mathrm{I}} &= \sum_{\mathbf{n},\tau} Y_{\mathbf{n},\tau}^{\mathrm{I}} (i_{\mathbf{n},\tau} e^{ik_z^{\mathbf{n},\mathrm{I}} z} - r_{\mathbf{n},\tau} e^{-ik_z^{\mathbf{n},\mathrm{I}} z}) \, |\mathbf{n}, \tau\rangle, \qquad (3.1) \\
-\hat{z} \times \mathbf{H}_{\parallel}^{\mathrm{II}} &= \sum_{\mathbf{n},\tau} Y_{\mathbf{n},\tau}^{\mathrm{II}} t_{\mathbf{n},\tau} e^{ik_z^{\mathbf{n},\mathrm{II}} z} \, |\mathbf{n}, \tau\rangle,
\end{aligned}$$

where $|\mathbf{n}, \tau\rangle = |n_x, n_y, \tau\rangle$ represents the in-plane (tangential) electric field of the $\mathbf{n}$-th diffracted plane wave with an in-plane wave-number $\mathbf{k}_{\parallel}^{\mathbf{n}} = (k_x^{\mathbf{n}}, k_y^{\mathbf{n}})$, a polarization state τ (s or p polarization) and a wave admittance in the superstrate (substrate) $Y_{\mathbf{n},\tau}^{\mathrm{I}}$ ($Y_{\mathbf{n},\tau}^{\mathrm{II}}$). The wave admittance of an s-polarized plane wave is $Y_{\mathbf{n},s} = k_z^{\mathbf{n}}/(Z_0 k_0)$ and that of a p-polarized plane wave is $Y_{\mathbf{n},p} = \epsilon_r k_0/(Z_0 k_z^{\mathbf{n}})$. In the above expressions, $k_x^{\mathbf{n}} = 2\pi n_x/P_x$, $k_y^{\mathbf{n}} = 2\pi n_y/P_y$, and $k_z^{\mathbf{n}} = \sqrt{\epsilon_r k_0^2 - (k_{\parallel}^{\mathbf{n}})^2}$ are respectively the x, y, and z components of the wavevector $\mathbf{k}^{\mathbf{n}}$. k_0 is the wavenumber of the wave in vacuum and ϵ_r is the relative permittivity of the medium in which the wave is propagating. $Z_0 \approx 376.73\ \Omega$ is the impedance of vacuum. The spatial representation of $|\mathbf{n}, \tau\rangle$ is given by:

$$\langle \mathbf{r}_{\parallel} | \mathbf{n}, s \rangle = \frac{\exp(ik_x^{\mathbf{n}} x + ik_y^{\mathbf{n}} y)}{k_{\parallel}^{\mathbf{n}} \sqrt{P_x P_y}} \{k_y^{\mathbf{n}} \hat{x} - k_x^{\mathbf{n}} \hat{y}\}, \qquad (3.2)$$

$$\langle \mathbf{r}_{\parallel} | \mathbf{n}, p \rangle = \frac{\exp(ik_x^{\mathbf{n}} x + ik_y^{\mathbf{n}} y)}{k_{\parallel}^{\mathbf{n}} \sqrt{P_x P_y}} \{k_x^{\mathbf{n}} \hat{x} + k_y^{\mathbf{n}} \hat{y}\}. \qquad (3.3)$$

The surface current in the plasmonic antennas is expanded with the use of the basis functions $|\mathbf{j}_{\alpha}^{m}\rangle$ satisfying the boundary condition of vanishing current on the antenna edges. The electric current in the m-th antenna within the unit cell takes the form

$$\mathbf{J}^m = \sum_\alpha c_\alpha^m \left|\mathbf{j}_\alpha^m\right\rangle \tag{3.4}$$

where c_α^m is the amplitude of the α-th current mode. The precise form of the functions $\left|\mathbf{j}_\alpha^m\right\rangle$ depends on the antenna geometry, which will be taken rectangular throughout the chapter. For this case, the explicit expressions for $\left|\mathbf{j}_\alpha^m\right\rangle$ are given elsewhere. [26]

The finite conductivity of the antennas is incorporated into the model using the relation

$$\mathbf{J}^m = \sigma \mathbf{E}_\parallel^m \tag{3.5}$$

where $\sigma = ih\epsilon_m k_0$ is the effective surface conductivity of the antennas of thickness h and permittivity ϵ_m [104]. The fields in the substrate and the superstrate should satisfy the standard continuity boundary condition over the interface between them

$$\mathbf{E}_\parallel^{\mathrm{I}} = \mathbf{E}_\parallel^{\mathrm{II}}, \tag{3.6a}$$

$$-\hat{z} \times \mathbf{H}_\parallel^{\mathrm{I}} = -\hat{z} \times \mathbf{H}_\parallel^{\mathrm{II}}. \tag{3.6b}$$

Over the antennas, the electric field is continuous and Eq. (3.6a) still holds, however a discontinuity in the magnetic field appears due to the finite current in the antennas

$$-\hat{z} \times \left(\mathbf{H}_\parallel^{\mathrm{I}} - \mathbf{H}_\parallel^{\mathrm{II}}\right) = \mathbf{J}. \tag{3.6c}$$

Combining these constraints together with the modal expansions and using the orthonormality of the basis functions, we obtain a system of three linear equations:

$$i_{\mathbf{n},\tau} + r_{\mathbf{n},\tau} = t_{\mathbf{n},\tau}, \tag{3.7a}$$

$$Y^{\mathrm{I}}_{\mathbf{n},\tau}(i_{\mathbf{n},\tau} - r_{\mathbf{n},\tau}) - Y^{\mathrm{II}}_{\mathbf{n},\tau} t_{\mathbf{n},\tau} = \sum_{\alpha,m} \langle \mathbf{n}, \tau | \mathbf{j}^m_\alpha \rangle \, c^m_\alpha, \tag{3.7b}$$

$$\sum_{\mathbf{n},\tau} \langle \mathbf{j}^m_\alpha | \mathbf{n}, \tau \rangle \, (i_{\mathbf{n},\tau} + r_{\mathbf{n},\tau}) = \sigma^{-1} c^m_\alpha. \tag{3.7c}$$

Eqs. (3.7a-3.7b) are obtained by multiplying Eqs. (3.6a-c) (from left) by $\langle \mathbf{n}, \tau|$ and Eq. (3.7c) is obtained by multiplying Eq. (3.5) (from left) by $\langle \mathbf{j}^m_\alpha|$. The scalar product $\langle \mathbf{n}, \tau | \mathbf{j} \rangle$ is defined as

$$\langle \mathbf{n}, s | \mathbf{j} \rangle = \int_{-a_x/2}^{a_x/2} \int_{-a_y/2}^{a_y/2} \frac{\exp\left(-ik^{\mathbf{n}}_x x - ik^{\mathbf{n}}_y y\right)}{k^n_\parallel \sqrt{P_x P_y}} \times \{k^{\mathbf{n}}_y j_x(x,y) - k^{\mathbf{n}}_x j_y(x,y)\} dx\, dy, \tag{3.8}$$

$$\langle \mathbf{n}, p | \mathbf{j} \rangle = \int_{-a_x/2}^{a_x/2} \int_{-a_y/2}^{a_y/2} \frac{\exp\left(-ik^{\mathbf{n}}_x x - ik^{\mathbf{n}}_y y\right)}{k^n_\parallel \sqrt{P_x P_y}} \times \{k^{\mathbf{n}}_x j_x(x,y) + k^{\mathbf{n}}_y j_y(x,y)\} dx\, dy. \tag{3.9}$$

where $j_x(x,y)$ and $j_y(x,y)$ are the x and y components of the current profile $|\mathbf{j}\rangle$. Eqs. (3.7a-3.7c) can be solved to obtain the amplitude of the scattered fields $t_{\mathbf{n},\tau}$ and $r_{\mathbf{n},\tau}$ in terms of the antenna current modes c^m_α

$$t_{\mathbf{n},\tau} = \frac{2Y^{\mathrm{I}}_{\mathbf{n},\tau}}{Y^{\mathrm{I}}_{\mathbf{n},\tau} + Y^{\mathrm{II}}_{\mathbf{n},\tau}} i_{\mathbf{n},\tau} - \frac{\sum_{\alpha,m} \langle \mathbf{n}, \tau | \mathbf{j}^m_\alpha \rangle \, c^m_\alpha}{Y^{\mathrm{I}}_{\mathbf{n},\tau} + Y^{\mathrm{II}}_{\mathbf{n},\tau}}, \tag{3.10}$$

$$r_{\mathbf{n},\tau} = \frac{Y^{\mathrm{I}}_{\mathbf{n},\tau} - Y^{\mathrm{II}}_{\mathbf{n},\tau}}{Y^{\mathrm{I}}_{\mathbf{n},\tau} + Y^{\mathrm{II}}_{\mathbf{n},\tau}} i_{\mathbf{n},\tau} - \frac{\sum_{\alpha,m} \langle \mathbf{n}, \tau | \mathbf{j}^m_\alpha \rangle \, c^m_\alpha}{Y^{\mathrm{I}}_{\mathbf{n},\tau} + Y^{\mathrm{II}}_{\mathbf{n},\tau}}, \tag{3.11}$$

where the amplitude of the α-th current mode in the m-th antenna c_α^m is

$$\sum_{\alpha\prime,m\prime}\{\sigma^{-1}\delta_{\alpha,\alpha\prime}\delta_{m,m\prime} + S_{\alpha\ \alpha\prime}^{mm\prime}\}c_{\alpha\prime}^{m\prime} = \chi_\alpha^m \tag{3.12}$$

In Eq. (3.12), $S_{\alpha\ \alpha\prime}^{mm\prime}$ is the Green's function that describes the cross-talk between the α-th current mode of the m-th antenna with the $\alpha\prime$-th current mode of the $m\prime$-th antenna in the unit cell. This coupling is mediated by the plane waves of all (propagating and evanescent) diffraction orders $\mathbf{n}$ as given by Eq. (3.13a). χ_α^m is the direct coupling strength of the α-th current mode of the m-th antenna to the external field.

$$S_{\alpha\ \alpha\prime}^{mm\prime} = \sum_{\mathbf{n},\tau}\frac{\langle\mathbf{j}_\alpha^m|\mathbf{n},\tau\rangle\langle\mathbf{n},\tau|\mathbf{j}_{\alpha\prime}^{m\prime}\rangle}{Y_{\mathbf{n},\tau}^{\mathrm{I}} + Y_{\mathbf{n},\tau}^{\mathrm{II}}} \tag{3.13a}$$

$$\chi_\alpha^m = \sum_{\mathbf{n},\tau}\frac{2Y_{\mathbf{n},\tau}^{\mathrm{I}}\langle\mathbf{j}_\alpha^m|\mathbf{n},\tau\rangle}{Y_{\mathbf{n},\tau}^{\mathrm{I}} + Y_{\mathbf{n},\tau}^{\mathrm{II}}}i_{\mathbf{n},\tau}. \tag{3.13b}$$

In addition to the scattering characteristics, the eigenmodes of the structure can also be determined by solving the secular equation

$$\det\{\sigma^{-1}\delta_{\alpha,\alpha\prime}\delta_{m,m\prime} + S_{\alpha\ \alpha\prime}^{mm\prime}\} = 0. \tag{3.14}$$

In general, Eq. (3.14) can be satisfied only at complex frequencies $\omega = \omega_r + i\omega_i$, showing that the eigenmodes have a finite lifetime due to either Ohmic losses (when $\mathrm{Re}\{\sigma\} \neq 0$) or radiative decay[55, 77]. A real eigenvalue ω may be ideally achieved only in the limit of lossless meta-surfaces and for $k_\parallel > k$, which ensures absence of absorption and radiation. While in this chapter we assume a two-dimensional periodic array of the antennas, but the results can be generalized to the case of an individual antenna. In that case, the sum over the discrete set of plane waves $\sum_{\mathbf{n}}$ in the above expressions, should be replaced by an integral over the continuum $\int\int dk_x dk_y$.[40]

3.3 Collective response of Single-Antenna Metasurfaces

While Eqs. (3.10-3.12) fully characterize the optical properties of the system, they have to be solved numerically. However, in the case when the wavelength of the incident light matches the resonant wavelength of a particular current eigenmode $|\mathbf{j}_{\alpha}^{m}\rangle$, truncation of the current modes' basis can provide simple and instructive expressions [73]. Indeed, it has been shown for the case of perforated metal films that near the cut-off frequency of a particular waveguide mode such a "minimal" model can provide a very good approximation [39, 49]. As will be shown later this situation holds for the antenna geometries in the frequency range studied here. It is worthwhile mentioning here, however, that as dimensions of antennas decrease and they become increasingly subwavelength, the convergence of the MMT deteriorates and more and more current modes should be considered.

By limiting the current basis to one mode per antenna $|\mathbf{j}_1^{m}\rangle = \sqrt{\frac{2}{a_y}}\cos(\frac{\pi y}{a_y})\,\hat{y}$ we assume a dominant role for the fundamental (electric dipolar) antenna-mode. Such a truncation allows us to get simple analytical expressions for the transmission and reflection amplitudes which qualitatively explain the system's response yet quantitatively match the numerical results.

First we consider a structure with a single antenna per unit cell with large length-to-width aspect ratio so that the fundamental current mode $|\mathbf{j}\rangle \equiv$

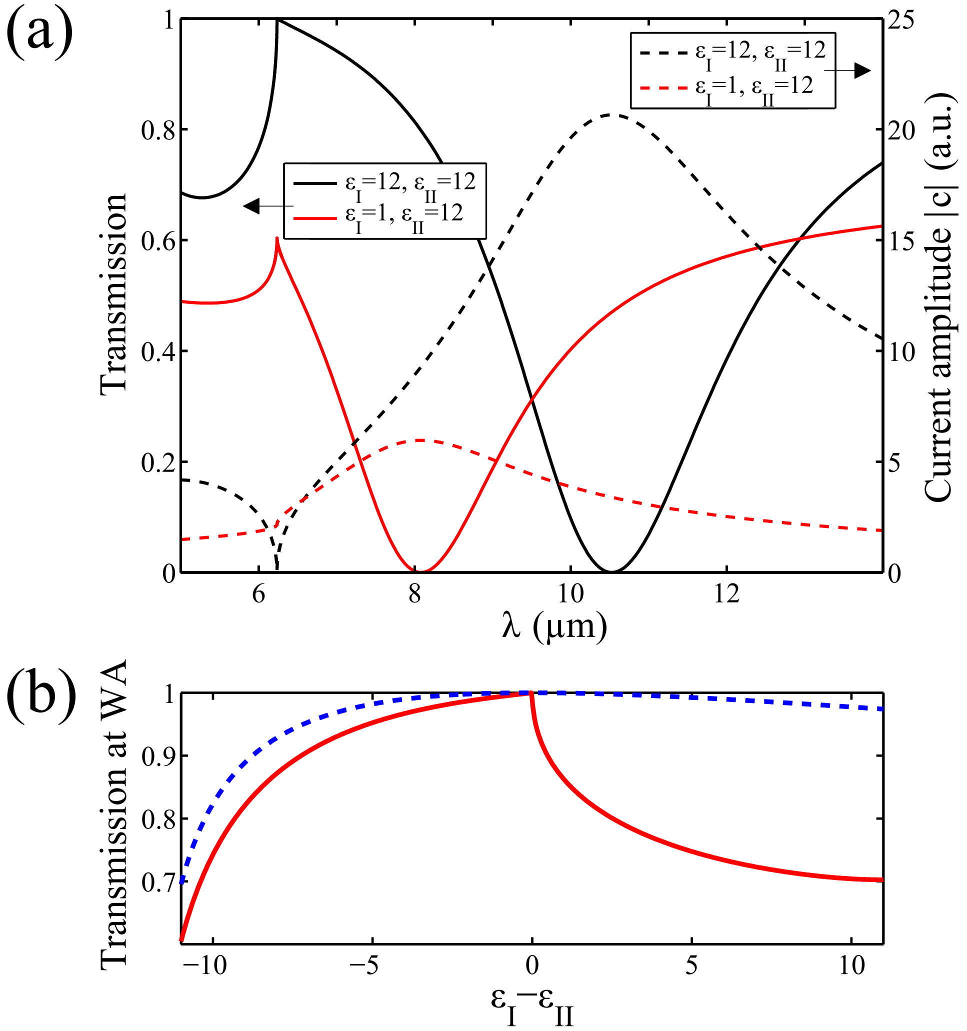

Figure 3.2: (Color online.) (a) Zeroth-order normal-incidence transmission (solid lines) and amplitudes of the fundamental current mode (dashed lines) for the single-antenna metasurface for the symmetric ($\epsilon_{\mathrm{I}} = \epsilon_{\mathrm{II}}$, black lines) and asymmetric ($\epsilon_{\mathrm{I}} \neq \epsilon_{\mathrm{II}}$, red lines) claddings. (b) Zeroth-order transmission of the single-antenna metasurface at the Wood's anomaly as a function of the dielectric contrast $\epsilon_{\mathrm{I}} - \epsilon_{\mathrm{II}}$(solid line) and the bare (without antennas) interface transmission (dashed line). The structure parameters are as follows: $a_x = 0.3\ \mu m$, $a_y = 1.5\ \mu m$, $P_x = 1.8\ \mu m$, $P_y = 1.8\ \mu m$, and $\epsilon_{\mathrm{II}} = 12$.

$\left|\mathbf{j}_1^1\right\rangle$ with the current along the long antenna dimension dominates. In this case Eq. (3.12) can be analytically solved for the current amplitude

$$c(\mathbf{k}_\parallel,\omega) \equiv c_1^1(\mathbf{k}_\parallel,\omega) = \frac{\chi_1(\mathbf{k}_\parallel,\omega)\, E_{\text{ext}}}{\sigma^{-1}(\omega) + S_{11}(\mathbf{k}_\parallel,\omega)}, \tag{3.15}$$

where $\chi_1(\mathbf{k}_\parallel,\omega) = 2Y^{\text{I}}_{\mathbf{0},\tau}/(Y^{\text{I}}_{\mathbf{0},\tau} + Y^{\text{II}}_{\mathbf{0},\tau})\,\langle \mathbf{j}|\mathbf{0},\tau\rangle$ is the coupling efficiency of the antenna to the external field, the sum $S_{11}(\mathbf{k}_\parallel,\omega) \equiv S^{11}_{11}(\mathbf{k}_\parallel,\omega)$ as defined in Eq. (3.13a), $E_{\text{ext}} = i_{\mathbf{0},\tau}$ and the rest of the $i_{\mathbf{n},\tau}$'s are assumed to be zero. In section III and IV we assume that the incident polarization is along the long dimension of the antennas. In the minimal model, S_{11} is explicitly given by:

$$S_{11} = \frac{4Z_0 a_x^2 a_y}{\pi^2 P_x P_y} \sum_{\mathbf{n}} \frac{\operatorname{sinc}^2(a_x k_x^{\mathbf{n}}/2)(1+\cos(a_y k_y^{\mathbf{n}}))}{(1-(a_y k_y^{\mathbf{n}}/\pi)^2)^2} \times \left[\frac{k_0 \left(k_x^{\mathbf{n}}/k_\parallel^{\mathbf{n}}\right)^2}{k_z^{\mathbf{n},\text{I}} + k_z^{\mathbf{n},\text{II}}} + \frac{\left(k_y^{\mathbf{n}}/k_\parallel^{\mathbf{n}}\right)^2}{\epsilon_{\text{I}} k0/k_z^{\mathbf{n},\text{I}} + \epsilon_{\text{II}} k0/k_z^{\mathbf{n},\text{II}}} \right], \tag{3.16}$$

where the first term in the square bracket corresponds to the s-polarized diffraction orders and the second term corresponds to the p-polarized diffraction orders. $\operatorname{sinc}(t) \equiv \sin(t)/t$ can be approximated by unity for thin antennas ($t = k_x a_x/2 \approx 0$). We emphasize that this sum converges much faster compared to that in the dipole model. In the framework of the minimal model the transmission and reflection coefficients of the single-antenna meta-surface assume a simple form:

$$t_{\mathbf{n},\tau} = \frac{2Y^{\text{I}}_{\mathbf{n},\tau}}{Y^{\text{I}}_{\mathbf{n},\tau} + Y^{\text{II}}_{\mathbf{n},\tau}} i_{\mathbf{n},\tau} - \frac{\langle \mathbf{n},\tau|\mathbf{j}\rangle}{Y^{\text{I}}_{\mathbf{n},\tau} + Y^{\text{II}}_{\mathbf{n},\tau}} c, \tag{3.17}$$

$$r_{\mathbf{n},\tau} = \frac{Y^{\text{I}}_{\mathbf{n},\tau} - Y^{\text{II}}_{\mathbf{n},\tau}}{Y^{\text{I}}_{\mathbf{n},\tau} + Y^{\text{II}}_{\mathbf{n},\tau}} i_{\mathbf{n},\tau} - \frac{\langle \mathbf{n},\tau|\mathbf{j}\rangle}{Y^{\text{I}}_{\mathbf{n},\tau} + Y^{\text{II}}_{\mathbf{n},\tau}} c. \tag{3.18}$$

Eqs. (3.17, 3.18) explicitly show two scattering pathways: (i) the direct transmission (reflection) through the dielectric interface between the substrate and the superstrate without interacting with the antennas and (ii) the field radiated by the antennas due to the excitation of the current mode. These two scattering pathways and the presence of the Wood's anomaly [93, 112] lead to a Fano interference resulting in an asymmetric lineshape typically observed in antenna arrays (Fig. 3.2a) and systems with extraordinary optical transmission. The condition of the vanishing denominator in the Eq. (3.15), $\sigma^{-1}(\omega) + S_{11}(\mathbf{k}_{\|}, \omega) = 0$, approximately describes the eigenmodes dispersion of the antenna array (*cf.* Eq. (3.14) for the exact expression).

Note that Eq. (3.15) strongly resembles that of the effective polarizability of an array of dipoles in the dipole model [38]. In our case, $\text{Im}\{1/\sigma(\omega)\}$ plays the role of "plasmonic polarizability" of the antennas while the role of $S_{11}(\mathbf{k}_{\|}, \omega)$ is similar to that of the dipole lattice sum. Note that because the modal-matching technique is based on current expansion, the polarizability and the lattice sum have $\pi/2$ phase shift as compared to the dipole model. It can be shown that when the dipole sum of the dipole model is written in the reciprocal space, the sums of both models have similar terms diverging at the Wood's anomalies. However, in contrast to the dipole model, the antenna model fully considers the substrate, antenna shape and finite conductivity. Here we limit our consideration to the mid-IR domain where antennas can be considered as perfectly conducting ($1/\sigma$=0). Effect of the finite conductivity of the antennas on Fano resonances will be considered elsewhere.

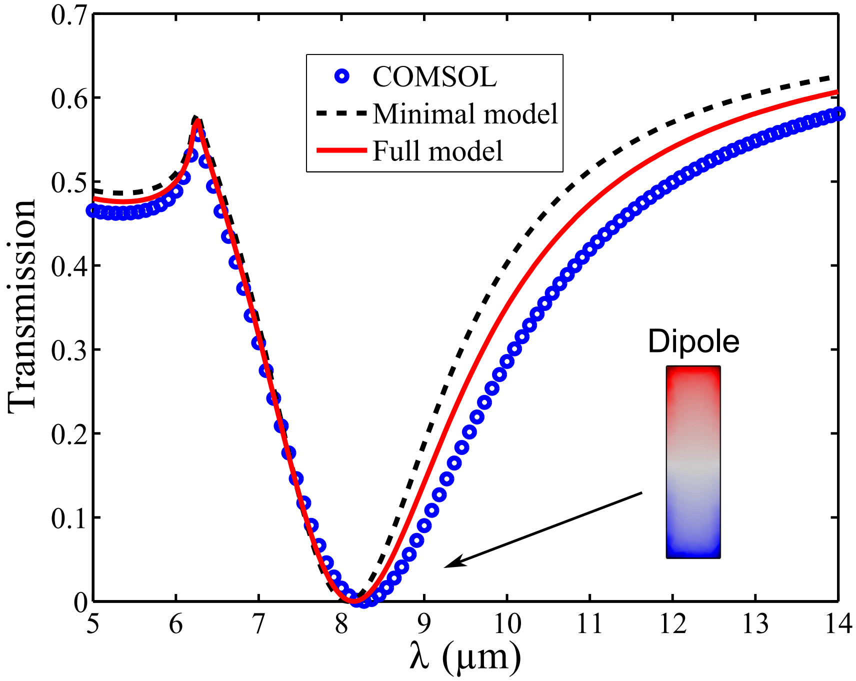

Figure 3.3: (Color online.) Direct transmission at normal incidence calculated using three methods: (i) first-principles COMSOL simulations (circles), (ii) full MMT model (solid line), and (iii) the minimal MMT model (dashed line). Structure parameters: same as in Fig. 3.2.

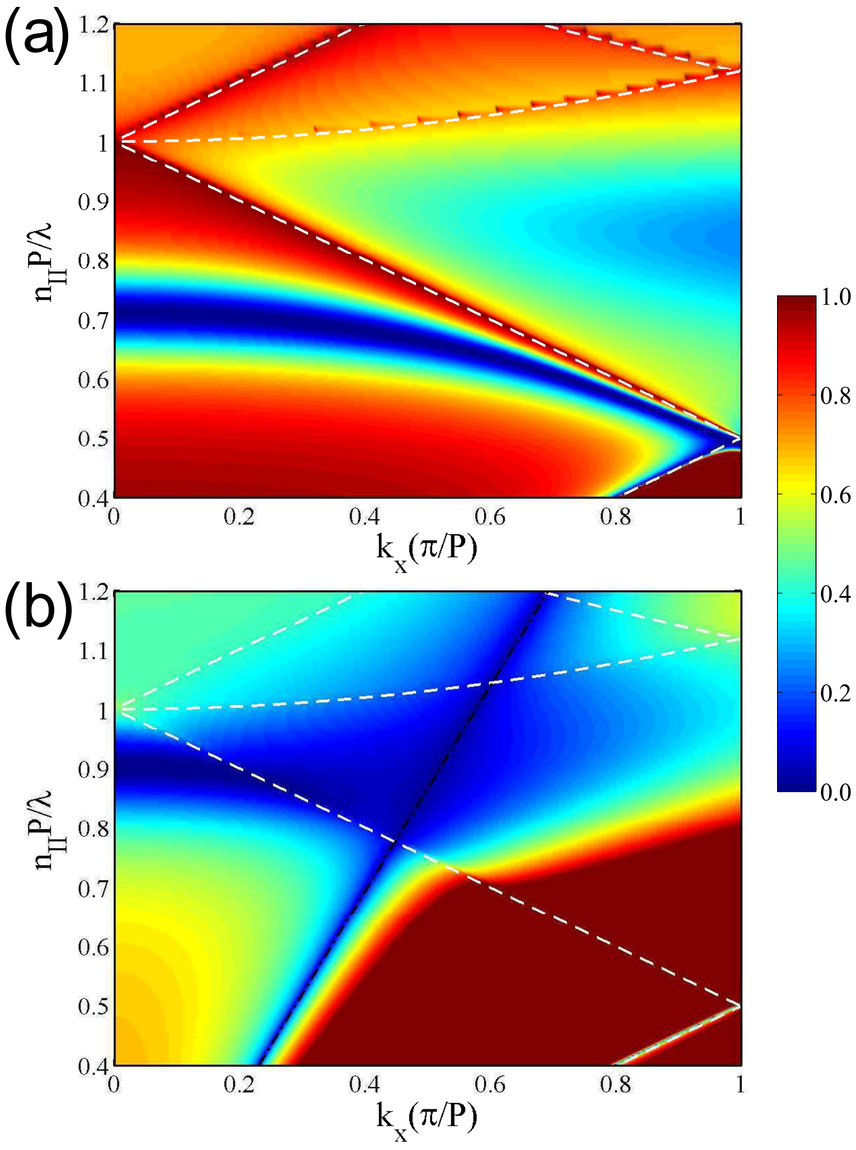

Figure 3.4: (Color online.) Angular-resolved zeroth-order (direct) transmission through the single-antenna metasurface in (a) symmetric ($\epsilon_{\rm I} = \epsilon_{\rm II}$) and (b) asymmetric ($\epsilon_{\rm I} = 1, \epsilon_{\rm II} = 12$) cladding. The parameters of the structure are the same as in Figs. 3.2 and 3.3.

Figure 3.3 compares the results obtained with the use of the analytical minimal model, the full MMT with a sufficient number of current modes (such that the convergence is reached), and the full-wave COMSOL Multiphysics simulations. The minimal model shows very good agreement with both COMSOL and the full model. The inclusion of the higher-order modes only insignificantly changes the spectra. Some discrepancy between the full MMT and COMSOL is attributed to the rounding of the antenna corners that was done in COMSOL to minimize the numerical error due to spurious singularities at sharp corners.

3.3.1 Substrate effects on Wood's anomalies

The substrate effect appears due to the finite dielectric contrast $\Delta\epsilon = \epsilon_{\mathrm{I}} - \epsilon_{\mathrm{II}}$ between the superstrate and substrate claddings, and in the MMT it is described by the wave admittances ($Y_{\mathbf{n},\tau}$) entering the expression for the sum S_{11} [Eq. (3.13a)]. Predictions of the minimal model and the exact calculations clearly show that the presence of a substrate strongly affects the scattering characteristics of the antenna array (Fig. 3.2). This effect can be fully understood from the analytical expressions of the minimal model. Let's first consider the case of a Wood's anomaly that indicates the onset of a diffraction order and appears in the transmission spectrum as a maximum (for symmetric cladding, $\epsilon_{\mathrm{I}} = \epsilon_{\mathrm{II}}$) or as a kink (in the general case) and represents the sharpest feature of the spectrum. Finite optical contrast between the substrate and the superstrate makes the sum S_{11} converge at the onset of the s-polarized diffraction orders which manifests as the suppression of the Wood's anomalies.

Indeed, as can be seen from the expression for $S_{11}(k_{\|}, \omega)$, in the case of a symmetric cladding ($\epsilon_{\mathrm{I}}{=}\epsilon_{\mathrm{II}}$) there is a divergent term corresponding to the onset of a s-polarized diffraction order $|\mathbf{n}, s\rangle$; when the diffraction order experiences a transition between the evanescent and propagating regimes $Y_{\mathbf{n},s} \sim k_z^{\mathbf{n}}$ vanishes and the lattice sum $S_{11}(k_{\|}, \omega)$ diverges as $1/k_z^{\mathbf{n}}$. This gives rise to the Wood's anomaly and vanishing of the current mode in the antennas $c(k_{\|}, \omega) \to 0$, as illustrated by black dashed curve in Fig. 3.2a. Thus, at the Wood's anomaly, antennas are inactive and invisible ($t_{\mathbf{0},\tau} = 1$ and $r_{\mathbf{0},\tau} = 0$) as can be seen from Eqs. (3.17-3.18).

In the case of an asymmetric cladding, $\epsilon_{\mathrm{I}} \neq \epsilon_{\mathrm{II}}$, the same term of the lattice sum that was divergent for the symmetric case, assumes the form $1/(k_z^{\mathbf{n},\mathrm{I}} + k_z^{\mathbf{n},\mathrm{II}})$ and, since $k_z^{\mathbf{n},\mathrm{I}} \neq k_z^{\mathbf{n},\mathrm{II}}$, the lattice sum $S_{11}(k_{\|}, \omega)$ never diverges. As shown in Fig. 3.2a by red dashed curve, even at the Wood's anomaly, the current in the wires $c(\mathbf{k}_{\|}, \omega_{WA})$, does not vanish and the antenna array scatters the radiation.

The fact that antennas remain polarized and contribute to scattering at the Wood's anomaly for any finite value of the optical contrast $\Delta\epsilon$ is illustrated by Fig. 3.2b, where the transmission at the wavelength corresponding to Wood's anomaly of the antenna array on the substrate (solid line) is plotted along with that of the bare (i.e., no antennas) interface (dashed line). The two curves intersect only for the case of a symmetric cladding and the discrepancy can be significant for a large contrast. Thus, the peak transmission of the an-

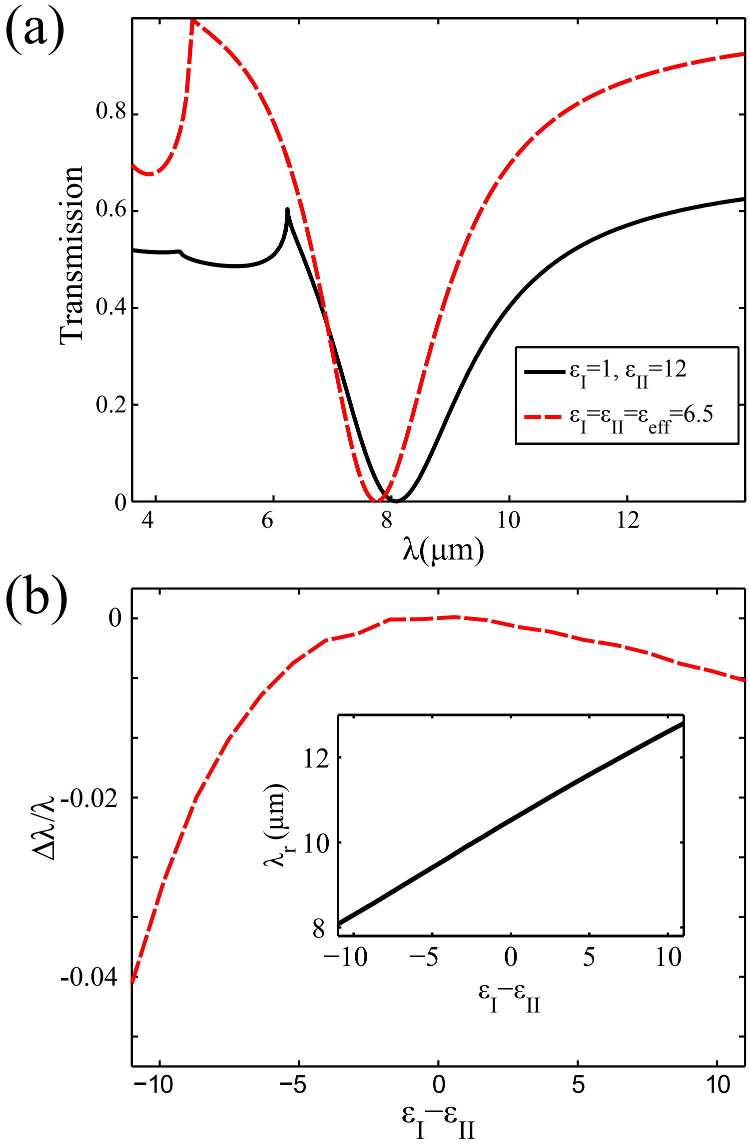

Figure 3.5: (Color online.) (a) Comparison between the exact treatment of the substrate and the result of the homogenized antenna's environment according to the effective medium theory (dashed line). (b) Deviation of the resonance spectral position ($\Delta\lambda/\lambda_r$) predicted by the effective medium approach from the exact result λ_r shown in the inset.

tenna array on the substrate never reaches that of the bare interface. It is also remarkable that the transmission of the antenna array appears very asymmetric with respect to the sign of the contrast and the difference can reach tens of percent. This asymmetry is caused by the presence of the Wood's anomaly of the second medium whose diffraction order dominates in the regime of $\epsilon_{\mathrm{I}} > \epsilon_{\mathrm{II}}$.

3.3.2 Substrate's influence on collective antenna resonances

The spectral position of the collective electric dipolar antenna resonance corresponds to the minimum of the transmission or the maximum of the reflection spectra. It can also be found from the zeros of the imaginary part of the denominator in Eq. 3.15. In this chapter, the length of the antennas are such that the observed collective mode stems from the $\lambda/2$ resonance of an individual antenna (as can be seen from the charge distribution plotted in the inset to Fig. 3.3). As can be seen from dashed curves in Fig. 3.2a, it also corresponds to the maximum of the current amplitude c excited in the antennas. Note that a good agreement between the MMT and COMSOL spectra near the resonance in Fig. 3.3 indicates that our model fully accounts for the modified polarizability of the antennas caused by the presence of the substrate.

The presence of the substrate and suppression of the Wood's anomalies dramatically affect the angular dispersion of the resonance and change its nature. Figure 3.4(a) shows that for the case of a symmetric cladding we observe the effect of "dragging" of the mode by the Wood's anomaly[38, 78], which results in its strong spatial dispersion. This strongly dispersive character of the mode is a manifestation of its collective origin. Indeed, the long-range interaction among the individual metamolecules results in the appearance of the collective modes which are spectrally displaced and sharper as compared to those observed in the individual metamolecules [38, 78]. However, for the case of an asymmetric cladding, shown in the Fig. 3.4b, the dragging effect is diminished and the resonance crosses the Wood's anomalies, every time reducing its quality factor due to the opening of additional radiative channels. The resulting non-dispersive behavior and lower quality factor of the mode imply that the resonance has lost its collective character and represent local excitation modified by the complex electromagnetic environment. Note that for the confined mode of the periodic metasurfaces, i.e. non-leaky spoof plasmons, presence of the substrate and associated suppression of the collective behavior may result in the disappearance of the mode [16].

By following the resonant frequency corresponding to the minimum of the transmission spectrum (Fig. 3.5a) one can also track its spectral position as a function of the dielectric contrast $\Delta\epsilon$. Inset to Fig. 3.5b shows the corresponding spectral shift of the resonance. The frequency of the resonance shows nearly linear dependence on the contrast. We emphasize that the effect of the substrate on the antenna polarizability cannot be rigorously described by a basic dipole model, but can be phenomenologically incorporated into it. One of the most common approaches to include the optical contrast is to use an effective medium approach[81] and approximate the permittivity of the background medium by some uniform effective ϵ_{eff}. For example, for layered media homogenization involves averaging permittivities or their inverse [75, 117]. Note that the choice of homogenization procedure largely depends on the polarization of the waves. In the present work, our main interest is in s polarization because the interaction among electric dipoles in far field has a transverse character and therefore, in periodic structures, the interaction is mediated by s polarized diffraction waves. It is this polarization that experiences Wood's anomalies, gives rise to collective resonances, and perceives average permittivity $\epsilon_{eff} = (\epsilon_{\mathrm{I}} + \epsilon_{\mathrm{II}})/2$. We also limit our consideration to the case of s polarized incidence. The validity of the effective medium approximation can be tested by comparing the spectral position of the resonance calculated for the antennas embedded into the effective medium with the exact MMT result. Figure 3.5b shows the deviation of the resonance frequency as predicted by the effective medium theory from the exact result. One can see that the agreement between the effective medium approach and the exact MMT calculations is rather good. However, it can be seen from Fig. 3.5a that the effective medium approximation fails in predicting the transmission and reflection, especially close to the Wood's anomaly.

3.4 Fano resonance in double-antenna meta-surfaces

Next, the MMT for the double-antenna meta-surface (DAM) shown in Fig. 3.1b is considered. In this case, the truncation of the basis to the fundamental modes in both antennas, results in a minimal model with a 2x2 matrix equation for the amplitudes c_1 and c_2:

$$\begin{bmatrix} S_{11} & S_{12} \\ S_{21} & S_{11} \end{bmatrix} \begin{bmatrix} c_1 \\ c_2 \end{bmatrix} = \chi E_{\text{ext}} \begin{bmatrix} e^{-ik_x D_x/2} \\ e^{+ik_x D_x/2} \end{bmatrix}, \tag{3.19}$$

where $S_{mm\prime} \equiv S_{11}^{mm\prime}$ represents the effective Green's function given by Eq. (3.13a), and $\chi{=}2Y^{\text{I}}_{\mathbf{0},\tau}/(Y^{\text{I}}_{\mathbf{0},\tau}+Y^{\text{II}}_{\mathbf{0},\tau})\exp(ik_xD_x/2)\left\langle \mathbf{j}^{(1)}|\mathbf{0},\tau\right\rangle$ is the coupling strength of the incident light ($|\mathbf{0},\tau\rangle$) to the fundamental current modes.

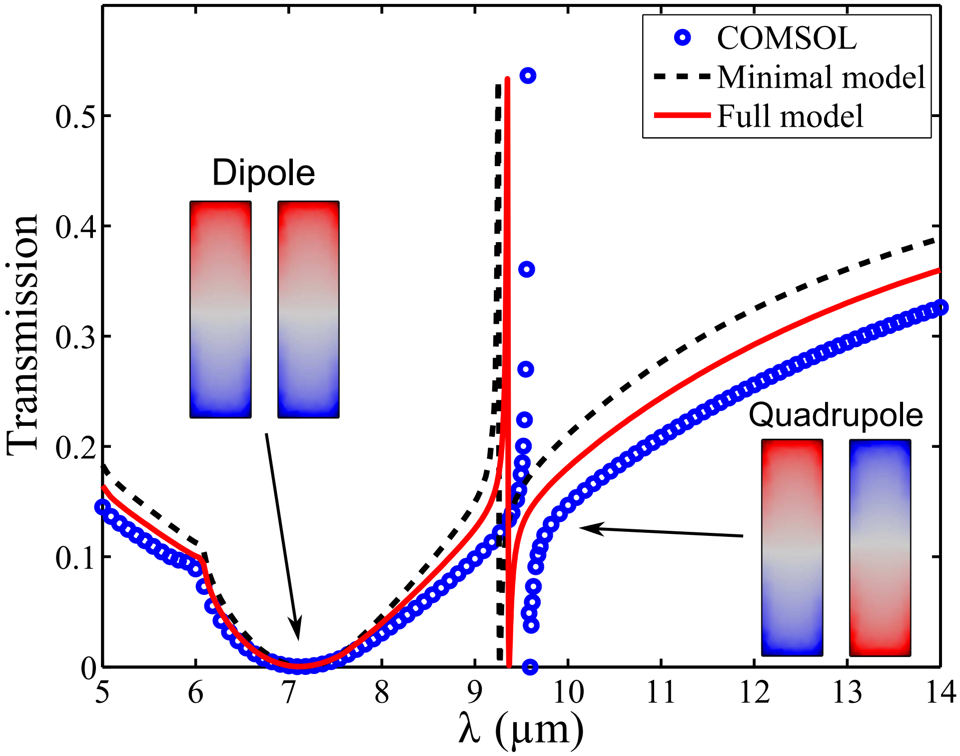

Figure 3.6: (Color online.) Comparison of the zeroth-order transmission spectra of a double-antenna metasurface on the substrate for 50° angle of s-polarized incidence calculated with the use of COMSOL Multiphysics, and the minimal and full MMT models. The structure parameters are as follows: $a_x = 0.3$ μm, $a_y = 1.5$ μm, $P_x = P_y = 1.8$ μm, $D_x = 0.6$ μm, $\epsilon_{\text{I}} = 1$, and $\epsilon_{\text{II}} = 12$.

Using the unitary transformation

$$
\begin{aligned}
c_{\text{sub}} &= c_1 \exp(ik_x D_x/2) - c_2 \exp(-ik_x D_x/2), \\
c_{\text{sup}} &= c_1 \exp(ik_x D_x/2) + c_2 \exp(-ik_x D_x/2),
\end{aligned}
\tag{3.20}
$$

the basis of the two fundamental electric currents can be changed to the more instructive basis of the sub-radiant and super-radiant current modes. In the new basis, the system is described by the matrix equation

$$
\begin{bmatrix} S_{11} + \Delta & i\kappa \\ -i\kappa & S_{11} - \Delta \end{bmatrix} \begin{bmatrix} c_{\text{sup}} \\ c_{\text{sub}} \end{bmatrix} = \chi E_{\text{ext}} \begin{bmatrix} 2 \\ 0 \end{bmatrix}, \tag{3.21}
$$

where $\Delta = -1/2[S_{12} \exp(ik_x D_x) + S_{21} \exp(-ik_x D_x)]$ and $\kappa = i/2[S_{12} \exp(ik_x D_x) - S_{21} \exp(-ik_x D_x)]$. These modes are the result of the radiative coupling of the electric dipole moments of the antenna pairs [68, 78, 114]. The super-radiant and sub-radiant modes have distinct symmetric and anti-symmetric charge distributions, while the currents corresponding to them are collinear and anti-collinear, respectively, as illustrated by the inset to Fig. 3.6. The modes interaction makes them blue-shifted (super-radiant) and red-shifted (sub-radiant) with respect to the electric-dipolar resonance of SAM. Another consequence of such hybridization and different symmetry of the modes is their different radiative coupling efficiency. The sub-radiant mode is not directly coupled to the incident light. The latter fact is reflected in the mode's name and directly follows from the zero radiative coupling strength on the RHS of Eq. (3.21).

With the use of Eqs. (3.10,3.11) we obtain a set of minimal-model

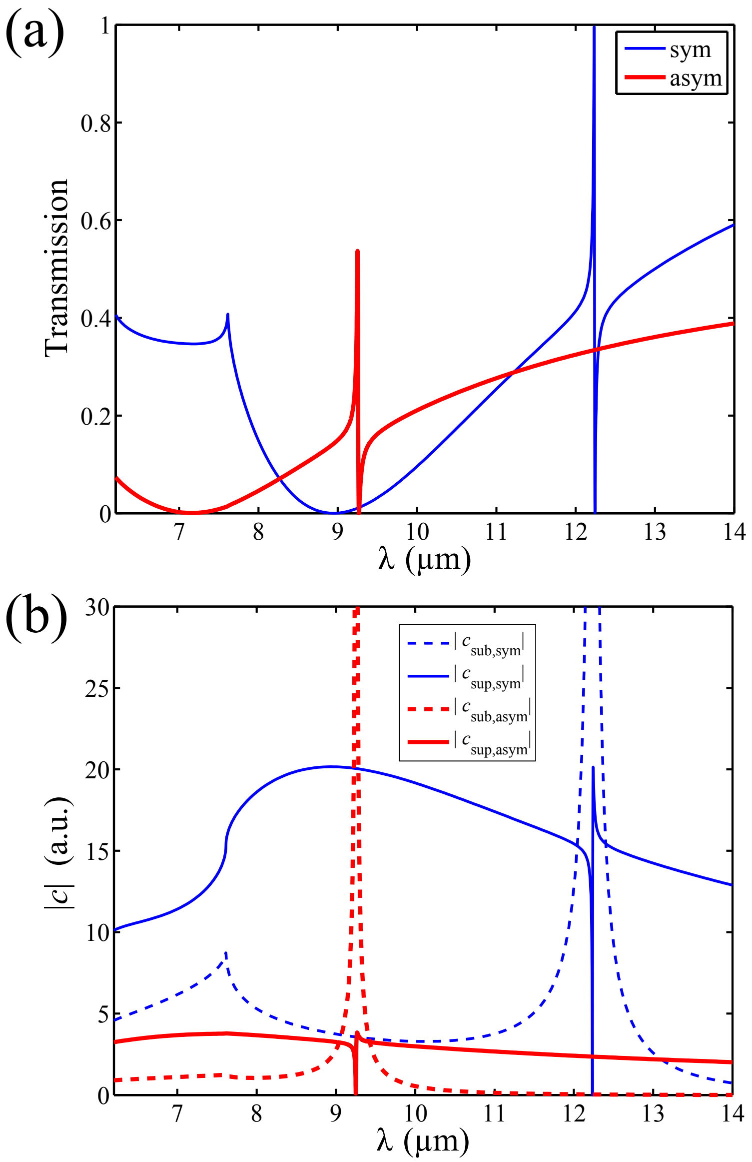

Figure 3.7: (Color online.) (a) Zeroth-order s-polarized transmission spectra of the double-antenna meta-surface for the symmetric ($\epsilon_{\mathrm{I}}=\epsilon_{\mathrm{II}}=12$, blue line) and asymmetric ($\epsilon_{\mathrm{I}}=1$, $\epsilon_{\mathrm{II}}=12$, red line) claddings. (b) Amplitude of the sub-radiant (dashed lines) and super-radiant (solid lines) current modes. The parameters of the structure and the incidence angle are the same as in Fig. 3.6.

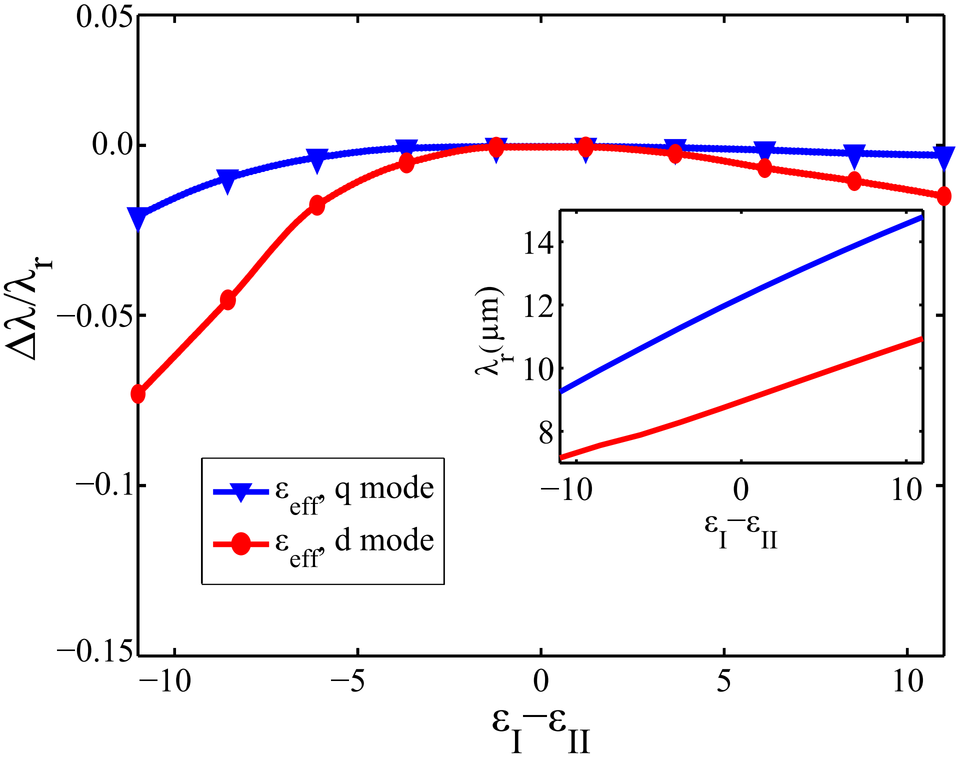

Figure 3.8: (Color online.) Deviation of the spectral position ($\Delta\lambda/\lambda_r$) of the dipolar (red lines with circle markers) and quadrupolar (blue lines with triangle markers) resonances predicted by the effective medium approach from the exact results λ_r shown in the inset.

expressions for the transmission and reflection coefficients:

$$t_{\mathbf{n},\tau} = \frac{2Y^{\mathrm{I}}_{\mathbf{n},\tau}}{Y^{\mathrm{I}}_{\mathbf{n},\tau} + Y^{\mathrm{II}}_{\mathbf{n},\tau}} i_{\mathbf{n},\tau} - \frac{\left\langle \mathbf{n}, \tau \,|\, \mathbf{j}^{(1)} \right\rangle \exp\left(-ik_x D_x/2\right)}{Y^{\mathrm{I}}_{\mathbf{n},\tau} + Y^{\mathrm{II}}_{\mathbf{n},\tau}} c_{\mathrm{sup}}, \tag{3.22}$$

$$r_{\mathbf{n},\tau} = \frac{Y^{\mathrm{I}}_{\mathbf{n},\tau} - Y^{\mathrm{II}}_{\mathbf{n},\tau}}{Y^{\mathrm{I}}_{\mathbf{n},\tau} + Y^{\mathrm{II}}_{\mathbf{n},\tau}} i_{\mathbf{n},\tau} - \frac{\left\langle \mathbf{n}, \tau \,|\, \mathbf{j}^{(1)} \right\rangle \exp\left(-ik_x D_x/2\right)}{Y^{\mathrm{I}}_{\mathbf{n},\tau} + Y^{\mathrm{II}}_{\mathbf{n},\tau}} c_{\mathrm{sup}}. \tag{3.23}$$

Note that because of their coupling, c_{sup} and c_{sub} are not the true eigenmodes of the system. The true eigenmodes which will be referred to as electric dipolar d and electric quadrupolar q, named according to their dominant multipolar moment, can be obtained using the transformation:[78]

$$\begin{aligned} d &= \frac{\Delta + X}{2X} c_{\mathrm{sup}} + \frac{i\kappa}{2X} c_{\mathrm{sub}}, \\ q &= \frac{i\kappa}{2X} c_{\mathrm{sup}} + \frac{\Delta + X}{2X} c_{\mathrm{sub}}, \end{aligned} \tag{3.24}$$

where $X = \sqrt{\Delta^2 + \kappa^2}$. The modal coefficients d and q are related to the incident field through

$$\begin{aligned} d =& \frac{1 + \Delta/X}{S_d} \chi E_{ext}, \quad S_d = S_{11} + X, \\ q =& \frac{i\kappa/X}{S_q} \chi E_{ext}, \quad S_q = S_{11} - X, \end{aligned} \tag{3.25}$$

Henceforth the prefix “electric” will be omitted for these modes. In the particular case of normal incidence, the quadrupolar mode q exactly coincides with the sub-radiant mode c_{sub} since its coupling to the super-radiant mode c_{sup} vanishes ($\kappa \to 0$ as $\mathbf{k}_\parallel \to 0$). However, at finite angles of incidence, this mode acquires a finite electric-dipole moment and its radiative coupling and bandwidth gradually increase. The dipolar mode, in contrast, is always strongly radiatively coupled and is spectrally broad at any incidence angle. Eqs. (3.22-3.23) describe a Fano resonance of a single "continuum" interacting with two "discrete" dipolar (d) and quadrupolar (q) resonances. However, the bandwidth of the last two is very different due to their different radiative coupling.

The transmission spectrum of DAM for an oblique incidence of 50° calculated using the minimal model, full MMT and COMSOL solver are plotted alongside in Fig. 3.6. As before, the different techniques show very good agreement, which implies the applicability of the analytical minimal model even for the description of light scattering by more complex metasurfaces such as DAM. Two resonances, a broad one due to the excitation of the dipolar mode and a narrow one due to the excitation of the quadrupolar mode, are clearly seen in the spectra. As expected, the narrow resonance has a strongly asymmetric shape typical for Fano resonances.

3.4.1 Dipolar mode

Because the dipolar and quadrupolar resonances are spectrally separated and the quadrupolar resonance is spectrally narrow, first we can consider the dipolar resonance individually. It has been recently shown that the collective dipolar resonance in DAM appears to have spatial dispersion $[\omega(\mathbf{k}_{\|})]$ very different from that found in SAM [78]. Using the basic dipole model, this difference was shown to be due to the suppression of the long-range interactions in DAMs. MMT provides analogous results. In the present case, however, the role of the substrate and the antenna geometry are fully taken into account. In DAM, the Wood's anomalies would have corresponded to the divergences (or local maxima for an asymmetric cladding) of the effective Green's function $S_d = S_{11} + X$ playing the role of the lattice sum in the dipole model or the Green's function S_{11} of SAM. However, it can be shown that exactly at the frequency where the Wood's anomaly is expected, the diverging terms in S_{11} and X exactly cancel out eliminating the divergence, thereby suppressing the spectral features associated with the Wood's anomaly [78]. Thus, in the DAM case, Wood's anomaly appears to be suppressed even for a symmetric cladding ($\Delta\epsilon = 0$). Therefore for the asymmetric cladding, the Wood's anomaly is suppressed by two mechanisms: one due to substrate/superstrate contrast just as in the case of SAM, and another one due to disconnected topology of DAM. Note, however, that despite such suppression, one might still observe some variations of reflectivity in the vicinity of the expected Wood's anomalies, which is a result of the opening of the diffraction channel and change of the mode's radiative lifetime. [78].

3.4.2 Quadrupolar mode

Now we focus on the quadrupolar resonance. The narrow spectral region where the transmission undergoes a rapid variation is especially interesting because of the strong field enhancement and slow light regime reported earlier [35, 114]. The asymmetric shape of the spectrum is the result of the Fano interference between the quadrupolar resonance and a background provided by two transmission channels: (i) the direct transmission without interaction with the array, and (ii) the radiation scattered by the dipolar resonance. This background is nearly constant and is featureless over the spectral width of the quadrupolar resonance where the transmission changes from its maximal value to zero. It can be analytically shown that the transmission peak corresponds to the divergence of c_{sub} and zero of c_{sup}(Fig. 3.7b). Because only the super-radiant mode (c_{sup}) is coupled to the radiation, the antennas do not radiate at this frequency and the transmission acquires a universal value of the transmission of the bare interface between the substrate and the superstrate as seen from Eqs. (3.22,3.23). Note that this behavior is different from that found for another type of Fano resonances, Wood's anomalies in SAM, when for an asymmetric cladding configuration, the radiative current mode always had some finite amplitude.

In the previous section, it was demonstrated that the effective medium approach accurately predicted the spectral position of the dipolar resonance for SAM. Here we test this approach for both cases of the dipolar and quadrupolar resonances in DAM. At first, the inset to Fig. 3.8 shows the spectral position of the resonances calculated by the full MMT approach as a function of the dielectric contrast, and Fig. 3.8 shows the deviation from the exact result. The effective medium theory matches well with the exact MMT results for both quadrupolar and dipolar resonances. However, just as in the case of SAM, the homogenization approach does not succeed in predicting the transmission/reflection spectra.

Finally, we observe that in contrast to the dipolar mode, the quadrupolar mode in DAM is strongly affected by the Wood's anomaly. From the expression for its amplitude Eq. (3.25) one can see that for the quadrupolar mode the divergence in the Green's function $S_{11} - X$ does take place in the case of a symmetric cladding $\epsilon_{\mathrm{I}} = \epsilon_{\mathrm{II}}$. The effect of the Wood's anomaly on the quadrupolar resonance of the DAM is expected to be especially significant for large angles of incidence, when they approach each other. This results in a strong spatial dispersion of the quadrupolar mode observed earlier both in mid- and near-IR plasmonic DAMs [78]. For the case of an asymmetric cladding the effect of the Wood's anomaly on the quadrupolar resonance is again suppressed due to the mismatch of the wave admittances in the substrate and the superstrate and all the arguments about the suppression of the Wood's anomalies used in the previous section for SAM are applicable here.

3.5 Electromagnetically Induced Transparency

In this section the effect of substrate on EIT is studied. It is worth mentioning that EIT-like electromagnetic response can be found in early studies on frequency-selective surfaces [22]. Acoustic counterpart of EIT has also been reported recently [48]. Here we consider a periodic dolmen structure with three antennas in its unit cell [118],[86],[68],[108],[114] [shown in Fig. 3.1c] is studied. This design was first introduced to mimic EIT in plasmonic structures for normally incident x-polarized light [118]. Two vertical antennas on the dolmen structure are responsible for formation of the quadrupolar mode analogous to that described in the previous section. This mode plays the role of the sub-radiant mode of EIT. The horizontal antenna provides a spectrally broad electric dipolar resonance. Its length is chosen in such a way that the central frequency of the dipolar resonance is matched to the frequency of the sub-radiant (quadrupolar) mode. The position of the horizontal antenna within the unit cell defines the degree of symmetry breaking of the metamolecule and the intensity of coupling between the two modes. The sub-radiant mode is completely decoupled from x-polarized incident radiation if the antenna is placed equidistantly between the two nearest vertical double antennas, $D_y = 0$. However, as soon as the horizontal antenna is displaced vertically from this position ($D_y \neq 0$), the sub-radiant mode couples to the incident radiation indirectly through the dipolar mode of the horizontal antenna. This coupling to the sub-radiant mode results in a transmission/reflection spectrum typical for the EIT: a sharp transmission resonance embedded into a region of highly reflecting background provided by the dipolar antenna mode. Note that for the polarization under study the dipolar mode of two-vertical antennas is not excited since there is no y-component of the incident electric field. In principle, this mode could be excited indirectly provided that the symmetry of the metamolecule is reduced further by displacing the horizontal antenna in the x-direction [114]. However, this situation will not be considered here.

Within the minimal model, limiting the current basis to only fundamental current mode for each antenna and neglecting finite conductivity of the metallic antennas ($1/\sigma = 0$), the EIT structure can be described by a 3x3 matrix equation relating the current amplitudes to the incident electric field:

$$\begin{bmatrix} S_{11} & S_{12} & S_{13} \\ S_{12} & S_{11} & -S_{13} \\ S_{13} & -S_{13} & S_{33} \end{bmatrix} \begin{bmatrix} c_1 \\ c_2 \\ c_3 \end{bmatrix} = \chi E_{\text{ext}} \begin{bmatrix} 0 \\ 0 \\ 1 \end{bmatrix}, \tag{3.26}$$

where $S_{mm\prime} \equiv S_{11}^{mm\prime}$ represents the effective Green's function given by Eq. (3.13a), and $\chi =< j_3|0 > 2Y^{\text{I}}_{\mathbf{0},\tau}/(Y^{\text{I}}_{\mathbf{0},\tau} + Y^{\text{II}}_{\mathbf{0},\tau})$ is the coupling strength between the incident light and the horizontal antenna (labeled as "3"). The RHS of Eq. (3.26) reflects the fact that the vertical antennas are not coupled to the x-polarized incident light. On the other hand, the presence of off-diagonal matrix elements in the LHS of this equation indicates that they are coupled to the horizontal antenna. It follows from the symmetry of the structure that the basis of three currents is redundant for the case of x-polarized normal incidence, under which the dipolar mode of the antenna pair D_y cannot be excited. By performing the unitary transformation $D_y = c_1 + c_2$, $Q = c_1 - c_2$ and $D_x = c_3$, the non-interacting D_y mode can be eliminated. The truncated governing equation for the super-radiant mode D_x and the sub-radiant mode Q assumes the form:

$$\begin{bmatrix} S_Q & \kappa \\ \kappa & S_{D_x} \end{bmatrix} \begin{bmatrix} Q \\ D_x \end{bmatrix} = \chi E_{\text{ext}} \begin{bmatrix} 0 \\ 1 \end{bmatrix}, \tag{3.27}$$

where $S_Q = 1/2(S_{11} - S_{12})$, $S_{D_x} = S_{33}$, and the coupling between the modes is given by $\kappa = S_{13}$. Note, that unless the horizontal antenna is placed symmetrically (in which case $\kappa = 0$), the modes D_x and Q are not eigenmodes of the EIT structure, since they are coupled to each other through the off-diagonal matrix elements in the LHS of Eq. (3.27). This coupling gives rise to hybridization of the sub-radiant mode Q and the super-radiant mode D_x and formation of new

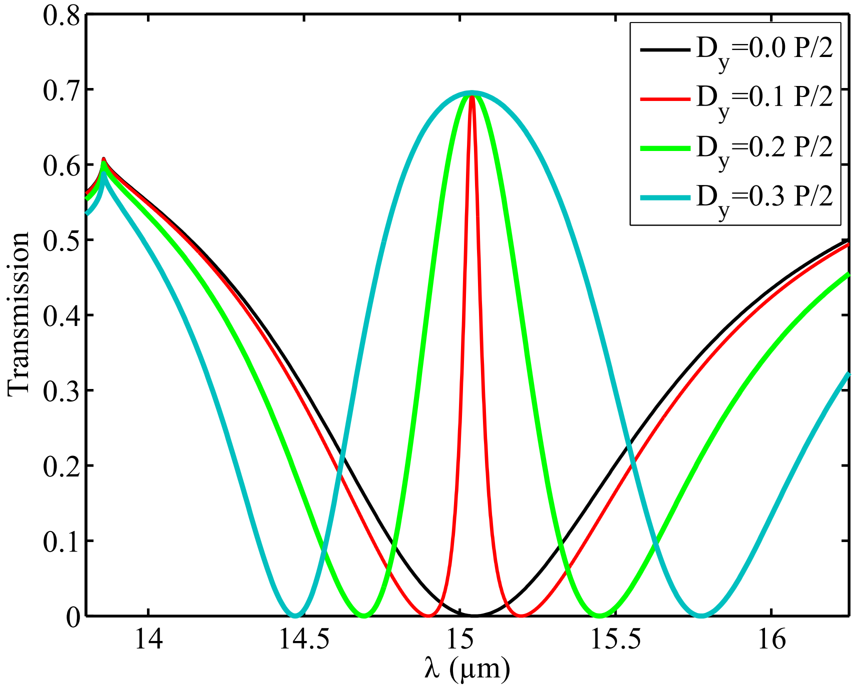

Figure 3.9: (Color online.) Substrate effect on the normal-incidence zeroth-order transmission spectra of the dolmen metasurface for different values of symmetry-breaking parameter D_y. Horizontal antenna's dimensions are $a_x = 1.79\,\mu\text{m}$, $a_y = 0.6\,\mu\text{m}$. Vertical antennas are identical with $a_x = 0.6\,\mu\text{m}$ and $a_y = 1.7\,\mu\text{m}$ and separated by $D_x = 1.2\,\mu\text{m}$. $\epsilon_{\text{I}} = 1$, $\epsilon_{\text{II}} = 12$, and P_x=P_y=$4\,\mu\text{m}$.

mixed states – quasi-dipolar $\tilde{D}_x$ and quasi-quadrupolar $\tilde{Q}$. Both of these modes are coupled to the incident electromagnetic field, but have very disparate coupling efficiency. The true eigenmodes of the structure can be found through an eigen-decomposition procedure, $\tilde{D}_x = 1/(1+\eta^2)\, D_x + \eta/(1+\eta^2)\, Q$ and $\tilde{Q} = 1/(1+\eta^2)\, Q - \eta/(1+\eta^2)\, D_x$ where $\eta = (S_Q - S_{D_x} - \Delta)/2\kappa$ [that tends to zero in the case of a vanishing coupling $\kappa \to 0$] and $\Delta = \sqrt{(S_Q - S_{D_x})^2 + 4\kappa^2}$. Then the equations for the eigenmodes' amplitudes assume the form

$$\tilde{D}_x = \frac{2/(1+\eta^2)}{S_Q + S_{D_x} - \Delta}\,\chi E_{\text{ext}}, \tag{3.28}$$

$$\tilde{Q} = \frac{-2\eta/(1+\eta^2)}{S_Q + S_{D_x} + \Delta}\,\chi E_{\text{ext}}, \tag{3.29}$$

and the reflection/transmission coefficients of the structure can be found from the following equations:

$$r_{\mathbf{n},\tau} = \frac{Y^{\mathrm{I}}_{\mathbf{n},\tau} - Y^{\mathrm{II}}_{\mathbf{n},\tau}}{Y^{\mathrm{I}}_{\mathbf{n},\tau} + Y^{\mathrm{II}}_{\mathbf{n},\tau}} + \frac{\langle \mathbf{n},\tau\,|\,\mathbf{j}_3\rangle}{Y^{\mathrm{I}}_{\mathbf{n},\tau} + Y^{\mathrm{II}}_{\mathbf{n},\tau}}\; D_x, \tag{3.30}$$

$$t_{\mathbf{n},\tau} = \frac{2Y^{\mathrm{I}}_{\mathbf{n},\tau}}{Y^{\mathrm{I}}_{\mathbf{n},\tau} + Y^{\mathrm{II}}_{\mathbf{n},\tau}} + \frac{\langle \mathbf{n},\tau\,|\,\mathbf{j}_3\rangle}{Y^{\mathrm{I}}_{\mathbf{n},\tau} + Y^{\mathrm{II}}_{\mathbf{n},\tau}}\; D_x, \tag{3.31}$$

$$D_x = \tilde{D}_x - \eta\,\tilde{Q}. \tag{3.32}$$

The transmission spectra of the structure are shown in Fig. 3.9. The different curves demonstrate how the radiative coupling of the sub-radiant mode increases when the symmetry of the metamolecule is gradually reduced by increasing the parameter D_y. This manifests, at first, as an appearance of the sharp and narrow EIT transmission peak and a gradual increase of the EIT peak bandwidth. It is remarkable that regardless of the symmetry breaking degree, the maximum of the EIT peak always tends to the same value defined by the transmission of the bare dielectric interface between the substrate and superstrate. Therefore we can claim that this is rather general rule for all Fano resonant systems, where a Fano resonance originates from the structure of the metamolecule and not from Wood's anomaly as in the case of SAM.

3.6 Conclusions

We investigated the effects of a substrate on three different mid-IR Fano metasurfaces and found that a finite refraction-index contrast between the top and bottom claddings dramatically changes the optical response of the structures. In addition to the expected spectral shift of the resonances induced by the substrate, a dramatic change in the collective behavior of the systems was found. The widely used effective medium technique was tested. While satisfactorily predicting the spectral positions of the resonances, it fails to describe other scattering characteristics of the structures. The Wood's anomalies and modes' dispersion were found to be strongly affected by the presence of a substrate. Divergences corresponding to the onset of the *s*-polarized diffraction orders disappear whenever the refractive indices of the substrate and the superstrate are mismatched, resulting in the suppression of the spectral features associated with the Wood's anomalies and giving rise to anomalously flat dispersion of the modes. As the Wood's anomaly and the surface resonances of the periodic metasurfaces can be considered as a Fano resonance due to the collective interaction of metamolecules, it can be concluded that the presence of a substrate destroys the Fano picture. As a consequence, the dramatic effect of the onset of the diffraction orders reduces to the less dramatic change of the modes radiative lifetime. The nature of the modes also changes as they lose their collective character and start resembling local resonances yet modified by their complex environment.

In addition to this collective Fano resonance, we also studied the effect of the substrate on Fano resonances originating from the local geometry of the metamolecules. Two types of Fano systems were considered with a sharp quadrupolar resonance detuned from (double-antenna metasurface) and tuned to (dolmen metasurface) the dipolar resonance providing the Fano background. In both systems the Fano resonances survived after the introduction of the substrate but were affected due to the modification of the frequencies of both low-Q (dipolar) and high-Q (quadrupolar) resonances as well as additional reflection from the substrate. A universal behavior was discovered for both systems: (a) the peak transmission reached the value corresponding to the bare interface, and (b) antennas became effectively invisible at the frequency of the Fano resonance. These findings will be useful for designing non-dispersive photonic devices with a wide-angle optical response.

Chapter 4

Effects Of Topology of Unit Cells On Scattering Properties of Meta-Surfaces

4.1 Introduction

The importance of metamaterials operating in the IR and visible domains for various applications, including plasmonics [15], photovoltaics and thermo-photovoltaics [10], and sensing [2, 65, 69, 116] is hard to underestimate. For this reason, the metamaterials with a resonant response at optical frequencies have recently attracted significant attention. In periodic plasmonic metamaterials, collective effects are known to play an important role, and give rise to such effects as extraordinary optical transmission (EOT) [27, 74], the formation of collective guided modes [11, 107, 110] such as spoof [39, 87] and hybrid spoof surface plasmons [77], and an increased lifetime of resonances [25, 61, 120–122].

The collective behavior in optical metamaterials originates from inherent nonlocal effects. In the case of a periodic assembly of meta-molecules, the major source of non-locality is long-range interaction [5, 11, 38, 110, 121, 122]. Collective long-range effects are most strongly manifested at the onset of Bragg diffraction, when the period is comparable to the wavelength and the cor-

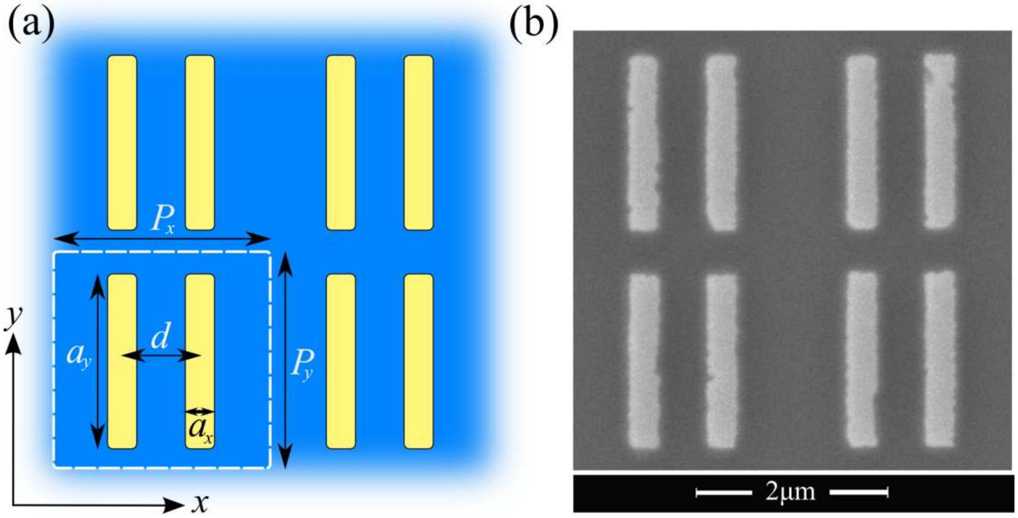

Figure 4.1: (a) Schematics of a double-antenna meta-surface on a substrate. (b) SEM image of the sample grown on CaF_2 ($\epsilon = n^2 = 1.96$). The structure dimensions are $a_y = 1.8\ \mu m$, $a_x = 0.3\ \mu m$, $P = P_x = P_y = 2.25\ \mu m$, and $d = 0.8\ \mu m$.

relation length effectively diverges. In this case, the long-range interaction dominates over the near-field interaction and gives rise to the appearance of Wood's anomalies [112]. Even at longer wavelengths the long-range interaction can significantly affect the optical response of metamaterials. It has long been recognized that both Wood's anomalies and the structure of the unit cell (e.g., its dipole polarizability) strongly influence metamaterial response. For example, the spectral positions of EOT maxima are influenced by the size and shape of the holes in the metal film [38, 39]. The effect of the *topology* of the unit cell, on the other hand, has not received significant attention.

In this chapter, we demonstrate that collective long-range effects can be considerably reduced for unit cells comprised of a pair of disconnected antennas. We theoretically and experimentally study a meta-surface which represents a two-dimensional periodic array of double plasmonic antennas [60]. We focus on the frequency range where the individual antennas experience an electric-dipolar antenna resonance [3, 83]. The double-antenna meta-molecule represents the simplest design experiencing a quadrupolar [68, 114] resonance along with the dipolar resonance, stemming from the single-antenna resonance. When the meta-molecules are arranged to form a periodic array, the collective dipolar and quadrupolar modes emerge from the resonances of the individual meta-molecules. To analyze the collective behavior of this structure, we use a standard dipole model [5, 11, 38, 54, 121, 122]. We show that the dipole model can qualitatively describe the experimentally observed anomalous collective response of the meta-surface. These results are confirmed by a rigorous numerical modal matching technique [26].

In this work, theoretical calculations and numerical modeling were performed by the author and Dr. Alexander B. Khanikaev, angular-resolved FTIR spectroscopy was performed by Burton Neuner III, and nanoscale sample fabrication was performed by David Y. Fozdar.

The chapter is organized as follows: in Section 2 we outline the dipole model of a single-antenna meta-surface (SAM), followed by its extension to the double-antenna meta-surface (DAM). In Section 3 we present the experimental and numerical results and explain the observed behavior applying our analytical model. The results for SAM and DAM are compared and the observed differences are discussed. Finally Section 4 summarizes our results and puts them into perspective with meta-surface applications.

4.2 Optical response of SAM and DAM structures

To understand the physics underlying the optical properties of DAM and demonstrate the importance of the meta-molecule geometry on the collective response, we use as a reference its well-understood counterpart, which consists of periodically arranged single plasmonic antennas. In this chapter, we will focus on the case of s-polarized incidence for which DAM and SAM exhibit a strong discrepancy and DAM experiences a quadrupolar resonance. An s-polarized incidence is defined by the wave-vector of the incident wave in the xz-plane ($k_y = 0$, $k_x \neq 0$) and the electric field along the antennas (y direction).

4.2.1 Single-antenna meta-surface

First, we outline the dipole model, commonly used to describe collective effects in plasmonic metamaterials [5–7, 11, 38, 54, 121, 122]. In its simplest version, the dipole model treats each meta-molecule with a finite size as a point electric-dipole $\mathbf{p}$ with a polarizability α relating the local electric field $\mathbf{E}_{\text{loc}}$ to the dipole moment, $\mathbf{p} = \alpha(\omega)\,\mathbf{E}_{\text{loc}}$. The local electric field polarizing the dipole at the position $\mathbf{r}$ is the superposition of the incident electric field and the electric field scattered by the other dipoles in the assembly, $\mathbf{E}_{\text{loc}}(\mathbf{r}) = \mathbf{E}_{\text{ext}}(\mathbf{r}) + \sum_{m\neq 0} \mathbf{E}_m(\mathbf{r})$, where the sum excludes the self-interaction, $\mathbf{E}_m(\mathbf{r}) = \hat{g}(\mathbf{R}_m - \mathbf{r}) \exp[-i\mathbf{k}_{\parallel} \cdot (\mathbf{R}_m - \mathbf{r})]\,\mathbf{p}$, $\hat{g}(\mathbf{r}) = (\nabla\nabla + k^2)\exp(ikr)/r$ is the dipole-

dipole interaction tensor, $k = n\omega/c$ where $n = \sqrt{\epsilon}$ stands for the refractive index, $\mathbf{k}_\parallel = (k_x, k_y)$ is the in-plane wave-vector, and $\mathbf{R}_m$ is the position of the m-th dipole in the array. By assuming that the antennas are polarizable only along the y direction, one can obtain the effective polarizability of the dipole in the array,

$$\begin{aligned}
&\alpha_{\text{eff}}(\mathbf{k}_\parallel, \omega) = \frac{1}{\alpha^{-1}(\omega) - S_0(\mathbf{k}_\parallel, \omega)}, \\
&S_0(\mathbf{k}_\parallel, \omega) = \sum_{m \neq 0} g_{yy}(\mathbf{R}_m) \exp(-i\mathbf{k}_\parallel \cdot \mathbf{R}_m), \\
&g_{yy} = \frac{e^{ikr}}{r} \{k^2 (1 - \frac{y^2}{r^2}) + \frac{ik}{r} (1 - 3\frac{y^2}{r^2}) - \frac{1}{r^2} (1 - 3\frac{y^2}{r^2})\},
\end{aligned} \tag{4.1}$$

where $S_0(\mathbf{k}_\parallel, \omega)$ is the interaction lattice sum. The 0-th order reflection and transmission coefficients of the dipole array are found to be

$$r = \frac{2\pi i k}{P_x P_y} \alpha_{\text{eff}}, \qquad t = 1 + r.$$

The collective eigenmodes of the dipole array, corresponding to the supported surface modes, are defined by the singularities of the reflection and transmission coefficients or by zeros of the denominator $\alpha^{-1}(\omega) - S_0(\mathbf{k}_\parallel, \omega)$. In general, this condition can be satisfied only at complex frequencies $\omega = \omega_r + i\omega_i$, showing that the eigenmodes have a finite lifetime due to Ohmic losses or radiative decay [55, 77]. A real eigenvalue ω may be ideally achieved only in the limit of lossless meta-surfaces and for $k_\parallel > k$, which ensures absence of absorption and radiation.

The Wood's anomalies correspond to the frequencies at which the dipoles in the array are suppressed ($\alpha_{\text{eff}} = 0$) and the array is effectively invisible and transparent to the incident radiation (r=0, t=1). This happens at the onset of the diffraction orders, for which the lattice sum diverges $S_0(\mathbf{k}_\parallel, \omega) \rightarrow \infty$. The origin of this divergence can be understood by considering a simpler model of a linear chain [5, 8, 110] of dipoles arranged along the x direction. A divergent term in this sum originates in the long-range interactions ($g_{yy}(x \rightarrow \infty, y = 0) \approx k^2 \exp(ikx)/x$) between dipoles.

$$S_0(k_x, \omega) \approx k^2 \sum_{m \neq 0} \frac{e^{ik|x_m|}}{|x_m|} e^{-ik_x x_m} = k^2 \sum_{m>0} \frac{e^{ikmP_x}}{mP_x} \{e^{-ik_x mP_x} + e^{ik_x mP_x}\}.$$

At the onset of l-th diffraction order, where $k = \pm(2\pi l/P_x + k_x)$, the lattice sum $S_0(k_x, \omega)$ grows as $\frac{k^2}{P_x} \sum_{m \neq 0} \frac{1}{m} \rightarrow \infty$.

To make the connection of Wood's anomalies with diffraction more clear, it is instructive to consider the lattice sum $S_0(\mathbf{k}_\parallel, \omega)$ in the reciprocal space [38], where it assumes the form $S_0(\mathbf{k}_\parallel, \omega) = \sum_{(l,q)} \frac{A_{(l,q)}}{k_z^{(l,q)}} + S_{0_{\text{non-singular}}}$, and diverges at the onset of (l, q) diffraction order when $k_z^{(l,q)} = \sqrt{\epsilon(\omega/c)^2 - (k_x + l\,2\pi/P_x)^2 - (k_y + q\,2\pi/P_y)^2} \rightarrow 0$. Note, however, that for some diffraction orders there are no Wood's anomalies, since $A_{(l,q)} = \frac{2\pi i}{P_x P_y}[k^2 - (k_y + 2\pi q/P_y)^2]$ tends to zero faster than $k_z^{(l,q)}$ providing no contribution to the lattice sum at the onset of diffraction order. For example, this situation appears for the p-polarized $(0, \pm 1)$ diffraction order, which, from the physical point of view, can be explained as a result of transverse character of the long-range interaction among dipoles, which do not radiate in the far-field along the direction of their moments ($g_{yy}(x = 0, y \rightarrow \infty) \sim 1/y^2$ while $g_{yy}(x \rightarrow \infty, y = 0) \sim 1/x$).

4.2.2 Double-antenna meta-surface

The dipole model can be generalized to the case of two parallel dipoles per unit cell, corresponding to a pair of plasmonic antennas in DAM. Let us consider two point-dipoles with electric dipole moments p_1 and p_2 aligned along the y-direction and separated by a distance d along the x-direction under an s-polarized illumination with k_y=0. Assuming the same polarizability α for both dipoles, we obtain a relation for the dipole moments in the array:

$$\begin{bmatrix} \alpha^{-1} - S_0 & -S_+ \\ -S_- & \alpha^{-1} - S_0 \end{bmatrix} \begin{bmatrix} p_1 \\ p_2 \end{bmatrix} = E_{\text{ext}} \begin{bmatrix} e^{-ik_x d/2} \\ e^{+ik_x d/2} \end{bmatrix}, \tag{4.2}$$

where E_{ext} is the external electric field at the center of the 0th unit cell, $S_0 = \sum_{m\neq 0} g_{yy}(\mathbf{R}_m)\exp(-i\mathbf{k}_\parallel \cdot \mathbf{R}_m)$ and $S_\pm = \sum_m g_{yy}(\mathbf{R}_m \pm \hat{x}d)\exp(-i\mathbf{k}_\parallel \cdot \mathbf{R}_m)$. The lattice sums S_0 and S_+/S_- characterize the interaction strength within and between two sub-lattices formed by p_1's and p_2's, respectively. The basis of the two electric dipoles can be changed to the more instructive basis of sub-radiant (quadrupolar) and super-radiant (dipolar) modes by the unitary transformation $p_{\text{sub}} = p_1 \exp(ik_x d/2) - p_2 \exp(-ik_x d/2)$ and $p_{\text{sup}} = p_1 \exp(ik_x d/2) + p_2 \exp(-ik_x d/2)$:

$$\begin{bmatrix} \alpha^{-1} - S_0 + \Delta & i\kappa \\ -i\kappa & \alpha^{-1} - S_0 - \Delta \end{bmatrix} \begin{bmatrix} p_{\text{sup}} \\ p_{\text{sub}} \end{bmatrix} = E_{\text{ext}} \begin{bmatrix} 2 \\ 0 \end{bmatrix}, \tag{4.3}$$

where $\Delta = -1/2[S_+ \exp(ik_x d) + S_- \exp(-ik_x d)]$ accounts for the splitting caused by the interaction between the two sub-lattices. This splitting makes the sub- and super-radiant modes red-shifted and blue-shifted, respectively, with respect to the SAM's electric-dipolar resonance. The disparity in the radiative coupling of the modes, which is reflected in their names, can be seen from the rhs of Eq. (3) which shows that only the super-radiant mode can be excited by the incident field. By reciprocity, the subradiant mode is dark and cannot radiate. Note that at normal incidence the coupling between the modes $\kappa = -i/2[S_+ \exp(ik_x d) - S_- \exp(-ik_x d)]$ vanishes, implying that in this particular case the sub-radiant component p_{sub} cannot be excited, either by the external field or through the coupling with the super-radiant mode p_{sup}. For oblique incidence, however, the sub-radiant mode couples with the super-radiant mode and therefore it is indirectly coupled to the external radiation.

While Eq. (3) is diagonal for normal incidence ($\mathbf{k}_{\parallel}$=0), this is not the case for oblique incidence. In this case there is a coupling between the super- and sub-radiant modes p_{sup} and p_{sub} which no longer represent the eigenmodes of the system. Eq. (3) can be diagonalized through an eigen-decomposition procedure using the transformation $D = 1/(1+\delta^2)[p_{\text{sup}} + i\delta p_{\text{sub}}]$ and $Q = 1/(1+\delta^2)[i\delta p_{\text{sup}} + p_{\text{sub}}]$:

$$D = \frac{1 + \Delta/X}{\alpha^{-1} - (S_0 - X)} E_{\text{ext}}, \tag{4.4a}$$

$$Q = \frac{i\kappa/X}{\alpha^{-1} - (S_0 + X)} E_{\text{ext}}, \tag{4.4b}$$

where $\delta = (X - \Delta)/\kappa$ and $X = (\Delta^2 + \kappa^2)^{1/2}$.

The physical meaning of the last transformation is to account for the hybridization of sub-radiant and super-radiant modes which takes place at oblique incidence. Since the hybridization is weak ($|\delta| \ll 1$), the modes D and Q are still dominated by super-radiant and sub-radiant components, respectively, and also have very disparate radiative coupling. It would be reasonable for these modes to be referred to as quasi super- and sub-radiant modes, however, for the sake of convenience we refer them to as dipolar and quadrupolar modes. In the special case of normal incidence, the quadrupolar mode Q coincides with the sub-radiant mode p_{sub} ($\delta = 0$) and is completely decoupled from the incident light having its lifetime limited only by the Ohmic losses. However, at finite angles, as a result of hybridization with the super-radiant component p_{sup}, it acquires a finite electric-dipolar moment and its radiative coupling and bandwidth gradually increase. The dipolar mode D, in contrast, is always strongly radiatively coupled and hence it is spectrally broad at any incidence angle.

Comparing Eqs. (4) with their single-antenna counterpart Eq. (1), we can identify $S_D = S_0 - X$ and $S_Q = S_0 + X$ as effective lattice sums for the modified modal coefficients D and Q of the double dipole meta-molecules. Just as in the case of SAM, for DAM the modal dispersion can be obtained by tracing the poles of the denominators in Eqs. (4).

The 0-th order reflection and transmission from the array can be expressed in terms of modal amplitudes in the form

$$r = \frac{2\pi i k}{P_x P_y}\, p_{\mathrm{sup}} = \frac{2\pi i k}{P_x P_y}\,(D - i\delta Q), \qquad t = 1 + r. \tag{4.5}$$

The dipole moments of the antennas in the two sub-lattices can also be written in terms of the D and Q modes as

$$p_1 = e^{-\frac{ik_x d}{2}}\{\frac{1-i\delta}{2}(D+Q)\}, \tag{4.6a}$$

$$p_2 = e^{\frac{ik_x d}{2}}\{\frac{1+i\delta}{2}(D-Q)\}. \tag{4.6b}$$

In order to study the optical response of the array close to the onset of a diffraction order, we consider the lattice sums in the reciprocal space which assume the form:

$$\begin{aligned} S_0 &= \sum_{(l,q)} \frac{A_{(l,q)}}{k_z^{(l,q)}} + S_{0_{\text{non-singular}}}, \\ S_\pm &= \sum_{(l,q)} \frac{A_{(l,q)}}{k_z^{(l,q)}} \exp[\mp i(k_x + \frac{2\pi l}{P_x})d], \\ \Delta &= -\sum_{(l,q)} \frac{A_{(l,q)}}{k_z^{(l,q)}} \cos(\frac{2\pi l}{P_x} d), \\ \kappa &= -\sum_{(l,q)} \frac{A_{(l,q)}}{k_z^{(l,q)}} \sin(\frac{2\pi l}{P_x} d). \end{aligned} \tag{4.7}$$

Here we focus on the (-1,0) order since in our case it is spectrally close to the antenna resonance. As we approach the (-1,0) Wood's anomaly, the terms containing $1/k_z^{(-1,0)}$ diverge and we can approximate the sums by retaining only these terms:

$$\begin{aligned}
S_0 &\rightarrow \frac{A_{(-1,0)}}{k_z^{(-1,0)}}, \\
\Delta &\rightarrow -\frac{A_{(-1,0)}}{k_z^{(-1,0)}} \cos(\frac{2\pi}{P_x} d), \\
\kappa &\rightarrow \frac{A_{(-1,0)}}{k_z^{(-1,0)}} \sin(\frac{2\pi}{P_x} d), \\
X &\rightarrow \frac{A_{(-1,0)}}{k_z^{(-1,0)}}, \\
\delta &\rightarrow \frac{1+\cos(2\pi d/P_x)}{\sin(2\pi d/P_x)} = \tan[\pi/2 - 2\pi d/P_x].
\end{aligned} \tag{4.8}$$

Note that this approximation breaks down for normal incidence, since there are two degenerate resonant terms, corresponding to (-1,0) and (1,0) diffraction orders. Away from normal incidence, where this approximation holds, the 0-th order reflection coefficient simplifies to

$$r_{\mathrm{WA}} = \frac{2\pi i k}{P_x P_y(\alpha^{-1} - S_0 + X)}[1 - \cos(\frac{2\pi d}{P_x})]. \tag{4.9}$$

As evident from Eq. (8), the divergent terms in $S_D = S_0 - X$ cancel out, but they are still present in $S_Q = S_0 + X$, implying that at the Wood's anomaly, the quadrupolar component vanishes (Q=0) but the dipolar component (D) remains finite, hence the reflection does not vanish as in the SAM case.

Finally, it is worthwhile noting that there is a connection between the SAM and DAM topologies. For a vanishing separation between the dipole pair ($d \rightarrow 0$), DAM reduces to a periodic array of single electric dipoles with a polarizability 2α, thus confirming the self-consistency of the generalized dipole model. As $d \to 0$, the Wood's anomalies in DAM reappear and the quadrupolar resonance disappears. At the position of the Wood's anomaly, $p_2 = -p_1$ and p_{sup}=$p_1 + p_2$=0, implying that we restore the well-know result r=0 and t=1, which also follows from Eq. (9).

4.2.3 Comparison between SAM and DAM

In general, one may expect a similar behavior for dipolar modes in SAM and more complex meta-molecules, such as in DAM. However, the numerical results show that in DAMs the character of interaction between antennas is substantially changed. To illustrate this, we plot side by side the transmission spectra of both SAM and DAM in Fig. 2. The SAM spectra (Fig. 2a) exhibit spectral features of two kinds. One appears as a minimum of transmission and corresponds to the coupling of the incident light to the collective dipolar mode with a dispersion $\omega_c(\mathbf{k}_\parallel)$ defined by the equation:

$$\mathrm{Re}\,\{\alpha^{-1}(\omega_c) - S_0(\mathbf{k}_\parallel, \omega_c)\} = 0. \tag{4.10}$$

Another one appears as a maximum of transmission, corresponding to the Wood's anomalies (shown by the color arrows in Fig. 2a and the dashed lines in Fig. 2c) of the array at the onset of the diffraction orders ($k_z^{(l,q)} = 0$). Note that this maximum never reaches unity due to the presence of the substrate. While the dipole model considered above does not capture the substrate effects, this can be accomplished by combining the model with the S-matrix formalism [12, 17]. However, the modal matching technique used here to calculate the optical response of SAM and DAM [26] rigorously considers the presence of the substrate.

For normal incidence the collective dipolar mode appears in close proximity to the electric-dipolar mode of an isolated antenna. As can be seen from Fig. 2(a,c), at larger angles it starts shifting due to "dragging" by the substrate-side (-1,0) Wood's anomaly and these two features always appear in close proximity to each other for large angles. The presence of the Wood's anomaly and its effect on the dipolar resonance are clearly related to the role of long-range interactions among meta-molecules and demonstrates the collective character of the mode [38]. Indeed, for an individual antenna the dipolar resonance corresponds to the condition $\mathrm{Re}\ \{\alpha^{-1}(\omega_0)\} = 0$, and the resonant frequency ω_0 is independent of the angle of incidence. The interaction among dipoles in the array alters the resonance position and shifts it to the new frequency ω_c defined by Eq.(10). If the resonance of the single-antenna is significantly away from the arrays Wood's anomalies, $S_0(\mathbf{k}_\parallel, \omega_c)$ is small and the resonant frequency ω_c is close to the resonance of the individual antennas. In this regime, the long-range interaction among meta-molecules is negligible and the array response is dominated by individual inclusions. However, closer to the Wood's anomaly the effect of the interaction among dipoles will result in a dramatic change in the frequency of the collective resonance ω_c due to the large value of $S_0(\mathbf{k}_\parallel, \omega_c)$ [38].

Note that because the dipolar long-range interaction among antennas is effective only in the direction perpendicular to the antenna dipolar moment, the Wood's anomaly (and the "dragging" associated with it) appears only for s-polarized incidence ($k_y = 0$, $k_x \neq 0$), i.e., when the wave-vector of the incident wave lies in the xz-plane. For p-polarized incidence (k_x=0, $k_y \neq 0$), when the wave-vector lies in the yz-plane, the dragging effect does not appear within the framework of the dipole model.

Another effect of the periodical arrangement is the suppression of the radiative losses of the dipolar mode [38], which has been recently utilized for Surface Enhanced Infrared Absorption spectroscopy [2] and fluorescence enhancement [45, 106]. Below the light line ($k_{\parallel} > k$), the imaginary parts of α^{-1} and the lattice sum S_0 exactly cancel out giving rise to the formation of guided surface waves [5, 11, 38, 107, 110]. However, even above the light line, when the collective dipolar eigenmodes correspond to complex or leaky waves, the interaction results in suppression of a portion of the radiative decay of the mode and the collective dipolar resonance appears spectrally narrower as compared to the single-antenna dipolar resonance [25, 38, 61, 120–122].

Remarkably, we do not observe the expected sharp spectral features at the frequencies corresponding to the substrate-side (-1,0) Wood's anomaly in the DAM case (Fig. 2b). The expected transmission peak is absent and the spectral position of the collective dipolar mode appears to be insensitive to the angle of incidence. This is a very peculiar behavior, since one would expect that both in SAM and DAM the electric-dipolar moments of meta-molecules interact through the same dipole-dipole mechanism, and therefore should exhibit similar spectral behavior. It is also important to notice that

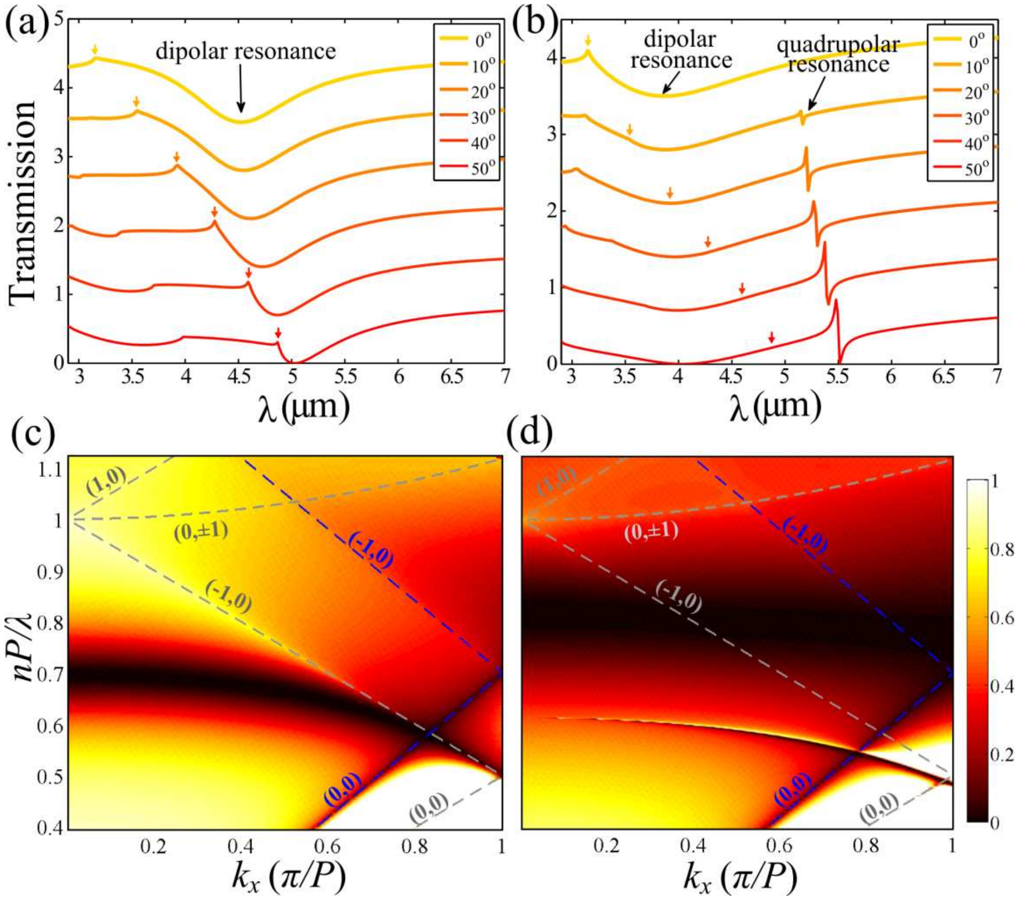

Figure 4.2: Calculated transmission spectra for s-polarized light in (a,c) SAM and (b,d) DAM perfectly conducting antennas on CaF_2 substrate. In (a,b), color arrows indicate the spectral position of the onset of the substrate-side (-1,0) diffraction order where the Wood's anomaly for SAM is observed while for DAM it is suppressed. Offset between different curves is 0.7. In (c,d) dashed lines show spectral position of substrate-side (gray) and air-side (blue) Wood's anomalies. Structure parameters are given in Fig. 1.

the bandwidth of the modes in SAM and DAM is very different indicating a different extent of the suppression of the mode's radiative decay caused by a different character of the long-range interactions among meta-molecules of different topologies.

The analytical dipole model can readily describe the observed difference between SAM and DAM structures. We have shown that for SAM the expression for $S_0(\mathbf{k}_\parallel, \omega)$ diverges at the frequency corresponding to the onset of diffraction orders. This gives rise to a Wood's anomaly which appears as a peak in the transmission spectrum. In the DAM case, one would expect Wood's anomalies due to the divergence of the effective lattice sum for the electric-dipolar moment of Eq. (4), $S_D(\mathbf{k}_\parallel, \omega) = S_0(\mathbf{k}_\parallel, \omega) - X(\mathbf{k}_\parallel, \omega)$. However in DAM the diverging terms in $S_0(\mathbf{k}_\parallel, \omega)$ and $X(\mathbf{k}_\parallel, \omega)$, as can be seen from Eq. (8), cancel out exactly, resulting in the disappearance of the Wood's anomaly and eliminating the expected spectral features.

For qualitative explanation of this effect it is instructive to look at the interactions in the dipolar array in the real space. For simplicity we consider a single chain of double-antenna meta-molecules which captures all the physics of the two-dimensional structure for the particular (-1,0) s-polarized diffraction order. We consider one row of double-antenna meta-molecules arranged along the x direction. From the first equality in Eq. (2), we obtain

$$[\alpha^{-1} - (S_0 + \frac{p_2}{p_1} S_+)]p_1 = e^{-i\frac{k_x d}{2}} E_{\text{ext}}. \tag{4.11}$$

Now we will show that at the onset of the (-1,0) diffraction order, the effective lattice sum for the p_1's dipoles, $S_1 = S_0 + \frac{p_2}{p_1} S_+$, does not have a divergent term

$$S_1 = \sum_{m \neq 0} g_{yy}(x_m) e^{-ik_x x_m} + \frac{p_2}{p_1} \sum_m g_{yy}(x_m + d) e^{-ik_x x_m}.$$

A divergent term in this sum would have come from the long-range interactions (decaying as r^{-1}) among meta-molecules. Let us consider a DAM meta-molecule (labeled m) located in the far-field from the origin. As can be seen from the expression for g_{yy} given in Eq. (1), in the far-field limit, the contribution to the lattice sum S_1 due to the interaction with the m-th meta-molecule becomes

$$g_{yy}(x_m) + \frac{p_2}{p_1} g_{yy}(x_m + d) \approx \frac{e^{ikx_m}}{x_m} + \frac{p_2}{p_1} \frac{e^{ik(x_m+d)}}{x_m + d} = \frac{e^{ikx_m}}{x_m} \{1 + \frac{p_2}{p_1} e^{ikd}\} + O(d/x_m)^2.$$

At the (-1,0) Wood's anomaly $k = \frac{2\pi}{P} - k_x$ and $\frac{p_2}{p_1} = -e^{i(k_x - 2\pi/P)d} = -e^{-ikd}$, according to Eqs. (6) and (8). Then the first term in the rhs vanishes and the contribution of the m-th unit cell to the lattice sum S_1 decays as

$$g_{yy}(x_m) + \frac{p_2}{p_1} g_{yy}(x_m + d) \approx \frac{1}{x_m^2}.$$

Thus, the interaction among the double-antenna meta-molecules decays too fast to result in a divergence in the lattice sum, which gives rise to the observed disappearance of the Wood's anomaly.

The suppression of the long-range interaction results in anomalous dispersion of the collective dipolar mode D in DAM. This can be clearly seen by comparing the spectral position of the minima corresponding to the collective dipolar modes in SAM and DAM transmission spectra in Figs. 2c and 2d. One can see that in the case of SAM, the dipolar mode is strongly dispersive because of "dragging" by the Wood's anomaly while in the DAM it is rather flat. In the case of SAM, the spectral position of the dipolar mode is strongly affected by the presence of the diverging lattice sum in the denominator of Eq. (1), $\alpha(\omega)^{-1} - S_0(\mathbf{k}_\parallel, \omega)$, and the mode acquires strong angular dependence. In contrast, in the case of DAM, the spatial dispersion of the mode is largely reduced, due to the cancellation of the diverging terms in the effective lattice sum $S_D(\mathbf{k}_\parallel, \omega)$.

Now we focus on the quadrupolar resonance in DAM. From Eq. (8) one can see that in this case the Wood's anomaly survives *because the effective "lattice sum"* $S_Q(\boldsymbol{k}_\parallel, \omega) = S_0(\boldsymbol{k}_\parallel, \omega) + X(\boldsymbol{k}_\parallel, \omega)$ *for the quadrupolar moment of the meta-molecules does diverge.* As a result we see that the spectral position of the collective quadrupolar mode is affected by the Wood's anomaly and the resonance is "dragged" to the long wavelength range at large angles (Fig. 2d). Just as in the case of the dipolar resonance in SAM, in DAM the quadrupolar resonance follows the Wood's anomaly and experiences a strong spatial dispersion.

4.3 Experimental results

4.3.1 Fabrication and optical setup

SAM and DAM arrays with the area of 400×400 μm^2 and dimensions of the unit cell given in the caption of Fig. 1 were fabricated on 0.5-mm thick CaF_2 substrates using electron beam lithography (EBL). Polymethyl methacrylate (MicroChem 950 PMMA C2) was spun at 1700 revolutions per second for 30 seconds on the substrate. A thin layer (5 nm) of chromium was deposited on the PMMA to promote conduction. This layer was etched away with chemical etchant (Transcene chromium etchant 1020AC) after exposure, before developing the sample. Desired structures were written (dosage was 300nC/cm^2 at 10pA beam current) using a Raith 50 EBL system and then developed in 1:3 MIBK:IPA developer (MicroChem) for 40s. A 3-nm thin layer of chromium was used to enhance the adhesion of the gold layer on quartz. Then an 80-nm thick layer of gold was deposited using a thermal evaporator at a base pressure of 9×10^{-7} torr. Finally, the sample was immersed in acetone for approximately one hour for liftoff. An SEM image of the fabricated DAM structure is shown in Fig. 1b. The angular-resolved transmission data were collected using a custom-made beamline based on a Fourier transform infrared (FTIR) spectrometer with the beam diameter of 300 μm. All spectra were normalized to a background of open transmission. In all cases spectra were collected at a resolution of 8 cm^{-1} and consist of 256 averaged scans.

4.3.2 Mid-IR spectroscopy of SAM and DAM

Experimental results for both SAM and DAM are shown in Fig. 3, which illustrates good agreement with the theoretical predictions in Fig. 2. Comparison of linear plots [Fig. 3 (a,b)] for the two designs clearly shows disappearance of the Wood's anomaly for the double-antenna case and a trans-

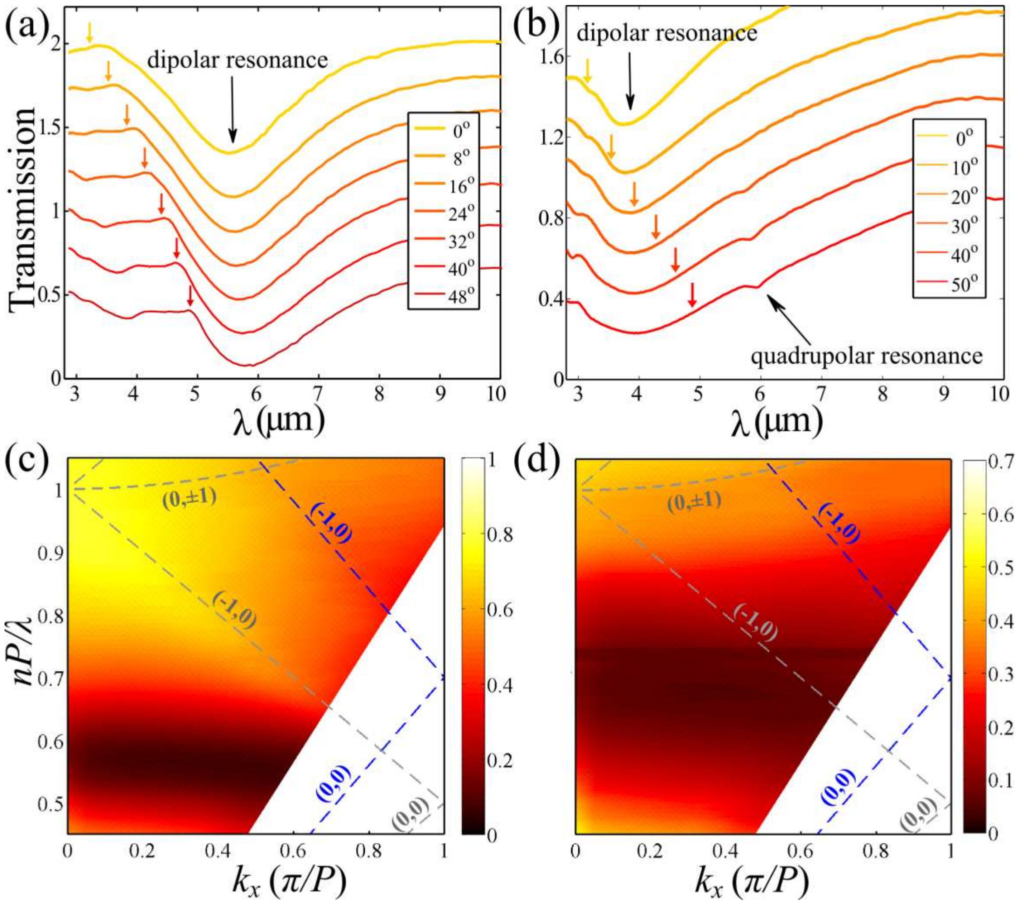

Figure 4.3: Experimental s-polarized transmission spectra for (a,c) SAM (b,d) DAM structures made of 75-nm thick gold (Au) antennas. In (a,b) color arrows indicate the expected spectral position of the onset of the substrate-side (-1,0) diffraction order where the Wood's anomaly for SAM is observed while for DAM it is suppressed. Offset between different curves is 0.2. In (c,d) dashed lines show spectral position of substrate-side (gray) and air-side (blue) Wood's anomalies. The structure parameters are given in Fig. 1. Courtesy of Dr. Burton Neuner III.

mission peak at the frequency of the onset of the s-polarized (-1,0) diffraction is observed only for the case of single-antennas. The angular-resolved transmission spectra, plotted in color in Fig. 3 (c,d), confirm the expected drastic difference in the angular dependence of the spectral position of the dipolar mode in SAM and DAM. While the range of the accessible angles of incidence is limited by the experimental setup design, the dragging is still clear in the SAM case at large angles. In contrast, for the DAM design, the suppression of the far-field interaction among meta-molecules makes the spectral position of the dipolar mode insensitive to the angle of incidence and it passes straight through the gray dashed line where the Wood's anomaly is expected. The change in the character of the long-range interaction also alters the lifetime of the dipolar mode which is broader for DAM.

The collective quadrupolar resonance in DAM can be seen around $\lambda = 6\ \mu m$, however it is not as pronounced as in the theoretical calculations, which is probably the result of the imperfections of the structure. Indeed, it is expected that the quadrupolar mode is more sensitive to metal roughness and disorder as compared to the dipolar mode due to its higher quality factor. Nevertheless, the experimental data clearly reveal theoretically predicted strong interaction among the quadrupolar moments of the meta-molecules. This is manifested in the transmission spectra as a dragging of the quadrupolar resonance by the Wood's anomaly. One can see that, as the frequency corresponding to the onset of the s-polarized substrate-side (-1,0) diffraction order approaches the quadrupolar resonance, its spectral position red-shifts due to "repulsion" from the Wood's anomaly.

4.3.3 Near-IR spectroscopy of SAM and DAM

The results presented so far have been limited to the mid-IR frequency range where metals behave as nearly perfect conductors. However, one may expect changes in the collective behavior of the periodic meta-surfaces in the near-IR frequency range where plasmonic effects start playing an important role in light-matter interaction. To reveal any changes associated with plasmonic effects, we have to refer to previous studies of light scattering by DAM structures. In Ref. [60], a silver (Ag) DAM was compared to a split-ring resonator metamaterial, and the dimensions of meta-molecules were scaled to exhibit resonances and Wood's anomalies in the near-IR spectral range.

The theoretical calculations, as shown in Fig. 4a, did not reveal any changes in collective behavior as compared to the mid-IR domain presented above. Again, the Wood's anomaly is absent in the transmission spectra and the dragging effect does not exist. Therefore, there is no evidence that plasmonic effects in near-IR may result in reappearance of the far-field interaction in DAM. The only effect of finite conductivity manifests as a modification of the antennas' polarizability and resonant frequency.

Near-IR experimental data reported in [60] for a silver DAM (fabricated by EBL on a SiO_2 substrate) confirm the theoretically predicted behavior. The experimental results are presented in Fig. 4b, and clearly show the disappearance of the Wood's anomalies and anomalously flat dispersion of the dipolar

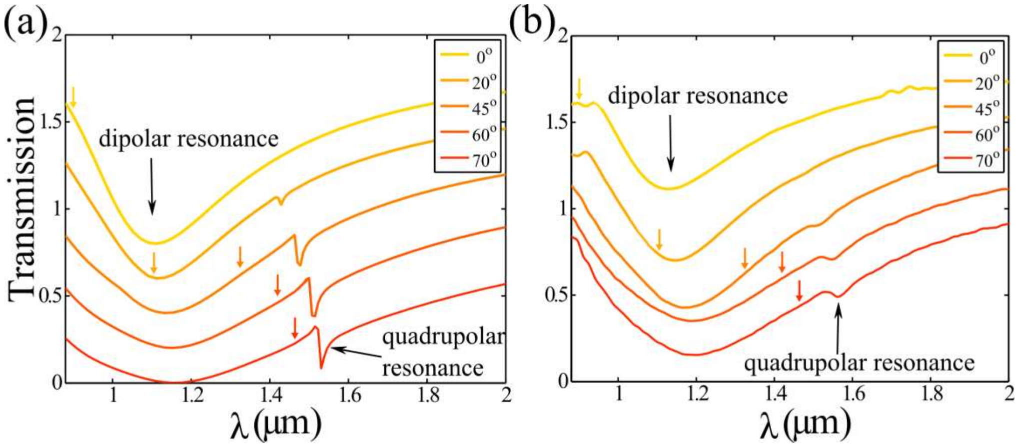

Figure 4.4: Theoretical (a) and experimental (b) near-IR *s*-polarized transmission spectra for 75-nm thick plasmonic (Ag) DAM on glass (SiO_2) substrate. Vertical color arrows indicate the expected spectral position of the onset of the substrate-side (-1,0) diffraction order. The offset between different curves is 0.2. Structure parameters are $a_y = 350$ nm, $a_x = 105$ nm, $\epsilon_{\mathrm{SiO_2}} = 2.25$, $P_x = P_y = 600$ nm, and $d = 230$ nm. Right panel is courtesy of Dr. Burton Neuner III.

mode caused by the cancellation of the long-range interaction between the double-antenna meta-molecules.

4.4 Conclusion

We have both theoretically and experimentally demonstrated the importance of the topology of meta-molecules in the collective response of frequency-selective meta-surfaces. A meta-surface comprised of a periodic array of double-antenna meta-molecules was studied as an example. We have proposed an analytical dipole model to provide a clear description of the suppression of non-local effects and long-range interactions between dipolar moments of the meta-molecules, resulting in the disappearance of the Wood's anomalies and anomalous dispersion of the collective modes of the structure. The predicted results have been experimentally confirmed in mid- and near-IR spectral domains. The discovered strong sensitivity of the spectral characteristics of collective modes envisions new approaches to design metamaterials with engineered optical properties that may avoid significant spatial dispersion effects or weaken the dependence of the response on the incidence angle.

Chapter 5

Electromagnetically Induced Polarization Conversion

5.1 Introduction

Recently there was a significant interest in plasmonic metamaterials stemming from their great promise in optical applications. The main advantages brought by the metamaterials originate in the unique optical properties of these artificial electromagnetic structures unavailable in their naturally occurring counterparts. Among these advantages are long lifetime of the modes and high density of electromagnetic energy achievable due to strong field confinement, and as a result, significant boost in light-matter interaction. In this context, asymmetric Fano resonant metasurfaces hold great promise [35, 68, 71, 76] by enabling ultrasensitive gas sensing [69], biosensing [113], broad-band slow-light [114], and other applications. On the other hand, the asymmetry of such metasurfaces endows them with unique polarization properties; it enables polarization-dependent response [114] and polarization conversion [102, 103, 119], which, to our knowledge, have not been studied in the context of Fano resonances. The possibility to convert polarization of light with ultrathin metasurfaces instead of bulky wave plates is especially attractive for practical applications. High-efficiency frequency-selective surfaces operating in terahertz has been recently introduced for polarization conversion [102]. Linear-to-circular polarization converters for visible light based on complementary (holey) metamaterials in deeply plasmonic regime have also been recently proposed [119]. Fano-resonant structures can be interesting for polarization-conversion applications because of the plasmonic analog of electromagnetically induced transparency (EIT) [68, 86, 118]. In conventional (non-EIT) metasurfaces, resonant modes' excitation results in strong reflection of light accompanied by a significant reduction in transmission. In Fano-resonant metasurfaces with EIT, one can overcome this limitation and boost the transmission. Here we apply this approach and design a plasmonic metasurface operating in mid-IR frequency range which exhibits a linear-to-circular polarization conversion with transmission reaching 40%. One of the benefits of the proposed approach to polarization conversion is the spectral selectivity stemming from the fact that, in contrast to other metasurface designs [86, 118], the EIT peak, where polarization conversion takes place, is surrounded by low transmission region. Thus, the structure naturally cuts off those spectral regions where polarization conversion does not take place or is not very efficient.

In this Chapter we introduce a new design of an asymmetric metasurface and study its optical response, including optical activity in the EIT regime. In this work, theoretical calculations and numerical modeling were performed by Dr. Alexander B. Khanikaev and the author with an equal contribution (as stated in the published work). Numerical simulations were performed using COMSOL Multiphysics. For the permittivity of the metal (silver), the Drude model was used with the parameters taken from Ref. [53]:

$$\epsilon(\omega) = \epsilon_\infty - \frac{\omega_p^2}{\omega^2 + i\gamma\omega}, \tag{5.1}$$

where $\epsilon_\infty = 3.7$, the plasma frequency $\omega_p = 13.673 \times 10^{15}$ rad/s, and the damping frequency $\gamma = 2.735 \times 10^{12}$ rad/s. The structure schematically shown in Fig. 5.1a represents a periodic array of vertical wires with attached horizontal monopole antennas of length l_M interacting with disconnected vertical dipole antennas of length l_D. The vertical wire plays the role of a "ground plate" [1, 29] for the monopole antennas connected to it (Fig. 5.1b). The resultant structure shows a resonant response for both x- and y-polarizations. In particular, the vertical dipolar antenna provides a low-quality ($Q \approx 5$) resonance for y-polarized incident light at the wavelength λ_D. For x-polarization, the structure exhibits a monopolar resonance at the wavelength given by λ_M. The latter resonance has a relatively high quality factor $Q \approx 15$ as compared to the dipolar one and its life time is mainly determined by radiative coupling to x-polarized light. Under the y-polarized illumination this mode is "dark" (subradiant).

The low-Q dipolar resonance plays the role of the "Fano background" for the high-Q monopolar resonance. By displacing the dipole antenna within the unit cell and changing its position with respect to the monopole, the degree of symmetry breaking in the structure and near-field interaction between the two modes are controlled. Changing the lengths of the antennas l_M and l_D provides an option for controlling the frequencies of the two resonances so that the monopolar resonance can be embedded into a dipolar background at a different spectral position, thus controlling interference between these modes. In the following, we focus on a specific case corresponding to spectral matching of the dipolar and monopolar resonances $\lambda_M \approx \lambda_D$. EIT-like behavior is observed in this case [68, 86, 118]. The effects related to polarization conversion enabled by the modes' coupling and circularly-polarized EIT are discussed.

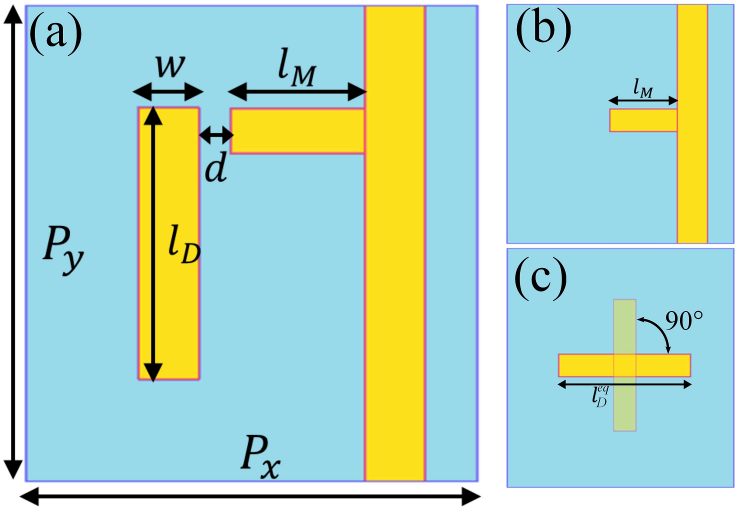

Figure 5.1: Unit cell of (a) an asymmetric Fano-resonant metasurface, (b) monopole array and (c) dipole array with unrotated and rotated dipole antennas for an equivalent dipole and Fano background cases, respectively.

5.2 Designing Polarization-Selective Fano Resonances

The design of the Fano-resonant metasurface consists of two main steps. At first we consider an array of monopole antennas attached to wires alone (without vertical dipole antennas), as shown in Fig. 5.1b. Henceforth we limit our consideration to the case of normal incidence. In this case the monopole can be excited only by x-polarized incident light but under y-polarized illumination it is “dark” (subradiant). Figure 5.2a shows x-polarized transmission spectra of the monopole metasurface where different curves correspond to different lengths of the monopole antenna l_M. We observe a behavior similar to the one known for an array of dipoles [38, 122]: as the monopole antennas’ length increases, the resonance shifts toward longer wavelengths due to their stronger polarizability and the resonance departs from the substrate-side Wood’s anomaly, which appears as a kink in the spectra at $\lambda_{WA} = \sqrt{\epsilon_{sub}} P_y = 4.725\ \mu\text{m}$. Indeed, the monopole (the horizontal antenna connected to the wire) can be roughly considered as an imaginary dipole of double length whose charge distribution is made out of the charge on the monopole antenna tip and its image of the opposite sign provided by the wire which plays the role of an effective ground plate [1, 29]. The interaction among such equivalent dipoles results in collective effects [34, 38, 78, 85] in the array: Wood’s anomalies, and collective plasmonic excitations. In fact, the observed monopolar resonance corresponds to the excitation of such a collective mode. The collective character of this mode explains not only the dependence of the resonance spectral position on the monopole length, but also the change in its quality factor. Higher quality factor for shorter monopole antennas (thus of weaker polarizability) appears due to stronger suppression of the radiative decay as the mode shifts toward the Wood’s anomaly [2, 38].

5.2.1 Monopolar mode

However, if one compares the monopole resonance with that of an "equivalent" dipole antenna of double length oriented along the x-direction (Fig. 5.1c), several discrepancies appear. First, the frequencies of the resonances do not match and the monopole appears redshifted with respect to the resonance of an equivalent dipole; this shows that *the coupling among the monopoles is stronger* due to the direct charge transfer though the wire. Second, even if the length of the equivalent dipole is adjusted (increased) to spectrally match the monopolar resonance, the quality factor of the latter appears to be several times higher, indicating *lower degree of the radiative coupling (and radiative decay) of the monopole.* This situation is illustrated by Fig. 5.2b where the transmission through an equivalent dipole structure – an array of x-oriented equivalent dipolar antennas – is plotted alongside with the transmission for the monopole array. Note that higher quality of the monopolar mode can be seen not only from the comparison of resonances' bandwidth, but is also evidenced by increased Ohmic losses for the monopole.

To explain higher quality factor of the monopole mode, we refer to Fig. 5.3(a) where the surface electric current density at the resonance frequency of monopole is shown by arrows. One can immediately see that both the x- and y-components of the currents are excited. However, at normal x-polarized excitation, the y-current cannot radiate due to the symmetry of the array, although it remains highly excited and its intensity is comparable to that of the x-current. Thus a significant part of the electromagnetic energy is confined

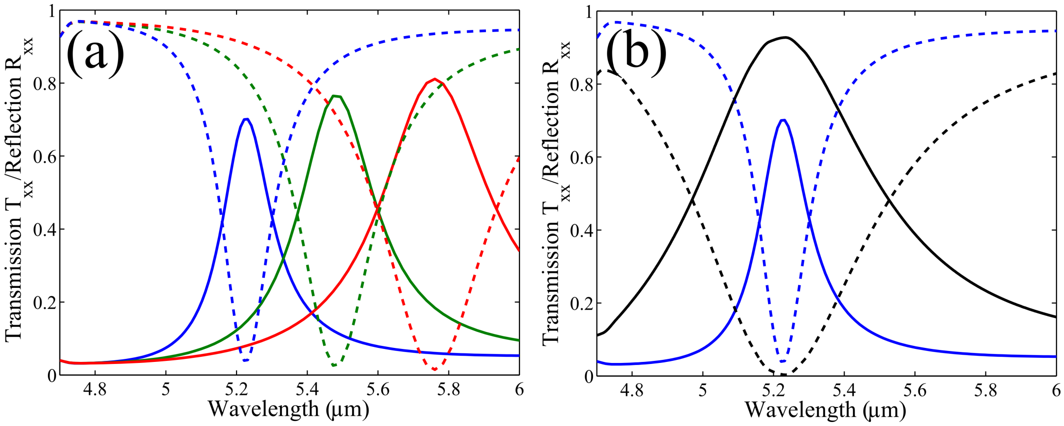

Figure 5.2: (a) x-polarized transmission (dashed lines) and reflection (solid lines) of a silver monopole antenna array shown in Fig. 5.1b under normal x-polarized illumination. Blue, green and red curves correspond to the monopole lengths l_M =0.6 μm, 0.7 μm and 0.8 μm, respectively. (b) Transmission (dashed lines) and reflection (solid lines) of a monopole antenna array shown in Fig. 5.1b (blue) and equivalent dipole array shown in Fig. 5.1c (black) under normal x-polarized illumination. The monopole antenna length is l_M=0.6 μm, and the equivalent x-dipole length is l_D=1.622 μm. In all cases w=0.35 μm, $P_x = P_y$ =3.15 μm, and the structure is assumed to rest on a CaF$_2$ substrate with ϵ_∞=2.25.

in a subradiant current component and this effectively increases the monopole's radiative lifetime as compared to its "bright" dipolar equivalent.

5.2.2 Comparison Between Monopolar And Dipolar Modes

As for the next step, we consider an array of vertical (y-oriented) dipole antennas alone shown in Fig. 5.1c (rotated semi-transparent antenna), which will provide a Fano background for the monopoles and thus enable EIT with polarization conversion. Because the array is square (P_x=P_y=P), y-polarized transmission spectrum of the array of y-oriented dipole antennas is identical to that of equivalent dipoles plotted in Fig. 5.2b for x-polarization.

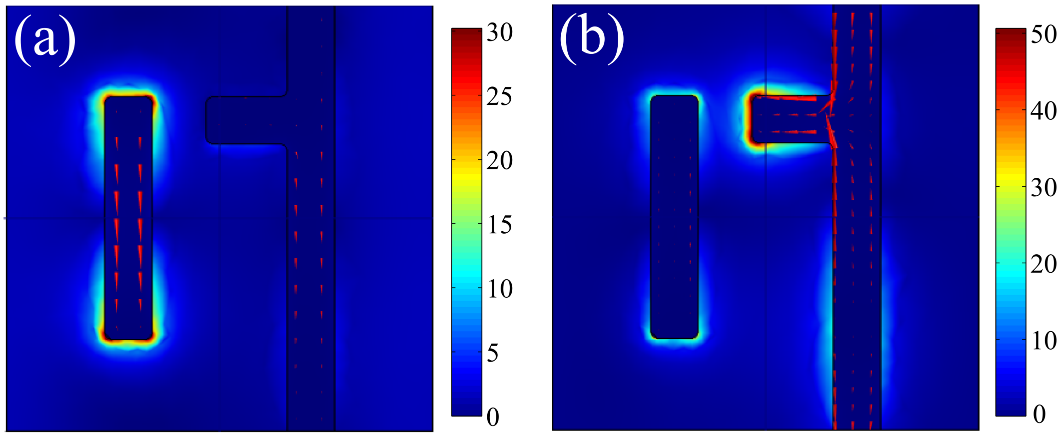

Figure 5.3: Electric field density (color) and electric current density (arrows) for the frequency (a) tuned to the EIT resonance (λ=5.71 μm) and (b) detuned from the EIT resonance (λ=6.4 μm). Structure parameters are the same as before and d=400 nm.

5.3 Interaction Between Monopolar And Dipolar Modes: Fano Resonance And Electromagnetically Induced Polarization Conversion

When both the monopole and dipole antennas are combined on the same substrate, the dipolar and monopolar modes interact in the near field, giving rise to interesting spectral features in the transmission spectra. Here we focus on the y-polarized incidence in which case the higher-Q monopole mode is "dark" and cannot be directly excited. Note that in order to induce the interaction between the modes, the mirror-reflection symmetry σ_y of the structure should be broken by displacing the vertical dipole antenna in the y-direction. From the structure's geometry follows that the σ_y symmetry is preserved and the modes do not interact when the center of the vertical antennas is placed either right on the line with the monopole antenna or exactly half way between the two nearest monopoles. This situation is analogous to previously studied dolmen EIT metasurfaces [118]. The interaction strength between the dipolar and monopolar modes depends on two factors, (i) the degree of the symmetry breaking, e.g. displacement of the vertical antenna with respect to one of the two symmetric positions and (ii) the distance between the dipole and monopole antennas. The optimal configuration corresponds to the displacement of the vertical antenna such that the antennas' tips are brought to close proximity, as shown in Fig. 5.1. In this case, the charge induced in the dipole antenna by the incident y-polarized electric field will induce the charge of an opposite sign on the monopole's tip thus resulting in the excitation of the monopolar resonance. This situation is illustrated in Fig. 5.3 where the electric field density is plotted (by color) at the frequencies of the incident light tuned (Fig. 5.3a) or detuned (Fig. 5.3b) from the frequency where the EIT takes place. For the present case of matched super-radiant (dipolar) and sub-radiant (monopolar) modes $\lambda_M \approx \lambda_D$, this frequency is approximately given by the frequency of the monopole resonance. Interaction of the modes gives rise to a notable EIT-like transmission/reflection spectrum for the y-polarized incidence. The emergence of the EIT peak is illustrated in Fig. 5.4 which shows how the total transmission $T_{tot} = T_{yy} + T_{xy}$ and the total reflection $R_{tot} = R_{yy} + R_{xy}$ change as the degree of coupling between the modes in the system changes, with the coupling controlled by the distance between the monopole and dipole antennas d. Here T_{uy} (R_{uy}) is the transmitted (reflected) light polarized along the direction u (x or y) with an incident light polarized along the y-direction. One can see that as the separation d decreases, the transmission at the EIT peak rises, reflecting an increase in the coupling strength between the modes (Fig. 5.4). The simple physical explanation of the reflectivity drop at the resonance is as follows: the monopole antenna depolarizes the dipole antenna, thereby decreasing the total dipole moment of the unit cell.

5.3.1 Polarization Conversion Using Fano Resonances

As one can expect, excitation of the monopole, which is dark in y-polarization but is radiatively coupled to x-polarization, causes the scattering of the incident radiation into the x-polarized light (T_{xy}). This scattering path-

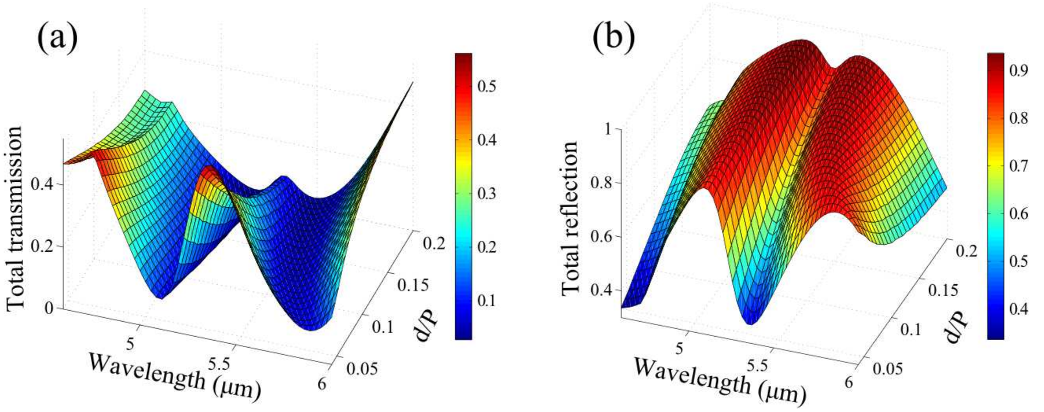

Figure 5.4: (a) EIT-like transmission and (b) reflection spectra of the asymmetric metasurface plotted as a function of the distance d between the monopole and dipole antennas. Structure parameters are the same as in Fig. 5.2.

way is an indirect coupling of the monopolar mode to the y-polarized incident light through a capacitive (near-field) interaction between the vertical dipole antenna driven by y-polarized light and the monopole antenna. However, the monopole and dipole antennas do not in general scatter in phase into the x- and y- polarizations resulting in an elliptically polarized scattered light. The phase difference between the two scattered waves depends on the degree of coupling and the light frequency. We find that in the vicinity of the EIT peak for certain degree of coupling, the monopole and dipole antennas scatter out of phase resulting in circularly-polarized transmitted light. To systematically study the polarization state of the transmitted light, we calculate the ellipticity $\eta = \tan(\frac{1}{2}\sin^{-1}(-\frac{2\mathrm{Im}(\chi)}{1+|\chi|^2}))$ of the transmitted light. Here, $\chi = t_{xy}/t_{yy}$ is the complex-valued ratio of the x-polarized and y-polarized transmission coefficients. η=0 (η=∞) corresponds to linear y (x) polarized light whereas η=1 (η=-1) corresponds to left (right) circular polarization. As can be seen from Figs. 5.5a and 5.5b, the ellipticity approaches zero away from the EIT-peak. Therefore away from the EIT peak, the transmitted light is linearly polarized along the y direction. As can be observed from the field profile given in Fig. 5.3(b), away from the EIT resonance the monopole antenna is barely excited and the dominant scattering is due to the vertical dipole.

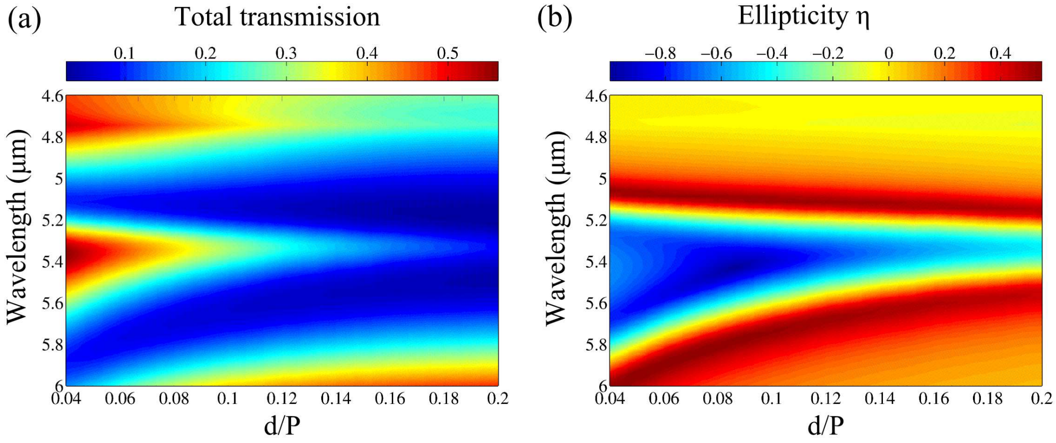

Figure 5.5: (a) Total transmission and (b) ellipticity of the transmitted light plotted as a function of the separation gap d and wavelength λ. Structure parameters are the same as in Fig. 5.2.

5.3.2 Tunability Of Polarization Conversion By Fano Coupling Strength

As the coupling strength increases with a decrease of d, the total transmission enhances while the magnitude of its ellipticity grows. The magnitude of the ellipticity increases and near the EIT peak it reaches the value η=-1 implying that the transmitted light has right circular polarization. This trend continues until the "over-coupled" regime (d/P <0.06) is entered where the ellipticity starts to drop while the total transmission continues to grow with a significant broadening of the resonance peak due to the enhanced hybridization of the monopolar mode with the strongly radiative dipolar mode. This indicates that for polarization-conversion applications, the coupling should be judiciously chosen to avoid such an over-coupled regime. Note that to produce a left circularly polarized light we need to reverse handedness of the structure. This can be achieved by moving the dipole antenna down or by considering the structure which is a mirror reflected of the original with respect to the y-z plane.

The optimal value of d can be chosen such that the total transmission is high enough while the magnitude of ellipticity exceeds 0.8. For the structure parameters we have chosen, the optimal value of d is $d = 0.073P$ for which the total transmission reaches ≈40%. The spectra of a few designs close to the optimal configuration of the metasurface are shown in Fig. 5.6, which are the cross-section of the plots in Fig. 5.4 and 5.5 for the given values of d.

5.4 Conclusion

To summarize, we have introduced a concept of polarization manipulation based on asymmetric Fano-resonant metasurfaces. We have proposed a structure which combines two distinct polarization-selective resonators (metamolecules) on the same substrate. Presence of two independent resonances makes the structure highly tunable and enables control over the spectral po-

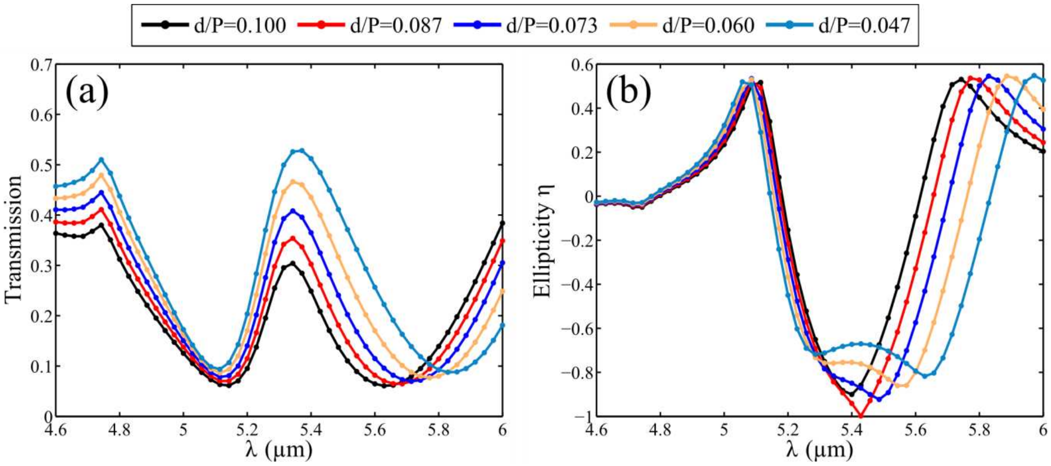

Figure 5.6: (a) Total transmission and (b) ellipticity of the light transmitted through the metasurface calculated for different values of d/P.

sitions and the quality factors of the resonances. It was demonstrated that by matching frequencies of the resonances, while endowing them with disparate lifetimes, enables an EIT-like response. The interaction between the resonances and their polarization selectivity enabled approximately circularly-polarized EIT with an ellipticity exceeding 0.80 where the total transmission was over 40%. Having a high transmission due to the nature of EIT resonance and polarization conversion at the same frequency range makes the proposed structure an excellent polarization converter of linearly polarized to circularly polarized light albeit being a subwavelength-thick structure as opposed to bulky quarter-wave plates. We believe that asymmetric metasurfaces with Fano and EIT resonances will open new avenues for numerous applications requiring polarization conversion.

Chapter 6

Summary

In this thesis, I presented my studies of the optical response of plasmonic meta-surfaces in infrared spectral range and the collective surface waves they support. These patterned surfaces, despite being extensively studied a few decades ago in the microwave spectral range, have attracted significant amount of interest in the recent years due to many promising optical applications. This thesis was an endeavor to gain a deeper understanding of the collective effects, to find the mechanisms to improve the confinement of the electromagnetic waves, and to enhance interaction of light with matter. Among important findings of my work are (i) understanding the effects of the surrounding medium on the modes and the scattering properties of metasurfaces, (ii) revealing the role of the geometry and topology of the nano patterns, and (iii) exploring the role of the symmetries of such patterns and how they can be altered to enable control over the polarization state of light. In what follows I will briefly summarize these findings.

One of the aims of my research was to improve the confinement of the surface waves to achieve many-fold enhancement of the electromagnetic fields on the surface. Two-dimensional patterns of simple shapes (such as rectangles or circles) result in surface waves with poor confinement in the infrared spectral range. More sophisticated geometries that have been shown to improve confinement in the microwave spectral range are not practical for optical applications due to fabrication challenges. In Chapter 2, I proposed an approach to improve the confinement of surface plasmons while retaining their important advantage: the ability to control the mode's index using variable size and shape of the patterns. This was achieved by combining metal structuring with the traditional method of electromagnetic field confinement, waveguiding. I theoretically predicted and my colleagues experimentally confirmed that a new class of SSPs exists in the ultrathin heterostructure comprised of a slab of high-index dielectric material and a perforated metal film.

In chapter 3, I explored an understudied but very important effect of the dielectric environment on the optical properties of the surface waves guided by metasurfaces. I found that a finite optical contrast between substrate and superstrate affects the collective effects, the main mechanism behind the supported surface waves. This happens due to modified long-range electromagnetic interactions between the unit cells of the metasurface. It was found that a large optical contrast would result in the suppression of these collective effects and in the disappearance of Wood's anomalies signifying the onset of diffraction orders.

In Chapter 4, I studied the effect of the geometry and topology of the unit cell on the collective interactions among them by considering a metasurface composed of a double-antenna unit cell. I found that in this structure the effective dipole-dipole interaction is significantly modified and the transverse long-range interaction is suppressed, which gives rise to the disappearance of Wood's anomalies, which is analogous to the effect of the finite optical contrast between the substrate and superstrate described in Chapter 3.

In Chapter 5, I explored the possibility to convert polarization of light with ultrathin metasurfaces which is attractive for practical applications because they may replace bulky wave plates used in contemporary optical systems. In order to achieve this, I developed a novel approach of multi-resonant metasurface where the coupling of the resonance elements gives rise to rescattering of the field with appropriate phases which is achieved by judicious manipulation of the symmetry of the unit cell.

To conclude, I hope my findings will be a pillar for the future work of the junior students who will pursue research on this topic in future and will further expand our understanding of light-matter interactions in nanostructures, thus enabling new revolutionary advances in technology.

Bibliography

[1] Ronen Adato, Ahmet A Yanik, and Hatice Altug. On chip plasmonic monopole nano-antennas and circuits. *Nano Letters*, 11(12):5219–5226, December 2011.

[2] Ronen Adato, Ahmet A. Yanik, Jason J. Amsden, David L. Kaplan, Fiorenzo G. Omenetto, Mi K. Hong, Shyamsunder Erramilli, and Hatice Altug. Ultra-sensitive vibrational spectroscopy of protein monolayers with plasmonic nanoantenna arrays. *Proceedings of the National Academy of Sciences*, 106(46):19227–19232, November 2009.

[3] J. Aizpurua, Garnett W. Bryant, Lee J. Richter, F. J. García de Abajo, Brian K. Kelley, and T. Mallouk. Optical properties of coupled metallic nanorods for field-enhanced spectroscopy. *Physical Review B*, 71(23):235420, June 2005.

[4] Javier Aizpurua, Thomas Taubner, F. Javier García de Abajo, Markus Brehm, and Rainer Hillenbrand. Substrate-enhanced infrared near-fieldspectroscopy. *Optics Express*, 16(3):1529–1545, feb 2008.

[5] Andrea Alù and Nader Engheta. Theory of linear chains of metamaterial/plasmonic particles as subdiffraction optical nanotransmission lines. *Physical Review B*, 74(20):205436, November 2006.

[6] Andrea Alù and Nader Engheta. Dynamical theory of artificial optical magnetism produced by rings of plasmonic nanoparticles. *Physical Review B*, 78(8):085112, August 2008.

[7] Andrea Alù and Nader Engheta. Guided propagation along quadrupolar chains of plasmonic nanoparticles. *Physical Review B*, 79(23):235412, June 2009.

[8] Andrea Alù and Nader Engheta. The quest for magnetic plasmons at optical frequencies. *Optics Express*, 17(7):5723–5730, March 2009.

[9] Pablo Alonso-Gonzalez, Martin Schnell, Paulo Sarriugarte, Heidar Sobhani, Chihhui Wu, Nihal Arju, Alexander Khanikaev, Federico Golmar, Pablo Albella, Libe Arzubiaga, Felix Casanova, Luis E. Hueso, Peter Nordlander, Gennady Shvets, and Rainer Hillenbrand. Real-Space mapping of fano interference in plasmonic metamolecules. *Nano Letters*, 11(9):3922–3926, sep 2011.

[10] Harry A. Atwater and Albert Polman. Plasmonics for improved photovoltaic devices. *Nature Materials*, 9(3):205–213, 2010.

[11] Baptiste Auguié and William L. Barnes. Collective resonances in gold nanoparticle arrays. *Physical Review Letters*, 101(14):143902, 2008.

[12] Baptiste Auguié, Xesús M. Bendaña, William L. Barnes, and F. Javier García de Abajo. Diffractive arrays of gold nanoparticles near an inter-

face: Critical role of the substrate. *Physical Review B*, 82(15):155447, oct 2010.

[13] Constantine A. Balanis. *Antenna Theory: Analysis and Design, 3rd Edition*. Wiley-Interscience, 3 edition, April 2005.

[14] W. L. Barnes, W. A. Murray, J. Dintinger, E. Devaux, and T. W. Ebbesen. Surface plasmon polaritons and their role in the enhanced transmission of light through periodic arrays of subwavelength holes in a metal film. *Physical Review Letters*, 92(10):107401, March 2004.

[15] William L. Barnes, Alain Dereux, and Thomas W. Ebbesen. Surface plasmon subwavelength optics. *Nature*, 424(6950):824–830, 2003.

[16] X. M. Bendaña and F. J. García de Abajo. Confined collective excitations of self-standing and supported planar periodic particle arrays. *Optics Express*, 17(21):18826–18835, oct 2009.

[17] X. M. Bendaña and F. J. García de Abajo. Confined collective excitations of self-standing and supported planar periodic particle arrays. *Optics Express*, 17(21):18826–18835, October 2009.

[18] H. A. Bethe. Theory of diffraction by small holes. *Physical Review*, 66(7-8):163–182, October 1944.

[19] Craig F. Bohren and Donald R. Huffman. *Absorption and Scattering of Light by Small Particles*. John Wiley & Sons, 1 edition, April 1983.

[20] Nicolas Bonod, Stefan Enoch, Lifeng Li, Popov Evgeny, and Michel Neviere. Resonant optical transmission through thin metallic films with and without holes. *Optics Express*, 11(5):482–490, March 2003.

[21] Max Born and Emil Wolf. *Principles of optics : electromagnetic theory of propagation, interference and diffraction of light*. Pergamon, Oxford [etc.], 1999.

[22] L. C. Botten, R. C. McPhedran, and J. M. Lamarre. Inductive grids in the resonant region: Theory and experiment. *International Journal of Infrared and Millimeter Waves*, 6(7):511–575, jul 1985.

[23] Sergey I. Bozhevolnyi, Valentyn S. Volkov, Eloïse Devaux, Jean-Yves Laluet, and Thomas W. Ebbesen. Channel plasmon subwavelength waveguide components including interferometers and ring resonators. *Nature*, 440(7083):508–511, March 2006.

[24] Chun-Chieh Chang, Yagya D. Sharma, Yong-Sung Kim, Jim A. Bur, Rajeev V. Shenoi, Sanjay Krishna, Danhong Huang, and Shawn-Yu Lin. A surface plasmon enhanced infrared photodetector based on InAs quantum dots. *Nano Letters*, 10(5):1704–1709, May 2010.

[25] Yizhuo Chu, Ethan Schonbrun, Tian Yang, and Kenneth B. Crozier. Experimental observation of narrow surface plasmon resonances in gold nanoparticle arrays. *Applied Physics Letters*, 93(18):181108–181108–3, November 2008.

[26] David H. Dawes, Ross C. McPhedran, and Lewis B. Whitbourn. Thin capacitive meshes on a dielectric boundary: theory and experiment. *Applied Optics*, 28(16):3498–3510, 1989.

[27] T. W. Ebbesen, H. J. Lezec, H. F. Ghaemi, T. Thio, and P. A. Wolff. Extraordinary optical transmission through sub-wavelength hole arrays. *Nature*, 391(6668):667–669, feb 1998.

[28] Hyo J. Eom. *Electromagnetic Wave Theory for Boundary-Value Problems: An Advanced Course on Analytical Methods.* Springer, May 2004.

[29] A. E. Çetin, Ahmet Ali Yanik, Cihan Yilmaz, Sivasubramanian Somu, Ahmed Busnaina, and Hatice Altug. Monopole antenna arrays for optical trapping, spectroscopy, and sensing. *Applied Physics Letters*, 98(11):111110–111110–3, March 2011.

[30] Jonathan A. Fan, Kui Bao, Chihhui Wu, Jiming Bao, Rizia Bardhan, Naomi J. Halas, Vinothan N. Manoharan, Gennady Shvets, Peter Nordlander, and Federico Capasso. Fano-like interference in Self-Assembled plasmonic quadrumer clusters. *Nano Letters*, 10(11):4680–4685, sep 2010.

[31] Jonathan A. Fan, Chihhui Wu, Kui Bao, Jiming Bao, Rizia Bardhan, Naomi J. Halas, Vinothan N. Manoharan, Peter Nordlander, Gennady Shvets, and Federico Capasso. Self-Assembled plasmonic nanoparticle clusters. *Science*, 328(5982):1135 –1138, may 2010.

[32] U. Fano. The theory of anomalous diffraction gratings and of quasi-stationary waves on metallic surfaces (sommerfeld's waves). *J. Opt. Soc. Am.*, 31:213–222, 1941.

[33] U. Fano. Effects of configuration interaction on intensities and phase shifts. *Physical Review*, 124(6):1866, dec 1961.

[34] V. A. Fedotov, N. Papasimakis, E. Plum, A. Bitzer, M. Walther, P. Kuo, D. P. Tsai, and N. I. Zheludev. Spectral collapse in ensembles of meta-molecules. *Physical Review Letters*, 104(22):223901, June 2010.

[35] V. A. Fedotov, M. Rose, S. L. Prosvirnin, N. Papasimakis, and N. I. Zheludev. Sharp trapped-mode resonances in planar metamaterials with a broken structural symmetry. *Physical Review Letters*, 99(14):147401, October 2007.

[36] G.W. Ford and W.H. Weber. Electromagnetic interactions of molecules with metal surfaces. *Physics Reports*, 113(4):195–287, nov 1984.

[37] Benjamin Gallinet and Olivier J. F. Martin. Ab initio theory of fano resonances in plasmonic nanostructures and metamaterials. *Physical Review B*, 83(23):235427, June 2011.

[38] F. J. García de Abajo. Colloquium: Light scattering by particle and hole arrays. *Reviews of Modern Physics*, 79(4):1267–1290, October 2007.

[39] F. J. García de Abajo and J. J. Sáenz. Electromagnetic surface modes in structured Perfect-Conductor surfaces. *Physical Review Letters*, 95(23):233901, nov 2005.

[40] F. J. García-Vidal, L. Martín-Moreno, Esteban Moreno, L. K. S. Kumar, and R. Gordon. Transmission of light through a single rectangular hole in a real metal. *Physical Review B*, 74(15):153411, oct 2006.

[41] F. J. García-Vidal, L. Martín-Moreno, and J. B. Pendry. Surfaces with holes in them: new plasmonic metamaterials. *Journal of Optics A: Pure and Applied Optics*, 7:S97–S101, feb 2005.

[42] C. Genet and T. W. Ebbesen. Light in tiny holes. *Nature*, 445(7123):39–46, January 2007.

[43] C. Genet, M.P van Exter, and J.P Woerdman. Fano-type interpretation of red shifts and red tails in hole array transmission spectra. *Optics Communications*, 225(4-6):331–336, oct 2003.

[44] M. Ghebrebrhan, P. Bermel, Y. X. Yeng, I. Celanovic, M. Soljačić, and J. D. Joannopoulos. Tailoring thermal emission via q matching of photonic crystal resonances. *Physical Review A*, 83(3):033810, mar 2011.

[45] V. Giannini, G. Vecchi, and J. Gómez Rivas. Lighting up multipolar surface plasmon polaritons by collective resonances in arrays of nanoantennas. *Physical Review Letters*, 105(26):266801, dec 2010.

[46] Reuven Gordon and Alexandre Brolo. Increased cut-off wavelength for a subwavelength hole in a real metal. *Optics Express*, 13(6):1933–1938, March 2005.

[47] Feng Hao, Peter Nordlander, Yannick Sonnefraud, Pol Van Dorpe, and Stefan A. Maier. Tunability of subradiant dipolar and Fano-Type plasmon resonances in metallic Ring/Disk cavities: Implications for nanoscale optical sensing. *ACS Nano*, 3(3):643–652, sep 2009.

[48] S. G. Haslinger, N. V. Movchan, A. B. Movchan, and R. C. McPhedran. Transmission, trapping and filtering of waves in periodically constrained elastic plates. *Proceedings of the Royal Society A: Mathematical, Physical and Engineering Science*, 468(2137):76–93, jan 2012.

[49] E. Hendry, A. P. Hibbins, and J. R. Sambles. Importance of diffraction in determining the dispersion of designer surface plasmons. *Physical Review B*, 78(23):235426, dec 2008.

[50] Aaron Hryciw, Young Chul Jun, and Mark L. Brongersma. Plasmon-enhanced emission from optically-doped MOS light sources. *Optics Express*, 17(1):185–192, January 2009.

[51] T. Itoh and R. Mittra. Relative convergence phenomenon arising in the solution of diffraction from strip grating on a dielectric slab. *Proceedings of the IEEE*, 59(9):1363 – 1365, September 1971.

[52] Traci R. Jensen, Michelle Duval Malinsky, Christy L. Haynes, and Richard P. Van Duyne. Nanosphere lithography: Tunable localized surface plasmon resonance spectra of silver nanoparticles. *The Journal of Physical Chemistry B*, 104(45):10549–10556, November 2000.

[53] P. B. Johnson and R. W. Christy. Optical constants of the noble metals. *Physical Review B*, 6(12):4370–4379, December 1972.

[54] K. Kempa, R. Ruppin, and J. B. Pendry. Electromagnetic response of a point-dipole crystal. *Physical Review B*, 72(20):205103, November 2005.

[55] Alexander B. Khanikaev, S. Hossein Mousavi, Gennady Shvets, and Yuri S. Kivshar. One-Way extraordinary optical transmission and nonreciprocal spoof plasmons. *Physical Review Letters*, 105(12):126804, 2010.

[56] Alexander B. Khanikaev, S. Hossein Mousavi, Wang-Kong Tse, Mehdi Kargarian, Allan H. MacDonald, and Gennady Shvets. Photonic analogue of two-dimensional topological insulators and helical one-way edge transport in bi-anisotropic metamaterials. *Accepted to Nature Materials (Editorial code NM12082163A). Also arXiv:1204.5700*, April 2012.

[57] Alexander B. Khanikaev, S. Hossein Mousavi, Chihhui Wu, Nima Dabidian, Kamil B. Alici, and Gennady Shvets. Electromagnetically induced polarization conversion. *Optics Communications*, 285(16):3423–3427, July 2012.

[58] Iskandar N. Kholmanov, Carl W. Magnuson, Ali E. Aliev, Huifeng Li, Bin Zhang, Ji Won Suk, Li Li Zhang, Eric Peng, S. Hossein Mousavi, Alexander B. Khanikaev, Richard Piner, Gennady Shvets, and Rodney S. Ruoff. Improved electrical conductivity of graphene films integrated with metal nanowires. *Nano Letters*, 12(11):5679–5683, November 2012.

[59] Charles Kittel. *Introduction to Solid State Physics*. Wiley, 8 edition, November 2004.

[60] P. W. Kolb, T. D. Corrigan, H. D. Drew, A. B. Sushkov, R. J. Phaneuf, A. Khanikaev, S. Hossein Mousavi, and G. Shvets. Bianisotropy and spatial dispersion in highly anisotropic near-infrared resonator arrays. *Optics Express*, 18(23):24025–24036, nov 2010.

[61] V. G. Kravets, F. Schedin, and A. N. Grigorenko. Extremely narrow plasmon resonances based on diffraction coupling of localized plasmons in arrays of metallic nanoparticles. *Physical Review Letters*, 101(8):087403, August 2008.

[62] Janardan Kundu, Fei Le, Peter Nordlander, and Naomi J. Halas. Surface enhanced infrared absorption (SEIRA) spectroscopy on nanoshell aggregate substrates. *Chemical Physics Letters*, 452(1–3):115–119, February 2008.

[63] Hitoshi Kuwata, Hiroharu Tamaru, Kunio Esumi, and Kenjiro Miyano. Resonant light scattering from metal nanoparticles: Practical analysis beyond rayleigh approximation. *Applied Physics Letters*, 83:4625, 2003.

[64] Basudev Lahiri, Ali Z. Khokhar, Richard M. De La Rue, Scott G. McMeekin, and Nigel P. Johnson. Asymmetric split ring resonators for optical sensing of organic materials. *Optics Express*, 17(2):1107–1115, jan 2009.

[65] Surbhi Lal, Stephan Link, and Naomi J. Halas. Nano-optics from sensing to waveguiding. *Nature Photonics*, 1(11):641–648, 2007.

[66] Lutz Langguth and Harald Giessen. Coupling strength of complex plasmonic structures in the multiple dipole approximation. *Optics Express*, 19(22):22156–22166, oct 2011.

[67] Bo-Hong Li, Charlotte E. Sanders, James McIlhargey, Fei Cheng, Changzhi Gu, Guanhua Zhang, Kehui Wu, Jisun Kim, S. Hossein Mousavi, Alexander B. Khanikaev, Yu-Jung Lu, Shangjr Gwo, Gennady Shvets, Chih-Kang Shih, and Xianggang Qiu. Contrast between surface plasmon polariton-mediated extraordinary optical transmission behavior in epitaxial and polycrystalline ag films in the mid- and far-infrared regimes. *Nano Letters*, November 2012.

[68] Na Liu, Lutz Langguth, Thomas Weiss, Jürgen Kästel, Michael Fleischhauer, Tilman Pfau, and Harald Giessen. Plasmonic analogue of electromagnetically induced transparency at the drude damping limit. *Nature Materials*, 8(9):758–762, 2009.

[69] Na Liu, Ming L. Tang, Mario Hentschel, Harald Giessen, and A. Paul

Alivisatos. Nanoantenna-enhanced gas sensing in a single tailored nanofocus. *Nature Materials*, 10(8):631–636, 2011.

[70] Matthew J. Lockyear, Alastair P. Hibbins, and J. Roy Sambles. Microwave surface-plasmon-like modes on thin metamaterials. *Physical Review Letters*, 102(7):073901, February 2009.

[71] Boris Luk'yanchuk, Nikolay I. Zheludev, Stefan A. Maier, Naomi J. Halas, Peter Nordlander, Harald Giessen, and Chong Tow Chong. The fano resonance in plasmonic nanostructures and metamaterials. *Nature Materials*, 9(9):707–715, 2010.

[72] Stefan Alexander Maier. *Plasmonics: Fundamentals and Applications*. Springer, 1 edition, may 2007.

[73] L. Martín-Moreno and F. J. García-Vidal. Minimal model for optical transmission through holey metal films. *Journal of Physics: Condensed Matter*, 20(30):304214, July 2008.

[74] L. Martín-Moreno, F. J. García-Vidal, H. J. Lezec, K. M. Pellerin, T. Thio, J. B. Pendry, and T. W. Ebbesen. Theory of extraordinary optical transmission through subwavelength hole arrays. *Physical Review Letters*, 86(6):1114, feb 2001.

[75] Graeme Walter Milton. *The Theory of Composites*. Cambridge University Press, may 2002.

[76] Andrey E. Miroshnichenko, Sergej Flach, and Yuri S. Kivshar. Fano resonances in nanoscale structures. *Reviews of Modern Physics*, 82(3):2257–2298, August 2010.

[77] S. Hossein Mousavi, Alexander B. Khanikaev, Burton Neuner, Yoav Avitzour, Dmitriy Korobkin, Gabriel Ferro, and Gennady Shvets. Highly confined hybrid spoof surface plasmons in ultrathin Metal-Dielectric heterostructures. *Physical Review Letters*, 105(17):176803, oct 2010.

[78] S. Hossein Mousavi, Alexander B. Khanikaev, Burton Neuner, David Y. Fozdar, Timothy D. Corrigan, Paul W. Kolb, H. Dennis Drew, Raymond J. Phaneuf, Andrea Alù, and Gennady Shvets. Suppression of long-range collective effects in meta-surfaces formed by plasmonic antenna pairs. *Optics Express*, 19(22):22142–22155, October 2011.

[79] S. Hossein Mousavi, Alexander B. Khanikaev, and Gennady Shvets. Optical properties of fano-resonant metallic metasurfaces on a substrate. *Physical Review B*, 85(15):155429, April 2012.

[80] Miguel Navarro-Cía, Miguel Beruete, Spyros Agrafiotis, Francisco Falcone, Mario Sorolla, and Stefan A. Maier. Broadband spoof plasmons and subwavelength electromagnetic energy confinement on ultrathin metafilms. *Optics Express*, 17(20):18184–18195, September 2009.

[81] F. Neubrech, T. Kolb, R. Lovrincic, G. Fahsold, A. Pucci, J. Aizpurua, T. W. Cornelius, M. E. Toimil-Molares, R. Neumann, and S. Karim.

Resonances of individual metal nanowires in the infrared. *Applied Physics Letters*, 89(25):253104–253104–3, December 2006.

[82] Burton Neuner, Dmitriy Korobkin, Chris Fietz, Davy Carole, Gabriel Ferro, and Gennady Shvets. Midinfrared index sensing of pL-Scale analytes based on surface phonon polaritons in silicon carbide†. *The Journal of Physical Chemistry C*, 114(16):7489–7491, April 2010.

[83] Lukas Novotny. Effective wavelength scaling for optical antennas. *Physical Review Letters*, 98(26):266802, June 2007.

[84] Masatoshi Osawa and Masahiko Ikeda. Surface-enhanced infrared absorption of p-nitrobenzoic acid deposited on silver island films: contributions of electromagnetic and chemical mechanisms. *The Journal of Physical Chemistry*, 95(24):9914–9919, November 1991.

[85] N. Papasimakis, V. A. Fedotov, Y. H. Fu, D. P. Tsai, and N. I. Zheludev. Coherent and incoherent metamaterials and order-disorder transitions. *Physical Review B*, 80(4):041102, July 2009.

[86] N. Papasimakis, V. A. Fedotov, N. I. Zheludev, and S. L. Prosvirnin. Metamaterial analog of electromagnetically induced transparency. *Physical Review Letters*, 101(25):253903, December 2008.

[87] J. B. Pendry, L. Martín-Moreno, and F. J. García-Vidal. Mimicking surface plasmons with structured surfaces. *Science*, 305(5685):847–848, August 2004.

[88] Jörg Petschulat, Arkadi Chipouline, Andreas Tünnermann, Thomas Pertsch, Christoph Menzel, Carsten Rockstuhl, Thomas Paul, and Falk Lederer. Simple and versatile analytical approach for planar metamaterials. *Physical Review B*, 82(7):075102, 2010.

[89] C. J. Powell and J. B. Swan. Origin of the characteristic electron energy losses in aluminum. *Physical Review*, 115(4):869–875, August 1959.

[90] David A Powell and Yuri S Kivshar. Substrate-induced bianisotropy in metamaterials. *Applied Physics Letters*, 97(9):091106–091106–3, sep 2010.

[91] David A. Powell, Mikhail Lapine, Maxim V. Gorkunov, Ilya V. Shadrivov, and Yuri S. Kivshar. Metamaterial tuning by manipulation of near-field interaction. *Physical Review B*, 82(15):155128, oct 2010.

[92] H Raether. *Surface plasmons on smooth and rough surfaces and on gratings*. Springer-Verlag, Berlin; New York, 1988.

[93] Lord Rayleigh. On the dynamical theory of gratings. *Proceedings of the Royal Society of London. Series A, Containing Papers of a Mathematical and Physical Character*, 79(532):399–416, August 1907. ArticleType: research-article / Full publication date: Aug. 2, 1907 / Copyright © 1907 The Royal Society.

[94] Eden Rephaeli and Shanhui Fan. Absorber and emitter for solar thermo-photovoltaic systems to achieve efficiency exceeding the Shockley-Queisser

limit. *Optics Express*, 17(17):15145–15159, 2009.

[95] A. Roberts. Electromagnetic theory of diffraction by a circular aperture in a thick, perfectly conducting screen. *Journal of the Optical Society of America A*, 4(10):1970–1983, October 1987.

[96] Carsten Rockstuhl, Thomas Zentgraf, Todd P. Meyrath, Harald Giessen, and Falk Lederer. Resonances in complementary metamaterials and nanoapertures. *Optics Express*, 16(3):2080–2090, February 2008.

[97] Jessie Rosenberg, Rajeev V. Shenoi, Sanjay Krishna, and Oskar Painter. Design of plasmonic photonic crystal resonant cavities for polarization sensitive infrared photodetectors. *Optics Express*, 18(4):3672–3686, February 2010.

[98] M. V. Rybin, A. B. Khanikaev, M. Inoue, K. B. Samusev, M. J. Steel, G. Yushin, and M. F. Limonov. Fano resonance between mie and bragg scattering in photonic crystals. *Physical Review Letters*, 103(2):023901, jul 2009.

[99] Michaël Sarrazin, Jean-Pol Vigneron, and Jean-Marie Vigoureux. Role of wood anomalies in optical properties of thin metallic films with a bidimensional array of subwavelength holes. *Physical Review B*, 67(8):085415, feb 2003.

[100] N. Stafanou and A. Modinos. Scattering of light from a two-dimensional

array of spherical particles on a substrate. *Journal of Physics: Condensed Matter*, 3(41):8135–8148, October 1991.

[101] N. Stefanou, V. Karathanos, and A. Modinos. Scattering of electromagnetic waves by periodic structures. *Journal of Physics: Condensed Matter*, 4(36):7389–7400, September 1992.

[102] Andrew C. Strikwerda, Kebin Fan, Hu Tao, Daniel V. Pilon, Xin Zhang, and Richard D. Averitt. Comparison of birefringent electricsplit-ring resonator and meanderlinestructures as quarter-wave plates atterahertz frequencies. *Optics Express*, 17(1):136–149, January 2009.

[103] Kevin Tetz, Vitaliy Lomakin, Maziar P. Nezhad, Lin Pang, and Yeshaiahu Fainman. Polarization weighting of fano-type transmission through bi-dimensional metallic gratings. *Journal of the Optical Society of America A*, 27(4):911, March 2010.

[104] Ashkan Vakil and Nader Engheta. Transformation optics using graphene. *Science*, 332(6035):1291 –1294, June 2011.

[105] D. Van Orden, Y. Fainman, and V. Lomakin. Optical waves on nanoparticle chains coupled with surfaces. *Optics Letters*, 34(4):422–424, feb 2009.

[106] G. Vecchi, V. Giannini, and J. Gómez Rivas. Shaping the fluorescent emission by lattice resonances in plasmonic crystals of nanoantennas. *Physical Review Letters*, 102(14):146807, apr 2009.

[107] G. Vecchi, V. Giannini, and J. Gómez Rivas. Surface modes in plasmonic crystals induced by diffractive coupling of nanoantennas. *Physical Review B*, 80(20):201401, November 2009.

[108] Niels Verellen, Yannick Sonnefraud, Heidar Sobhani, Feng Hao, Victor V. Moshchalkov, Pol Van Dorpe, Peter Nordlander, and Stefan A. Maier. Fano resonances in individual coherent plasmonic nanocavities. *Nano Letters*, 9(4):1663–1667, sep 2009.

[109] Kristy C. Vernon, Alison M. Funston, Carolina Novo, Daniel E. Gómez, Paul Mulvaney, and Timothy J. Davis. Influence of Particle-Substrate interaction on localized plasmon resonances. *Nano Letters*, 10(6):2080–2086, sep 2010.

[110] W. H. Weber and G. W. Ford. Propagation of optical excitations by dipolar interactions in metal nanoparticle chains. *Physical Review B*, 70(12):125429, September 2004.

[111] C.G. Wells and J.A.R. Ball. Mode-matching analysis of a shielded rectangular dielectric-rod waveguide. *IEEE Transactions on Microwave Theory and Techniques*, 53(10):3169 – 3177, October 2005.

[112] Robert W. Wood. Films of minute metallic particles. *Philosophical Magazine*, 4:396, 1902.

[113] Chihhui Wu, Alexander B. Khanikaev, Ronen Adato, Nihal Arju, Ahmet Ali Yanik, Hatice Altug, and Gennady Shvets. Fano-resonant asym-

metric metamaterials for ultrasensitive spectroscopy and identification of molecular monolayers. *Nature Materials*, 11(1):69–75, 2012.

[114] Chihhui Wu, Alexander B. Khanikaev, and Gennady Shvets. Broadband slow light metamaterial based on a double-continuum fano resonance. *Physical Review Letters*, 106(10):107403, March 2011.

[115] N. Yamamoto, K. Araya, and F. J. García de Abajo. Photon emission from silver particles induced by a high-energy electron beam. *Physical Review B*, 64(20):205419, November 2001.

[116] Ahmet A. Yanik, Arif E. Cetin, Min Huang, Alp Artar, S. Hossein Mousavi, Alexander Khanikaev, John H. Connor, Gennady Shvets, and Hatice Altug. Seeing protein monolayers with naked eye through plasmonic fano resonances. *Proceedings of the National Academy of Sciences*, 108(29):11784 –11789, jul 2011.

[117] Pochi Yeh. *Optical waves in layered media*. Wiley, February 2005.

[118] Shuang Zhang, Dentcho A. Genov, Yuan Wang, Ming Liu, and Xiang Zhang. Plasmon-induced transparency in metamaterials. *Physical Review Letters*, 101(4):047401, July 2008.

[119] Yang Zhao and Andrea Alú. Manipulating light polarization with ultrathin plasmonic metasurfaces. *Physical Review B*, 84(20):205428, November 2011.

[120] Wei Zhou and Teri W. Odom. Tunable subradiant lattice plasmons by out-of-plane dipolar interactions. *Nature Nanotechnology*, 6(7):423–427, 2011.

[121] Shengli Zou, Nicolas Janel, and George C. Schatz. Silver nanoparticle array structures that produce remarkably narrow plasmon lineshapes. *The Journal of Chemical Physics*, 120(23):10871–10875, June 2004.

[122] Shengli Zou and George C. Schatz. Narrow plasmonic/photonic extinction and scattering line shapes for one and two dimensional silver nanoparticle arrays. *The Journal of Chemical Physics*, 121(24):12606–12612, December 2004.

Vita

The list of the papers published during my PhD years are [55–58, 60, 67, 77–79, 116].

Permanent address: 3607 Greystone Dr APT 220
Austin, Texas 78731

This dissertation was typeset with LaTeX[†] by the author.

[†] LaTeX is a document preparation system developed by Leslie Lamport as a special version of Donald Knuth's TeX Program.